UNIVERSITÀ DEGLI STUDI DI SALERNO
Dipartimento di Fisica "E.R. Caianiello"

XXXII CICLO DI DOTTORATO IN
MATEMATICA, FISICA ED APPLICAZIONI

TESI DI DOTTORATO IN:

Detailed study of the 2010-2014 Pollino (Italy) seismic sequence with absorption and scattering imaging of the surrounding area

Dottorando: Ferdinando Napolitano
Tutor: Ch. Prof. Roberto Scarpa
Coordinatore: Ch. Prof. Carmine Attanasio

ANNO ACCADEMICO 2019/2020

Abstract

A detailed study of the seismic sequence occurred in the western sector of the Pollino Range (Southern Italy) between 2010 and 2014, and an imaging of the surrounding area, have been performed in this thesis. The sequence, occurred in this area considered as a seismic gap in the transition zone between the Calabrian Arc and the Southern Apennines, developed as a seismic swarm, rather than an aftershock sequence. The large number of small-to-medium earthquakes ($m_L < 5.0$) recorded by the seismic stations operated by different institutions in the area allowed to: 1) perform high quality imaging and characterization of the seismogenic volume responsible for the Pollino swarm using relative location technique; 2) characterize the properties of the medium involved during the swarm and nearby, separating scattering and absorption contribution to the total attenuation of coda waves; 3) assess site effects for seismic risk mitigation purpose by applying *HVSR* technique and polarization analysis. The hypocenter distribution, achieved using relative locations, depicted a seismogenic volume characterized by strike 150°, dip 48° and an overall normal fault kinematics, in agreement with the focal mechanism of the mainshock of $M5.0$. This volume is estimated to be $5 \times 2 \times 2km^3$, at a depth between 4.5 and 6.5 km below the sea level. The details of the analysis allowed also to follow the swarm evolution. The rupture nucleated from the central part of the seismogenic volume, spreading around and then migrating northward. Fractures opened at the shallower and deeper tips of the seismogenic volume few months after. On 25^{th} October 2012 the $M5.0$ event occurred at the southern edge of the western seismogenic volume. Many $M > 3$ occurred close to the $M5.0$, but after one month the seismicity dropped to few events per day. Scattering and absorption analysis proved, through physical evidences, the interplay between fluid-filled connected fractures in the studied area. This results explained also the SE-NW trend of the historical seismicity of the area, before the last Pollino sequence. Furthermore, site effects have been estimated in the swarm area and nearby. Achieved amplification and peaks have been mainly associated with the shallow lithology and the complex topography of the area. This detailed and complete study, which can be further improved, may enhance the current knowledge of the 2010-2014 Pollino seismic sequence. Hopefully, similar analyses may be helpful in better understanding the physics behind the evolution of swarms and their main differences with classic aftershock sequences, both in case of natural and induced seismicity.

DEDICATION AND ACKNOWLEDGEMENTS

I would like to acknowledge my supervisor Prof. Roberto Scarpa that gave me a chance to develop this project and always supported me. I am very grateful to Prof. Mario La Rocca for his patience and motivation. He really helped me in developing my research, sharing his knowledge and helping me writing papers and this thesis. I also want to thank Prof. Luca De Siena that hosted me at the University of Aberdeen (Scotland) and at the JGU in Mainz (Germany) and gave me the chance to deepen new challenging and fascinating topics. I would like to acknowledge Dr. Janire Prudencio and Dr. Luigi Passarelli for their reviews that helped me to improve the quality of this thesis. I am grateful to Dr. Giuseppe Palladino, Prof. Robert Butler and Dr. Roberto Rizzo from the University of Aberdeen for their geological tips. I really want to thank my friends and colleagues Panayiota Sketsiou and Simona Gabrielli that made me feel home in Aberdeen and helped me in developing my research and writing papers. I want to thank my family, my mom and my sister for supporting me spiritually throughout writing this thesis and my life in general. My last and heartfelt thanks go to Rosamaria. She has been always there for me, giving me the strength and the motivation I needed. Her open mind for a different view has been fundamental to improve not only this work but my whole life.

AUTHOR'S DECLARATION

I declare that the work in this dissertation was carried out in accordance with the requirements of the University's Regulations and Code of Practice for Research Degree Programmes and that it has not been submitted for any other academic award. Except where indicated by specific reference in the text, the work is the candidate's own work. Work done in collaboration with, or with the assistance of, others, is indicated as such. Any views expressed in the dissertation are those of the author.

SIGNED: ..... DATE: .....

TABLE OF CONTENTS

List of Tables

Table **Page**

List of Figures

Figure **Page**

CHAPTER 1

INTRODUCTION

The occurrence of seismic sequences characterized by a high number of earthquakes located in a small seismogenic volume is a common feature of the tectonic seismicity. Seismic sequences can be divided into *aftershock sequences* and *seismic swarms*. The latter occur in many areas of the world, but the physical mechanisms behind their origin and development are still not fully understood [*Passarelli et al.*, 2015]. Several differences between aftershock sequences and seismic swarms have been described [*Hainzl and Fischer*, 2002; *Lohman and McGuire*, 2007; *Hainzl et al.*, 2012]. Swarms are not characterized by a strong earthquake at the beginning of the sequence, but rather the seismicity rate repeatedly changes in time. Usually they comprise many events of comparable magnitude without any events much stronger that can be defined a mainshock. Swarms usually affect a focal area that is larger than the volume associated to the magnitude of the biggest earthquake occurred. Slow earthquakes may alternate with regular earthquakes, also on the same fault patches [*Lohman and McGuire*, 2007; *Ozawa et al.*, 2007]. Rupture patches migration due to the diffusion of pore-pressure lowering the normal stress on the fault [*Hainzl and Ogata*, 2005] may control the swarm nucleation and evolution, as well as natural hydro-fracturing leaking fluids into pores [*Hainzl et al.*, 2012] and slow-slip events, or aseismic creep, redistributing elastic stress along a large fault area [*Lohman and McGuire*, 2007; *Peng and Gomberg*, 2010; *Passarelli et al.*, 2015]. A complete study of a seismic sequence should always include a detailed imaging and characterization of the seismogenic source, the investigation of the properties of the medium in which waves propagate and the assessment of local site

effects. These analyses play a crucial role in the evaluation and mitigation of the seismic risk of an area. However, the quality of the results strongly depends on the number and distribution of earthquakes and seismic stations available in the area.

The main aim of this thesis is a detailed study of the seismic sequence that affected the west side of the Pollino Range (Southern Italy) between 2010 and 2014. This area is considered as a seismic gap in the transition zone between the Calabrian Arc and the Southern Apennines, [*Margheriti et al.*, 2013; *Passarelli et al.*, 2015; *Totaro et al.*, 2013, 2015]. Seismic catalogs and few historical reports indicate maximum magnitudes in the $5.2 - 6.0$ range [e.g. 1693 and 1708 earthquakes, *Rovida et al.*, 2011; *Tertulliani and Cucci*, 2014]. The lack of information about historical seismicity is partially due to a documentary gap of the sources [*Scionti et al.*, 2006], to the low density of population, and to the scarcity of settlements in the epicentral area [*Cinti et al.*, 1997]. Sound evidence exists of sporadic near-surface micro-seismic sequences which affected in the past centuries the villages of Mormanno and Morano, near the western edge of the ridge [*Guerra et al.*, 2005]. In addition, paleo-seismological investigations of the southern slope of the Pollino massif have identified at least two surface-rupturing seismic events between the sixth and fifteenth centuries A.D. corresponding to earthquakes of magnitude $6.5 - 7$ [*Cinti et al.*, 2002]. The last Pollino sequence (2010-2014), subject of this thesis, has been the most numerous seismic sequence observed in Southern Italy in recent years. More than 10.000 earthquakes of magnitude in the range $M1.0 - M5.0$ occurred in an area approximately $20km \times 15\ km$, just 4 km eastward from the village of Mormanno, relying on catalogue locations [*ISIDe*, 2010]. The seismicity rate was quite irregular, ranging from few to hundreds of events per day [*Margheriti et al.*, 2013; *Passarelli et al.*, 2015]. Most of the events were characterized by very low signal-to-noise ratio (SNR) at the farthest stations, so that the waveform could barely be distinguished from the noise. Due to these problems, the entire sequence could not be used to perform some of the analyses proposed. The seismic sequence was attributed to at least two main sub-parallel normal faults oriented approximately NNW-SSE and dipping to W-SW [*Totaro et al.*, 2015]. This peculiarity is clear from the catalogue locations of these events. The hypocenters appear to be arranged into two large groups, the western bigger than the eastern one. These faults are consistent with the extensional tectonic regime of the area, oriented NE-SW, which characterizes the entire southern Apennines. Two main shocks of $m_L 4.3$ in the eastern group and $m_L 5.0$ in the western group occurred in 2012 on May 28 and October 25, respectively [*De Gori et al.*, 2014; *Totaro et al.*, 2013, 2015; *Passarelli et al.*, 2015; *Cheloni et al.*, 2017].

The area was well instrumented during most of the seismic crisis [*Margheriti et al.*, 2013]. Permanent and temporary seismometers were installed and operated during the sequence by *Università della Calabria* and *Istituto Nazionale di Geofisica e Vulcanologia (INGV)* [*Margheriti et al.*, 2013]. The number of seismic stations further increased for few months during the *Pollino Seismic Experiment (2012-2014)* operated by the *GFZ (Geoforschungszentrum, Potsdam, Germany)*[*Passarelli et al.*, 2012]. Unfortunately this number has not always been sufficient to apply some of the techniques proposed in this work. For instance, when the sequence started on October 2010 very few stations were installed in the area, making impossible to follow its development from the very begin. Also, between May and September 2012 several temporary stations were removed to be installed in the area of the Emilia earthquake, occurred on 20 May 2012. Then, from September 2012 the number of stations around the focal area increased again, but the network distribution slightly changed. These station issues have made this study more challenging, even if a large number of earthquakes were available.

The study proposed in this thesis aims to characterize the seismogenic volume responsible for the 2010-2014 Pollino seismic sequence and the area nearby, by applying different methodologies with peculiar purposes. The opening analysis intends to enhance the current imaging of the volume activated during the swarm by performing *relative locations* of the events occurred on this structure. Several techniques for the earthquake relative location have been developed in the past decades for the analysis of volcanic events [*Frémont and Malone*, 1987; *Got et al.*, 1994] and then applied to tectonic sequence [*Yang et al.*, 2003; *Bai et al.*, 2006; *Huang et al.*, 2006; *Waldhauser and Ellsworth*, 2000; *Waldhauser and Schaff*, 2008]. The basic assumption of these techniques is that if the distance between two hypocenters is very small compared with the source to receiver distance, the two ray paths to any seismic stations are nearly identical, crossing the same velocity heterogeneities. Furthermore, two close hypocenters, characterized by comparable magnitude, are expected to produce very similar signals. When the last hypothesis is satisfied, the travel time differences at each station pairs can be easily estimated with uncertainty smaller than the sampling rate of analyzed data. Therefore these techniques give useful results when applied to seismic swarms. The *master-slave* method [*Got et al.*, 1994] has been chosen and performed in this thesis. After the selection of a conspicuous number of waveforms recorded at a reference station in two period characterized by a sufficient number of seismic stations, the normalized cross-correlation was performed on each event pair. The result was a reasonable number of clusters of similar waveforms, likely produced by the same patch of a larger seismogenic structure.

For each cluster the *master event* was selected, and its absolute location was performed using the velocity model by *Barberi et al.* [2004] in a code named $EqLoc$. The *master-slave* method was applied locating all the events of the cluster, the *slave events*, with respect to the master. The best fit plane of the hypocenter locations was computed to find out the fault patch orientation. Focal mechanisms of the master events were calculated by applying the code FOCMEC [*Snoke*, 1984, 1989] and compared with the best fit plane. the focal mechanisms computed here have been used as first input, together with the azimuth and the epicentral distance, to compute the synthetic seismograms at different stations using *Computer programs in seismology* [*Herrmann*, 2013]. After having resolved the single cluster analysis, the master events were located among them applying the same *master-slave* method. Because of the non-similarity among events belonging to different clusters, an intermediate step was needed in order to make the waveforms as similar as possible. This step consisted in filtering them at high frequency and performing the absolute value of the waveforms. The cross-correlation of these signals gave an estimate of the time differences to be used for the relative location. The final distribution of the hypocenters depicted the seismogenic volume involved during the swarm. The structure orientation was compared with the known faults of the region [*Brozzetti et al.*, 2017] and with the focal mechanism of the m_L5.0 occurred southward and deeper than the swarm location. Moreover, the precise location of the earthquakes of the clusters allows to follow the swarm evolution in space and time. These analyses performed for the Pollino sequence may also give new insights about the physical mechanism behind the nucleation and development of the swarms in general.

Once the seismogenic volume involved into the Pollino sequence was precisely depicted, the following analysis was aimed to characterize the properties of the medium involved during the swarm and the surrounding area using the attenuation of coda waves. Specifically, the main purpose is to measure the contribution of *scattering* and *absorption* to the total attenuation of coda-waves [*Sato et al.*, 2012]. The former causes energy loss due to the presence of small-scale heterogeneities, while the latter is related to anelastic processes and internal friction, resulting in heat dissipation. The resulting envelope of coda waves in heterogeneous media is a combination of both scattering and absorption contributions [*Saito et al.*, 2005; *Calvet and Margerin*, 2013]. Processes like multiple forward scattering, due to the presence of small and medium size heterogeneities, occur when waves propagate through the Earth. This is directly expressed by the broadening of the wave-packet that expands as the epicentral distance increases [*Saito et al.*, 2002]. A direct measurement of the strength of multiple scattering is the *peak-delay time*

[*Takahashi et al.*, 2007], interpreted as the time lag between the direct wave onset and the maximum amplitude of the waveform. A peak-delay time was measured for each waveform. Then, the variations of the peak-delay were mapped at different frequency bands in the selected area, divided into blocks of a chosen size. The peak-delay values of each ray crossing the $i-th$ block were averaged (*regionalization* approach). High values of peak-delay represent highly fractured medium, that means relevant presence of heterogeneities. The *absorption* contribution to the total attenuation of coda-waves depends mainly on temperature, melt or fluid content, and chemical composition in the propagation medium [*Calvet and Margerin*, 2013]. It is estimated directly by the *inverse coda quality factor,* Q_c^{-1} that determine the coda decay [*Aki and Chouet*, 1975]. In diffusive regime and in absence of leakage from the mantle [*Hennino et al.*, 2001; *Souriau et al.*, 2011; *Margerin*, 2017], the inverse coda quality factor Q_c^{-1} roughly represents the inverse absorption quality factor Q_i^{-1}, direct estimation of the absorption in the medium. The coda window was fixed for the whole dataset at the same lapse time in diffusive regime, where equipartition between P- and S-waves is reached. Then, fitting the coda decay with the theoretical equation by *Aki and Chouet* [1975] a Q_c^{-1} value for each waveform was achieved. Inverting for the spatial distribution of Q_c^{-1}, through the sensitivity kernels by *Del Pezzo et al.* [2016], the absorption map was obtained at different frequency bands. Several checkerboard tests were performed to investigate where the results were reliable. The same dataset was used for both peak-delay and $coda-Q$ analysis. The scattering and absorption maps were divided using blocks of the same size. Furthermore, these results were linked together. For each block of the map the variation of the peak-delay time and Q_c^{-1} with respect to their average has been computed. These variations have been interpreted in terms of local geological features, heterogeneities, fault networks and fluid content. The historical seismicity was also displayed on the maps. Being highly sensitive to heterogeneities and fluid contents, this analysis may be complementary to the velocity tomography, either in tectonic and volcanic environment or in areas of exploitation of georesources.

The detailed study of the 2010-2014 Pollino sequence has been completed assessing the local site effects for seismic risk mitigation [*Pitilakis*, 2004; *Panzera et al.*, 2015]. Site effects can produce change in amplitude, frequency content and polarization of the ground motion nearby at any investigated site. Several geological and morphological features may affect the local seismic response: presence of soft layers on the underlying bedrock; topographic irregularities; presence of water; landslides and underground cavities and presence of faults. [*Pitilakis*, 2004]. In the last few years, increasing importance has

been given mainly to convex and concave topographic irregularities [*Chávez-García et al.*, 1997; *Pischiutta et al.*, 2010; *Formisano et al.*, 2012], presence of faults [*Pischiutta et al.*, 2012, 2017; *Panzera et al.*, 2015, 2017] and their relationship with site effects in terms of directional resonance [*Bonamassa and Vidale*, 1991]. The Pollino area is quite complex from the tectonic and geological point of view. The combined application of *Horizontal-to-Vertical Spectral Ratios (HVSR)*[*Nakamura*, 1989] on both noise and earthquakes, and *polarization analysis* computed using the *covariance matrix method in time domain* [*Montalbetti and Kanasewich*, 1970; *Jurkevics*, 1988] could be useful to quantify the contribution of fault systems, topographic irregularities and different geological layers to the local site effects. During the seismic sequence a high number of seismic stations were installed in the area [*Margheriti et al.*, 2013], some of which very close to each other in the village of Mormanno, highly damaged by the $M5.0$ event. A large number of noise and earthquake recordings have been collected at 15 sites and used to apply the two techniques. The comparison between noise and earthquakes HVSR revealed a good agreement both in case of flat curves and presence of peaks. Few stations showed a discrepancy between these curves interpreted in terms of topographic irregularities, through the use of *polarization analysis*. The combination of both techniques pointed out that the source of the discrepancy found in a certain frequency band for these station was orthogonal to the closest mountain range to the investigated site.

In conclusion, the analysis aims to enhance the current knowledge of the 2010-2014 Pollino seismic sequence in terms of source characterization, scattering and absorption contribution to the total attenuation of coda waves in the crust nearby the swarm, and site effect assessment for seismic risk mitigation.

CHAPTER 2

GEOGRAPHICAL, GEOLOGICAL AND GEOPHYSICAL SETTING OF THE POLLINO AREA

The Pollino area, located in Southern Italy, is one of the most complex and challenging regions from the geological and geophysical point of view. This chapter aims to introduce the main geographical, geological and geophysical features that characterize this area. An overall knowledge of these properties is crucial to better interpret the results obtained through the analyses described in the following chapters. Finally, the main aspects of the last seismic sequence occurred west of the Pollino range between 2010 and 2014, subject of this thesis, will be described.

2.1 Geography of the Pollino area

The area under investigation in the thesis is the western sector of the Pollino Range, affected by the most intense seismic sequence of the last decades in Southern Italy (cyan star in Figure 2.1, right panel). The area is mostly located inside the *Pollino National Park*, the widest protected area in Italy, covering $1,925.65\ km^2$ (dark green area in Figure 2.1), extending roughly from the Ionian to the Tyrrhenian Sea. The *Pollino National Park* was founded in 1988 and secured in 1990. The headquarter of the managing body of the Park is settled in the village of Rotonda (Potenza). The Park extends between two regions, Calabria and Basilicata. It comprises three provinces, Potenza, Matera and Cosenza, and 56 municipalities.

Figure 2.1: Map of the Italian Peninsula (on the left panel) and of the Pollino National Park (on the right panel). The cyan star on the right panel represents the location of the 2010-2014 seismic sequence.

The Pollino National Park includes some of the highest mountains of Southern Italy: the highest *Serra Dolcedorme* (2267 mt), the *Mt. Pollino* (2248 mt), *Serra del Prete* (2181 mt) and *Serra del Ciavole* (2127 mt). Many rivers can be found inside the Park: *Sinni* (97 km), *Lao* (64 km), *Coscile* (49 km) and many others. This place is suggested for long walks, trekking and hiking but, due to the variety of the countrysides, climbing rafting, mountain biking and spelunking shall be carried out (further information at the website: *http://www.parcopollino.it/*).

2.2 Geological setting

The Pollino area is a complex geological setting, due to the superposition of a Early Pleistocene low strain-rate NE-SW extensional deformation over pre-existing strike-slip Late Pliocene-Early Pleistocene structures [*Ghisetti and Vezzani*, 1983; *Schiattarella*, 1998]. This current NE-SW extensional regime of the area, driven by the simultaneous retrograde SE motion of the subduction zone and by the opening of the Tyrrhenian back-arc basin [*D'Agostino et al.*, 2011], accommodates mainly normal faults nearly parallel to the Apennines chain [*Schiattarella*, 1998; *Brozzetti et al.*, 2009, 2017].

A large number of models about the evolution of the Southern Apennines relies on an alternation of carbonates platforms and pelagic basins driven by the relative motion of the European and African plates during the Late Neogene [*Dewey et al.*, 1989]. In Figure 2.2, taken by *Noguera and Rea* [2000], is shown the starting configuration from West to

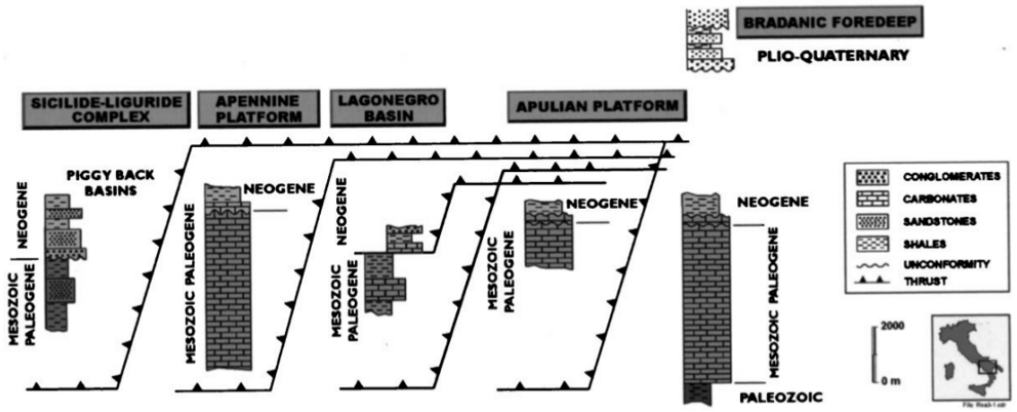

Figure 2.2: Image taken from *Noguera and Rea* [2000]. From East to West, or from the top to the bottom of the accretionary wedge: Liguride-Sicilide basinal domain, Apenninic or Lucania-Campania Platform, Lagonegro Basin and Apulian Platform. Ages and overlapping direction of the are also specified.

East and from the top to the bottom of the accretionary wedge of these units:

- Liguride-Sicilide basinal domain;
- Apenninic or Lucania-Campania Platform;
- Lagonegro Basin;
- Apulian Platform.

The shallowest *Liguride Basin* is a Jurassic-Cretaceous ophiolitic unit of oceanic origin, beneath which lays the *Campania-Lucania Platform*, dated from the late Triassic to early Miocene. Then going deeper, the *Lagonegro Basin* is found. This is a unit mainly composed of deep-sea sediments, whose age ranges from early Triassic to lower-middle Miocene. Lastly, the deepest structure found is the carbonatic *Apulian Platform* (Figure 2.3, modified after *Schiattarella* [1998]). These layers overlapped due to the opening of the Tyrrhenian sea from west, that caused the eastward migration of the subduction of the African plate under the European plate.

This thesis focuses mainly on the recent seismic activity on the western side of the *Pollino Ridge*, a N120 trending morpho-structure, formed by Meso-Cenozoic carbonate rocks, bordered by two Quaternary basins: the northern *Mercure Basin* and the southern *Castrovillari Basin* (Figure 2.3, modified after *Schiattarella* [1998]). In the study area the Liguride Unit and the Apennines Platform, a >4 km-thick carbonate shelf succession,

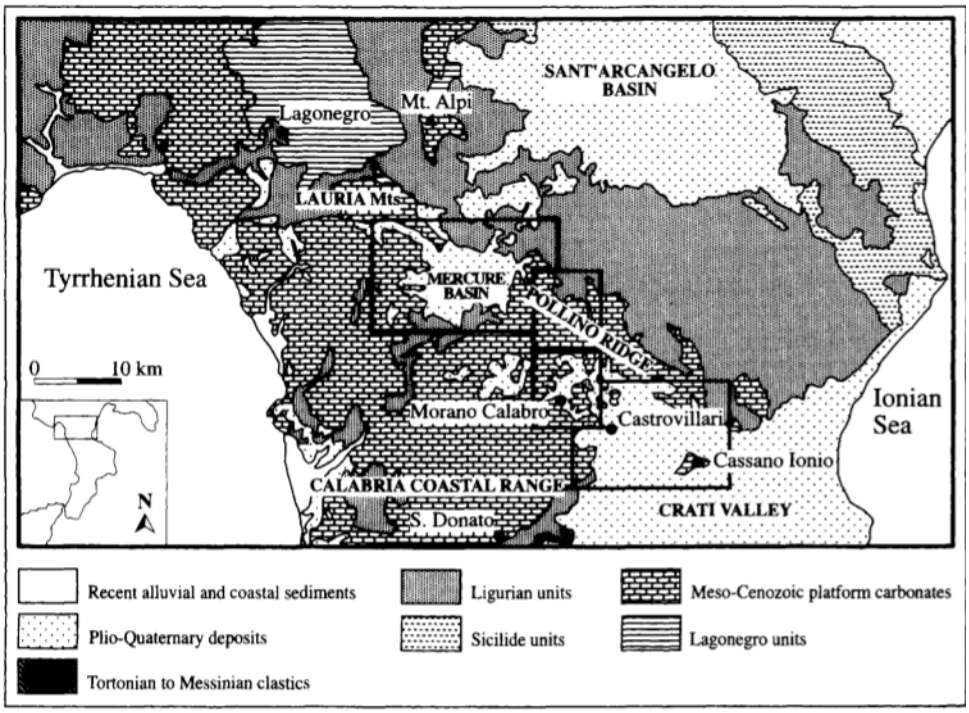

Figure 2.3: Geological map of the Pollino and surrounding area from *Schiattarella* [1998]. The map covers the area from the Lucanian Apennines-Sant'Arcangelo Basin north to the southern Crati Valley, from the Calabria Coastal Range on the Tyrrhenian Sea to the Ionian Sea.

crop out [*Brozzetti et al.*, 2017]. The Campania-Lucania Platform can be separated in the *Verbicaro Unit*, that crops out in the Calabria Coastal Range, and in the *Pollino Unit*, along the southwest margin of the Pollino Massif. This Platform is mainly composed by shallow-water dolomites and dolomitic limestones overlain by carbonate deposits [*Patacca and Scandone*, 1989]. In this area, more precisely in the Verbicaro Unit of the Apenninic Platform, is located the area affected by the 2010-2014 seismic sequence, subject of this thesis.

Some analyses performed in the thesis will require also a basic knowledge of the main characteristics of the area surrounding the 2010-2014 seismic sequence fault system from the geological point of view. A summary of the main geological features of the *Mercure* and *Castrovillari Basins*, and of the *Lauria Mountains* is explained as follows. The *Mercure Basin* is located just north of the area affected by the seismic sequence. It is a depression that extends from the Pollino Ridge on the East to the Lauria Mountains on the West, for a 15×10 km with a main WNW-ESE elongation [*Ferranti et al.*, 2017]. This basin is filled in with Pleistocene alluvial, fluvial-deltaic and lacustrine sediments

[*Schiattarella*, 1998]. The *Castrovillari Basin*, or *Castrovillari-Cassano Basin*, is the southern boundary of the Pollino Ridge, extending from the town of Castrovillari to the beginning of the southern Crati Valley. From deeper to shallower layers, the basin is filled by: lower Pliocene aged marine clay and sand, outcropping along the western side of the Crati Valley; marine fine sediments and conglomerates, dated from the upper part of late Pliocene to lower Pleistocene; by marine, transitional and continental deposits ascribed to the lower Pleistocene [*Schiattarella*, 1998]. The *Lauria Mountains*, northwest of the Mercure Basin, represent the extension of the carbonatic Pollino Ridge. They are characterized by the same geological features, until the Lucanian Apennines, a barrier that separates this area from the northern Val D'Agri, well-known due to the debated oil explorations. Geologically this barrier represented by the Lucanian Apennines is a compact carbonate stand-alone block, surrounded by faults and isolated through clay formations. Fractured volumes of minor importance are present in this block due to the high-compression regime in the region.

2.2.1 Main fault pattern in the Pollino area

The most detailed work on the Pollino range faulting system is the paper by *Brozzetti et al.* [2017], in which the authors provide precise information on the most relevant fault segments, listing their length, strike, dip and rake, slip rate and many others specific features, covering an area of $1200 km^2$. The aim of this section is to summarize the most interesting properties of the main faults of the Pollino Range using the Figure 2.4 modified after *Brozzetti et al.* [2017] as a reference. In the upper a) panel, three main sets of normal faults are shown: a set of East- to NNE-dipping faults, the *Coastal Range Fault Set (CRFS)* (red lines in Figure 2.4), mainly composed by NS strike-direction faults alternating to WNW-ESE transfer segments, and two sets of SW-dipping faults (light blue lines, in Figure 2.4). Moreover, the SW-dipping faults are divided in an *Eastern* and *Western* NW-SE-striking sets. The former, the *Seluci - Viggianello e Piano di Pollino e Castrovillari fault (SVPC)*, consists of three main en échelon[1] faults with strike from WNW-ESE to NNW-SSE (from the North to the South, the *Castello Seluci - Timpa della Manca (CPST)*, *Viggianello - Piano di Pollino (VPP)* and the *Castrovillari (CAS)* faults). The second SW-dipping group is the *Rotonda e Campotenese Set (ROCS)*, that extends across the 2010-2014 Pollino epicentral area and consists of two main right-stepping en

[1]Or "en échelon gash fractures" appear as more short and parallel mineral-filled lenses, originated as tension fractures in the direction of the major stress orientation, then filled by a mineral precipitation.

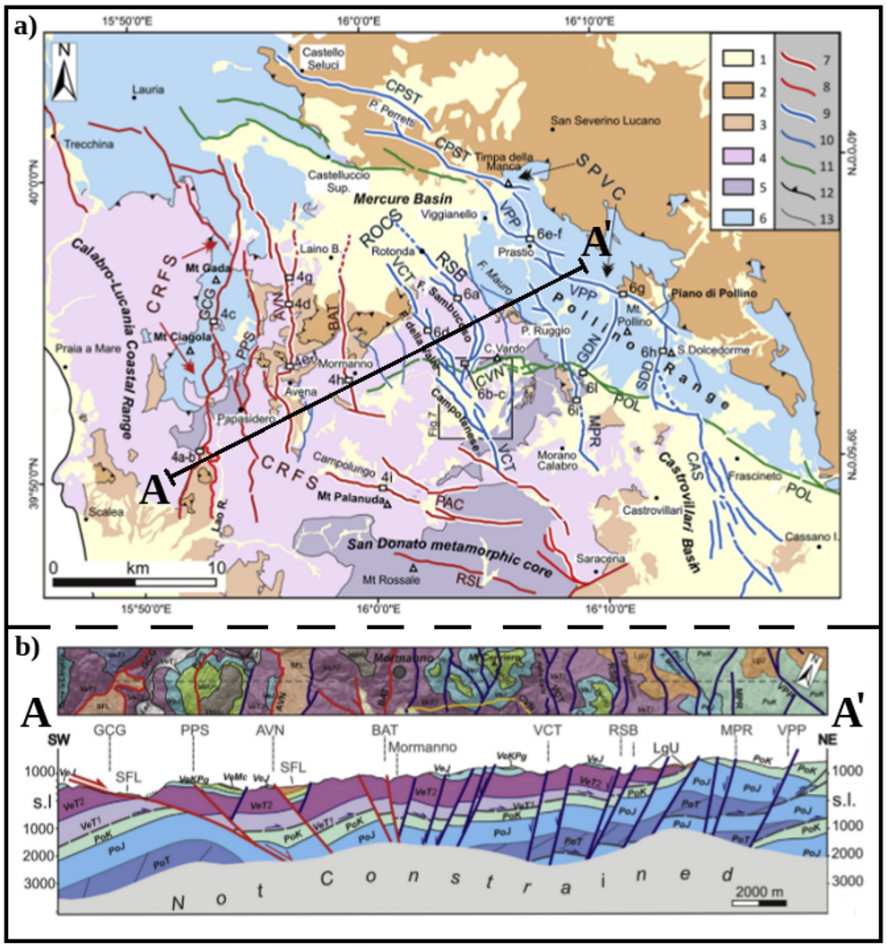

Figure 2.4: panel a) shows the structural scheme of the fault network in the Pollino area, the main tectonic units and the Quaternary basins. Key: 1) sin-extensional deposits of the continental basins (Mercure, Campotenese and Morano C. basins) and of the marine Castrovillari basin; 2) Liguride unit; 3) "Scisti del Fiume Lao"; 4) Apennine Platform western unit (*Verbicaro Unit*, Late Triassic-Early Miocene); 5) San Donato metamorphic core; 6) Apennine Platform eastern Unit (*Pollino unit*, Late Triassic-Late Cretaceous); 7) Middle Pleistocene to Holocene east-dipping normal fault; 8) Early-Middle Pleistocene east-dipping normal fault; 9) Late Pleistocene to Holocene west-dipping normal fault; 10) Early-Middle Pleistocene west-dipping normal fault; 11) Early to Middle Pleistocene south-dipping normal fault; 12) thrust fault; 13) basal contact of "Scisti del Fiume Lao" Fm. Acronyms: CRFS) Coastal Range Fault Set; ROCS) Rotonda-Campotenese Fault Set; SVPC) Castello Seluci-Viggianello-Piano di Pollino-Castrovillari Fault Set; MPR) Morano Calabro-Piano di Ruggio fault and GDN) Gaudolino fault; POL) Pollino fault; CVN) Cozzo Vardo-Cozzo Nisco fault. Panel b) cross-section AA' showing stratigraphy and thickness of the three major superimposed units (Ligurian (LGU), Verbicaro (Ve) and Pollino (Po) units. These are Figures 2. and 3. modified after *Brozzetti et al.* [2017]

échelon fault segments (the *Rotonda - Sambucoso, RSB*, and the Valle e Campotenese, VCT faults).

Drawing an E-W cross-section passing through the village of Mormanno (*AA'* thick line in Figure 2.4a, then showed in panel 2.4b in cross-section) and constrained to the first 3 km of crust, *Brozzetti et al.* [2017] highlight some interesting properties of the fault system. From West to East, from the *Gada-Ciagola (GCG)* to the *Battendiero (BAT)* fault, it is clear the increase of the dip angle of these structures. Moving Eastward we encounter the West-dipping faults of the ROCS set, from the VCT faults, a 15 km long fault system characterized by strike of average 115° and similar dip angles around 50° – 60°, to the RBS, 10 km long fault system, striking from NNW-SSE to N-S and dipping with an average 60° angle.

2.3 The 2010-2014 Pollino seismic sequence

The western sector of the Pollino Range, just few kilometers eastward from Mormanno village, was affected between 2010 and 2014 by a long-lasting seismic sequence of more than 10,000 low-to-moderate earthquakes. Approximately the 90% of these events barely reached magnitude M_L2.0. The area is a well-known seismic gap in the Italian historical earthquake catalogue [*Rovida et al.*, 2011]. The seismic sequence was characterized by a swarm behaviour, without a typical mainshock-aftershock succession. Indeed, the seismicity rate frequently changed during the sequence [*Passarelli et al.*, 2015]. After two years from the beginning of the sequence, the two mainshocks occurred: the first one on 28 May 2012 (M_L4.3), the second one on 25 October 2012 (M_L5.0).

Temporary and permanent seismic stations were installed and operated during the sequence by *Università della Calabria* and by *Istituto Nazionale di Geofisica e Vulcanologia (INGV)* [*Margheriti et al.*, 2013]. The number of seismic stations further increased during the *Pollino Seismic Experiment (2012-2014)* operated by the *GFZ (Geoforschungszentrum, Potsdam, Germany)* [*Passarelli et al.*, 2012]. Unfortunately several temporary stations were removed before the sequence end to be installed in the area of the Emilia earthquake, occurred on 20 May 2012. For this reason, during the periods of intense activity the number of seismic stations was not suitable to perform some analyses.

Pollino sequence development The seismicity of the 2010-2014 Pollino sequence was well studied in *Passarelli et al.* [2015]. The aim of this paragraph is to resume the

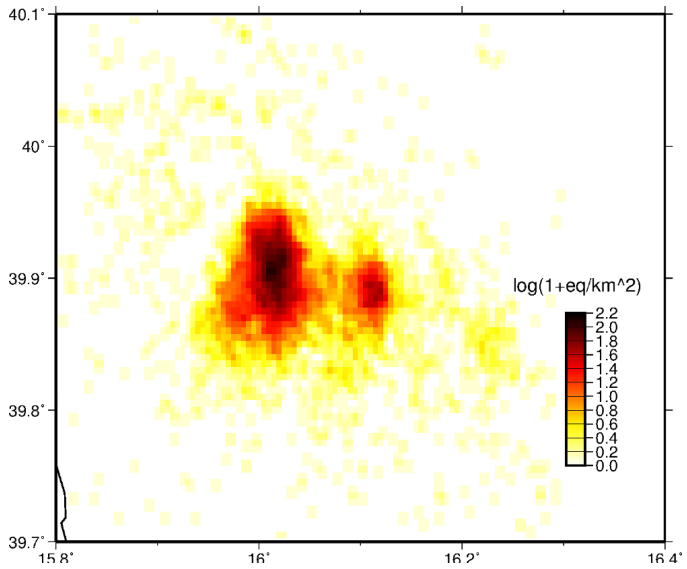

Figure 2.5: Map showing the number of event per square kilometer of the whole sequence. The scale is logarithmic, from white (0 ev/km^2) to brown (for the highest values of density).

main phases of the swarm development using this paper as reference. The seismicity of the whole sequence was grouped in two main seismogenic volumes: a larger volume comprising approximately 80% of the whole sequence, and a smaller volume located east from the first one. Taking into account the locations from the official Italian Catalogue [*Rovida et al.*, 2011], Figure 2.5 shows that the earthquake density reached 160 epicenters per square kilometer. This number may surely be higher due to the undetected small magnitude events by the automatic software used to perform the absolute locations. Missing events is a frequent issue during the most intense periods of a seismic sequence, due to the high seismicity rate and the temporal proximity of the events. The beginning of the sequence coincides with the increase of the seismicity rate on 2 October 2010. This seismicity phase lasted for about a month and was located in a NNE-SSW stretched ellipse (phase 1, blue squares in Figure 2.6, modified after *Passarelli et al.* [2015]). The seismicity was characterized by few events per day during the following year, until September 2011 (phase 2, cyan diamonds in Figure 2.6). Between November 2011 and April 2012 the seismic rate increased, reaching 85 earthquakes per day for few days (phase 3, green pentagons in Figure 2.6). During this phase the seismicity was totally confined in the bigger western volume. The seismicity then migrated on the eastern volume. A M_L4.3 event occurred on 28 May 2012 and was followed by aftershocks for one month (phase 4, orange triangles in Figure 2.6). After this phase the seismic rate

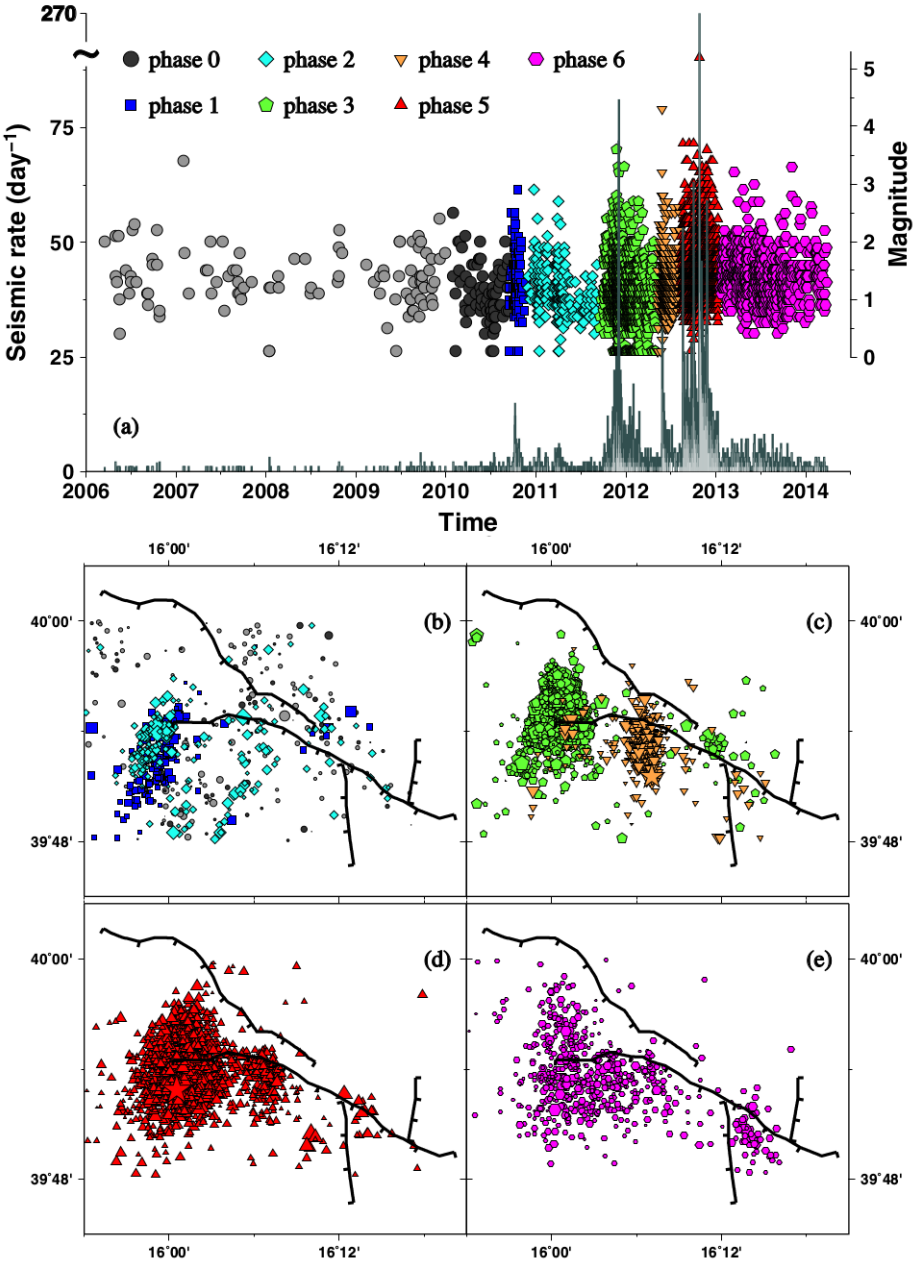

Figure 2.6: Phases (upper panel) and their spatial location (bottom panel), that characterized the 2010-2014 sequence. Seismic rate and magnitude of the events from 2006 to 2014 are also shown. Figure 3 taken from *Passarelli et al.* [2015]

decreased to few events per day until August 2012, when an increased number of events marked both the seismogenic volumes between September 2012 and February 2013 (phase 5, red triangles in Figure 2.6). During this phase, on 25 October 2012 the second mainshock of M_L5.0 occurred in the western seismogenic volume, followed by aftershocks and by more than ten $M > 3$ events. Finally, few event per day characterized the last part of the sequence until the beginning of 2014 (phase 6, magenta circles in Figure 2.6).

Even though the area is a gap of large magnitude earthquakes in the Italian Peninsula, the seismic structures are clearly very active. In addition, *Cheloni et al.* [2017] showed, through the use of Global Positioning System (GPS) and Synthetic Aperture Radar (SAR) data, that a transient slip, characterized by the same mechanism of the main shock, started some months before the M5.0 mainshock and lasted almost one year, with a released moment equivalent to a M_W5.5. This is a clear evidence that a part of the deformation was released aseismically. *Cheloni et al.* [2017] pointed out that the longer recurrence time of $M > 6.5$ events in the Pollino seismic gap is likely due to the frequent mixed seismic/aseismic strain release. The results indicate that an aseismic fault slip event may have been the most likely driving process of the last Pollino swarm.

Historical seismicity The Pollino area is considered a *seismic gap* in historical seismicity. Seismic events in the catalogue barely reached M6 [*Guerra et al.*, 2005; *Tertulliani and Cucci*, 2014]. This lack of historical seismicity was also partially due to a documentary gap of the historical sources [*Scionti et al.*, 2006] and to the low population and scarcity of settlements in the epicentral area [*Cinti et al.*, 1997]. Notably five events (1693, 1708, 1792, 1825 and 1894) characterized by magnitudes between 4.5 and 5.5 are listed in the Italian Catalogue [*Rovida et al.*, 2011]. According to *Tertulliani and Cucci* [2014], the 1693 and 1708 events had a swarm-like behaviour, similar to the 2010-2014 sequence. Paleo-seismological investigations in the southern Pollino area [*Cinti et al.*, 1997, 2002] have recognized at least two large faults in the Castrovillari area capable of earthquakes of magnitude $6.5 - 7$ and slip on this faults compatible with at least two large events (M>6) in the last 10000 years, leading to the proposal of a seismic gap for this area. Unfortunately, no trace are left related these major events in the historical records. Before the well-recorded 2010-2014 sequence, only the Mercure earthquake, occurred in the Mercure basin, located just above the Pollino area, on 9 September 1998 (M_L5.5) was instrumentally recorded.

Latest studies about the 2010-2014 sequence Several studies have been performed on the 2010-2014 Pollino sequence and its connection with geology and fault structures. Location of the events characterized by $M_L \geq 1$ and hypocentral depth lower than 30km and focal mechanisms of those of $M_L \geq 2.7$ were computed by *Totaro et al.* [2015] using SIMULPS and CAP softwares, respectively. In the same work the double difference relative locations using HYPODD were computed [*Waldhauser and Ellsworth*, 2000]. These results were used by *Brozzetti et al.* [2017] to link the seismicity of the sequence with the newly identified Quaternary and active faults of the area. They found that three are the main structures involved in this swarm. The interplay between the *Fosso della Valle-Campotenese (VCT)* and *Rotonda-Sambucoso (RBS)* faults, comprised in the *Rotonda-Campotenese Fault Set* (ROCS in Figure 2.4), was responsible for the seismicity on the western seismogenic volume of the swarm. The smaller eastern cluster that characterized the phase 4 of the sequence (Figure 2.6) was well correlated with the *Morano Calabro-Piano di Ruggio* fault (MPR in Figure 2.4).

Using different kind of data and methodology, *Passarelli et al.* [2015] highlighted the presence of **aseismic transient** driving the 2010-2014 Pollino sequence, although in that work was not possible to understand the type of aseismic transient, while *Cheloni et al.* [2017] found a long-lasting slow-slip event via deformation data. *Passarelli et al.* [2015] pointed out interesting specific features of swarm-like sequences as the lack of an early mainshock followed by aftershocks, a change of the *b-value* in the Gutenberg-Richter law and, particularly, the fact that *the sequence has affected a much larger volume of rocks than what is expected according to the largest magnitude event: a* $M_w 5.1$ *has occurred while the volume of rock affected corresponds rather to a* $M \sim 6$*, followed by a significant expansion of the focal area during the sequence*. They proposed a main role played by fluids in lowering the normal stress on the fault plane, favouring the aseismic slip, alternated with large brittle-failure events, and also causing *an expansion of the focal area due to an incremental stress accumulation leading to larger ruptures [Hainzl and Fischer, 2002]*. *Cheloni et al.* [2017] showed the aseismic slip proposed by *Passarelli et al.* [2015] using the *Global Positioning System (GPS)* and *Synthetic Aperture Radar (SAR)* data in order to analyze the surface deformation in the area and suggested that *the combination of lower strain rates relative to the adjacent Southern Apennines, and a mixed seismic/aseismic strain release may be a possible scenario capable of increasing the recurrence time of large magnitude events in the Pollino seismic gap.*

CHAPTER 3

RELATIVE LOCATION OF MICROEARTHQUAKES

Sequences of seismic events characterized by low-to-moderate magnitude offer the opportunity to image crustal fault structures, particularly in areas where large earthquakes have not been observed during the last centuries. These sequences can occur either like a single rupture extending for kilometers, followed by *aftershocks*, or like *tectonic earthquake swarms*.

The mechanism behind the occurrence and development of the *seismic swarms* is still not fully understood, although the number of studied swarms is increasing. The main difference between aftershock sequences and seismic swarms is that for the latter a clear mainshock-aftershocks chronological occurrence is missing. The rate of the earthquakes occurrence in a swarm is neither described by the Omori-Utsu law[1] nor by any other equation, but can change randomly in time. The events in a seismic swarm affect volumes larger than the largest event could suggest. They also mainly occur in region of slow deformation alternating with *slow earthquakes*, that are events characterized by aseismic crustal deformation that last for days [*Lohman and McGuire*, 2007; *Peng and Gomberg*, 2010; *Hainzl et al.*, 2012; *Passarelli et al.*, 2015]. Different mechanisms have been proposed for the origin and development of seismic swarms as for instance a migration of fault patches due to the diffusion of pore-pressure lowering the effective normal stress on the fault plane [*Hainzl and Ogata*, 2005], or slow slip events, driven by pressurized fluids, redistributing the stress along the fault [*Lohman and McGuire*, 2007; *Peng and*

[1]Empirical law proposed by Omori and modified by Utsu, that describes the decrease of the aftershock after a mainshock, following the hyperbolically decay $n(t) = k/(c+t)^p$ where p is a case-dependent parameter usually falling between 0.7 and 1.5.

Gomberg, 2010].

Since small earthquakes may be produced by secondary faults, the analysis of few events, in the case of large earthquakes, may not be representative of the main fault. On the other hand, when thousands of small earthquakes are available, their hypocenters distribution may display the features of the main active fault that produced the swarm. The precise location of low magnitude events is crucial to image the seismogenetic structures responsible for the sequence. Unfortunately, the absolute location of low magnitude events is always challenging and can be affected by high uncertainties, from hundred of meters to more than one km, also in well-instrumented areas. This is due to several reasons: the number of seismic stations and their spatial distribution around the source; the accuracy of the P- and S-wave picking; the low signal-to-noise ratio (SNR) that reduces the number of useful waveforms when locating, increasing the gap and consequently the uncertainty; the use of automatic or semi-automatic softwares to perform the phase picking. These issues may be exacerbated during a seismic crisis, when the seismicity rate is very high, reaching hundreds of event per day. In these cases, the use of automatic softwares for picking direct waves is the standard procedure in seismological centers all over the world. Although this procedure speeds up the localization process, usually increases the uncertainties associated with it. In order to enhance the reliability of these locations, the pickings of the direct waves are often manually revised by an operator. This step could reduce the uncertainties on the catalogue locations, but does not allow to image a seismogenetic structure with high quality.

The use of the *relative location* methodologies allows for more precise hypocenter distributions and, consequently, high resolution image of the seismogenetic fault. Several relative location techniques have been developed in the past decades to reduce the dependence of earthquake location to the Earth velocity structure, which is the main source of errors [*Jordan and Sverdrup*, 1981; *Frémont and Malone*, 1987; *Got et al.*, 1994; *Gillard et al.*, 1996; *Rubin et al.*, 1999; *Waldhauser and Ellsworth*, 2000]. The basic assumption of these techniques is that earthquakes characterized by similar waveforms likely occurs on the same patch of a larger structure. In this case, their magnitudes are comparable and the distance between two different hypocenters is much smaller compared with the respective source-receiver distances. Therefore, the ray paths are so close together that it can be assumed the velocity heterogeneities within the crust crossed by both of them to be the same. As a result, the hypocenter spatial difference one aims to compute translates into a delay of the two P-wave onsets at each station.

Thus, relative location methodologies turned out to be a powerful tool to investigate fault extension, when these assumptions are all fulfilled, as in the case of tectonic sequences and swarms.

The aim of this chapter is to perform the relative location of micro-earthquakes for a high quality image of the structure(s) responsible for the 2010-2014 Pollino seismic swarm, and to compare them with their absolute locations. Moreover, several analysis have been performed in order to assess the reliability of these results and to give new insights on the source mechanism and development of the sequence.

3.1 Cross-correlation analysis

The imaging detail of large fault structures mainly depends on the amount of clusters of similar waveforms achieved using the cross-correlation performed on all the available waveforms at a reference station. The larger this number is, the more seismogenic volume can be imaged, giving accurate information about the fault orientation and the temporal evolution of the sequence. The following subsections propose to illustrate how to obtain clusters of similar waveforms applying the normalized cross-correlation of time-shifted seismic signals. Before that, the cross-correlation and the normalized cross-correlation will be briefly discussed with numerical examples.

3.1.1 Cross-correlation and auto-correlation of discrete signals

In signal processing, the **cross-correlation** is a measure of similarity of two waveforms as a function of a time-lag applied to one of them. Basically the aim is to combine two different waveforms and figure out the similarity between those signals. It has applications in many fields, where detecting similar patterns between different signals is crucial, as in the case of *electron tomography*, *cryptanalysis*, *neurophysiology* and, of course, *geophysics*. The *cross-correlation* works very well when the energies of the two signals are of the same order. For discrete signals, the cross-correlation between x and y is given by the equation

$$Corr_{x,y}(l) = \sum_{n=-\infty}^{\infty} x[n]y[n-l] = \sum_{n=-\infty}^{\infty} x[n+l]y[n] \tag{3.1}$$

where l is the value of the shifting sample in computing the cross-correlation. A numerical example using three discrete signals may clarify how this analysis operates. Three discrete signals are taken: $x = [0,0,4,-2,8,0,0]$, $y = [0,0,10,-3,5,0,0]$ and $z =$

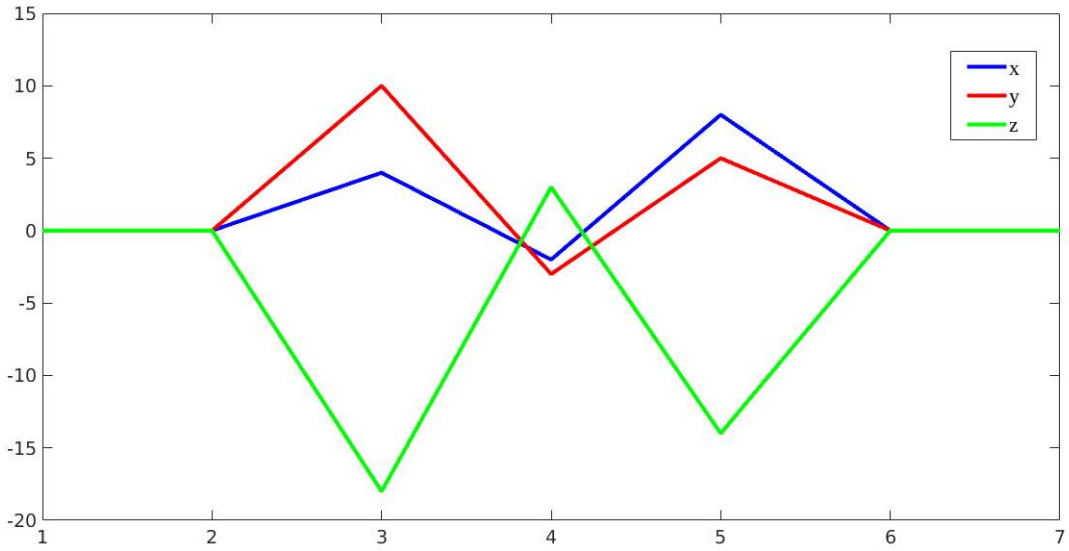

Figure 3.1: Three discrete signals, x, y and z, used to perform cross-correlation and normalized cross-correlation.

$[0,0,-18,3,-14,0,0]$. The choice of these values is not random, as seen later in this paragraph. The signals are shown in Figure 3.1. Taking into account the x and y signals, the computation of the cross-correlation values for $l=-1$, $l=0$ and $l=1$ is shown for instance as follows

$$
\begin{aligned}
&Corr_{x,y}(0) = (0)\cdot(0)+(0)\cdot(0)+(4)\cdot(10)+(-2)\cdot(-3)+(8)\cdot(5)+(0)\cdot(0) = 86 \\
&Corr_{x,y}(-1) = (0)\cdot(0)+(0)\cdot(10)+(4)\cdot(-3)+(-2)\cdot(5)+(8)\cdot(0)+(0)\cdot(0) = -22 \\
&Corr_{x,y}(1) = (0)\cdot(0)+(4)\cdot(0)+(-2)\cdot(10)+(8)\cdot(-3)+(0)\cdot(5)+(0)\cdot(0) = -44
\end{aligned}
\tag{3.2}
$$

The cross-correlation values for each pair of signals at each lag are shown in Table 3.1 and represented in Figure 3.2a. The highest value is reached at $l=0$. The negative values of the cross-correlation between x and z ($cc_{x,z}=-190$) means that these signals are anti-correlated. The same happens between y and z ($cc_{y,z}=-259$).

lag	-6	-5	-4	-3	-2	-1	0	1	2	3	4	5	6
$cc_{x,y}$	0	0	0	0	20	-22	86	-44	80	0	0	0	0
$cc_{x,z}$	0	0	0	0	-56	40	-190	60	-144	0	0	0	0
$cc_{y,z}$	0	0	0	0	-140	72	-259	69	-90	0	0	0	0

Table 3.1: Cross-correlation values computed between the three signals x, y and z for each lag.

In case of signals with a large range of values covered, it is more appropriate to scale the cross-correlation by some factors determined by the energy of the signals that are

analyzed. This is possible introducing the **normalized cross-correlation**, defined by

$$CorrNorm_{x,y}(l) = \frac{\sum_{n=-\infty}^{\infty} x[n]y[n-l]}{\sqrt{\left(\sum_{n=-\infty}^{\infty} x[n]x[n-l]\right)\left(\sum_{n=-\infty}^{\infty} y[n]y[n-l]\right)}} \tag{3.3}$$

where $AutoCorr_{xx} = \sum_{n=-\infty}^{\infty} x[n]x[n-l]$ and $AutoCorr_{yy} = \sum_{n=-\infty}^{\infty} y[n]y[n-l]$ are the **auto-correlation** functions. This function is defined as the comparison of a time series with itself at a different time. It is very helpful in detecting a periodic transient in the signal.

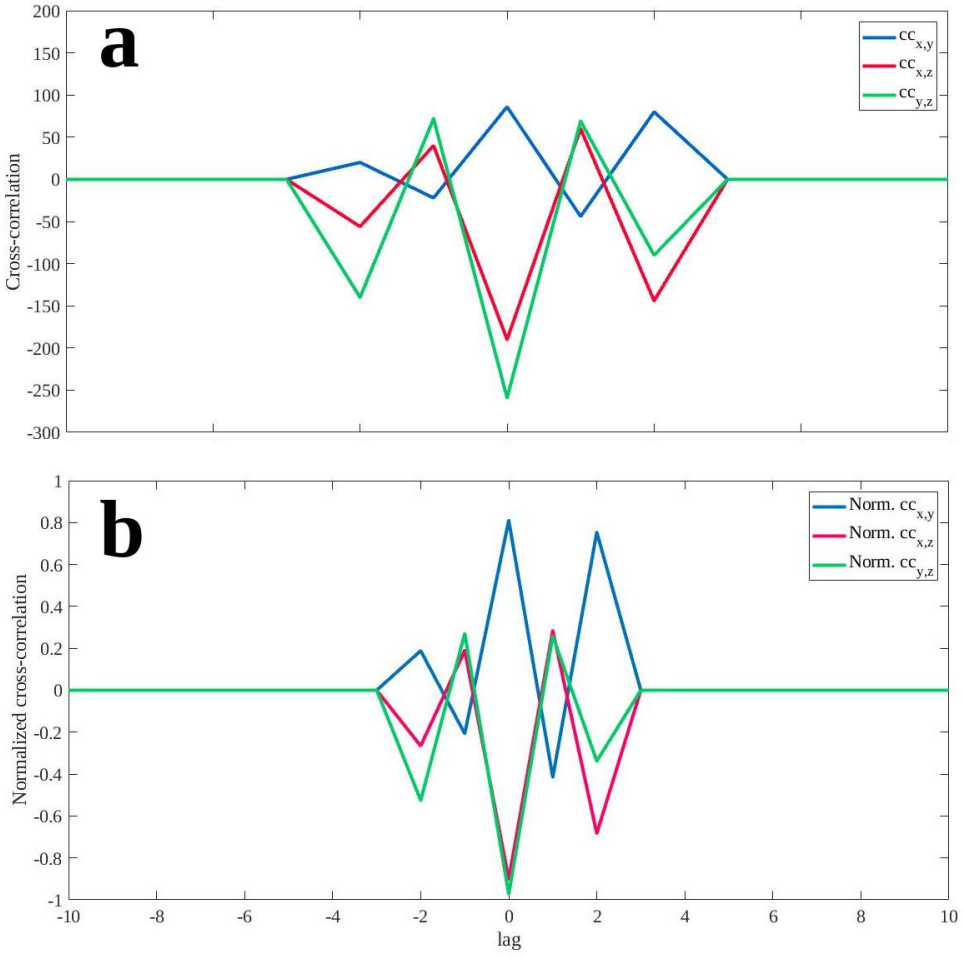

Figure 3.2: Cross-correlation between the three signals are shown in panel a. Normalized cross-correlation of the same signals are shown in panel b, using the same colors.

The normalized cross-correlation values range between -1 and 1, allowing to compare even signals characterized by very different amplitudes, that may happen with seismic waveforms.

lag	-6	-5	-4	-3	-2	-1	0	1	2	3	4	5	6
$cc_{x,y}$	0	0	0	0	0.18	-0.2	0.81	-0.41	0.75	0	0	0	0
$cc_{x,z}$	0	0	0	0	-0.27	0.19	-0.90	0.29	-0.68	0	0	0	0
$cc_{y,z}$	0	0	0	0	-0.53	0.27	-0.97	0.25	-0.34	0	0	0	0

Table 3.2: Cross-correlation values computed between the three signals x, y and z for each lag.

Taking into account the same signals x, y and z, the normalized cross-correlation values for each pair of signals at each lag are shown in Table 3.2 and represented in Figure 3.2b. The results are now directly comparable.

3.1.2 Cross-correlation of time-shifted signals

Performing the normalized cross-correlations on very similar time shifted signals in a cluster, in order to detect their time difference and link it to their spatial distribution, is a task of this work. The value of the lag at which the maximum cross-correlation value is reached defines the time shift between the two signals. Obviously, if they are identical this value is 1.

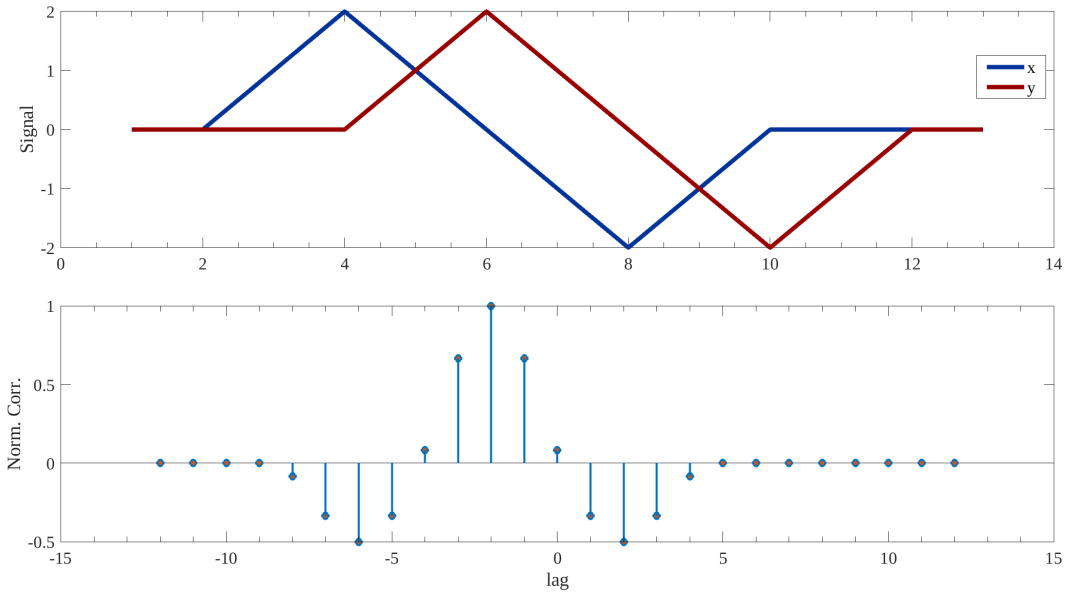

Figure 3.3: Normalized cross-correlation to obtain time lag between two signals. Blue and red lines represent the two identical signals shifted by two samples (upper panel) and the stem plot showing the normalized cross-correlation associated to each lag, for each sample (lower panel).

A practical example may clarify the theory. Two identical signals are taken into account, shifted by two samples (upper panel in Figure 3.3). The maximum value of the normalized cross-correlation ($normcc_{x,y} = 1$) is reached if the red signal shifts by 2 samples to the left, as expected (Table 3.3). This analysis is very efficient to estimate the

lag	-6	-5	-4	-3	-2	-1	0	1	2
cc	-0.5	-0.33	0.08	0.67	1	0.67	0.08	-0.33	-0.5

Table 3.3: Values of normalized cross-correlation for each time lag, shown in the lower panel of Figure 3.3. The points whose cross-correlation value is close to zero are excluded.

time lag between two similar waveforms in the same cluster in order to measure their spatial separation, as shown in the following sections.

3.2 Relative locations

In this work the *master-slave* method, one of the simplest and most reliable methodology to perform relative locations, has been applied. This method is based on the computation of the time differences between a *reference event* (or *master event*) and the current event at each station (*Got et al.* [1994]).

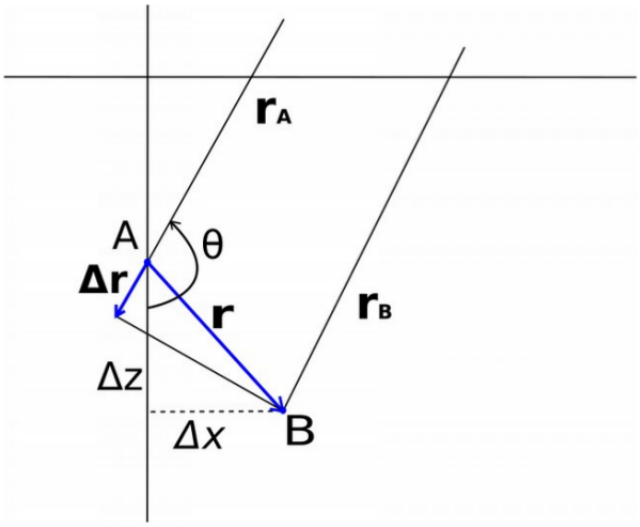

Figure 3.4: Geometrical representation in section XZ of two hypocenters A and B whose distance is much smaller than their distance from the seismic station. θ is the takeoff angle, r_A and r_B are the two source-receiver distances and Δr their difference, the projection of $\mathbf{r}$ on $\mathbf{r_A}$.

During the seismic crisis, different institutions installed and operated seismic stations in the area. Their sampling rate were different. An over-sampling of the selected similar waveforms at 500 samples per seconds is a useful procedure before performing the relative location method. Through this operation the dataset becomes homogeneous and the time resolution of the waveforms increases. In fact, such high sampling yields travel time differences as small as $0.002s$, which corresponds to a hypocenter distance of only $12m$ for P-wave velocity. The normalized cross-correlation has been performed to group the waveforms characterized by similar waveforms. Then the *master event*, characterized by high signal-to-noise ratio among all the earthquakes of the cluster and by the best azimuthal coverage of the seismic stations, was chosen and its absolute location was performed using the code *EqLoc*.

This location method is based on the following assumptions:

- master-slave distance is much smaller than their distance from the seismic station;
- the two events have very similar focal mechanisms;
- the two events are characterized by similar magnitude.

Once it has been established that all the listed assumptions are verified, the master-slave method may be applied. The hypocentral coordinates of two events are called $A = (X_A, Y_A, Z_A, T_A^0)$ and $B = (X_B, Y_B, Z_B, T_B^0)$, respectively. Assuming the previous hypothesis, the travel times for each couple of points $A - B$ of events should be very similar at each station i: $tt_A^i = tt_B^i$.

Consider a Cartesian coordinate system, whose axes are oriented respectively towards *East (X)*, *North (Y)* and *Down (Z positive down)* (Figure 3.4). A seismic ray is uniquely traced assigning two angles: the *take-off angle*[2], θ, and the *azimuth*[3], ϕ. These angles are retrieved by the code *EqLoc*, together with other useful information. The rays connecting A and B to the same seismic station are labelled $\mathbf{r_A}$ and $\mathbf{r_B}$. The position vector from A to B, is then given by $\mathbf{r} = \mathbf{r_A} - \mathbf{r_B} = (\Delta x, \Delta y, \Delta z)$. In first approximation, $\Delta\mathbf{r}$ (Figure 3.4) is the difference between the length of the two ray paths $\mathbf{r_A}$ and $\mathbf{r_B}$, computed as the projection of $\mathbf{r}$ on $\mathbf{r_A}$[4]. Calling their travel times t_A and t_B, the time differences (the

[2]The take-off angle is measured with respect to the vertical, assuming the value of 0 for a ray going directly downward from the source into the earth, and a value of 180 if it propagates upward.

[3]The azimuth is the angle at the source location between the local north and source-receiver direction with values of 0, 90, 180, and 270 representing north, east, south and west.

[4]In geometry, if $\hat{i}$ is a unit vector and $\vec{v}$ an arbitrary vector, the orthogonal projection of $\vec{v}$ along the direction of $\hat{i}$ is the vector $v_{\hat{i}} = (\vec{v} \cdot \hat{i})\,\hat{i}$, whose direction is the same as $\hat{i}$.

waveforms lag) $\Delta t = t_A - t_B$ are given by:

$$\Delta t_k^{AB} = t_A - t_B = \frac{1}{v}(\Delta\vec{r} \cdot \hat{r}_A) \tag{3.4}$$

where $\hat{r}_A = \vec{r}_A/|\vec{r}_A| = (\sin\theta\sin\phi, \sin\theta\cos\phi, \cos\theta)$ in spherical coordinate system. The time differences become:

$$\Delta t_k^{AB} = \frac{1}{v}\left(\Delta x \sin\theta_k \sin\phi_k, \Delta y \sin\theta_k \cos\phi_k, \Delta z \cos\theta_k\right) \tag{3.5}$$

at the k^{th} seismic station. Measuring these time differences for the same master-slave couple at N seismic stations, N equations are obtained. These can be written in the compact matrix:

$$\frac{1}{v}\begin{pmatrix} sin\theta_1 sin\phi_1 & sin\theta_1 cos\phi_1 & cos\theta_1 & v \\ sin\theta_2 sin\phi_2 & sin\theta_2 cos\phi_2 & cos\theta_2 & v \\ \vdots & \vdots & \vdots & \vdots \\ sin\theta_N sin\phi_N & sin\theta_N cos\phi_N & cos\theta_N & v \end{pmatrix}\begin{pmatrix} \Delta x \\ \Delta y \\ \Delta z \\ \Delta T_0 \end{pmatrix} = \begin{pmatrix} \Delta t_1 \\ \Delta t_2 \\ \vdots \\ \Delta t_N \end{pmatrix} \tag{3.6}$$

that is an over-determined system, in the form $\mathbf{Gm} = \mathbf{d}$ where the data vector are the time differences for the same couple of event at different seismic stations and the model parameter, $\mathbf{m} = (\Delta x, \Delta y, \Delta z, \Delta T_0)$. The first three elements of $\mathbf{m}$ represent the distance in km of the current event with respect to the master event, while ΔT_0 represents the origin time shift in seconds between the two events.

The solution to this over-determined problem is given by:

$$m = \left(G^T G\right)^{-1} G^T d \tag{3.7}$$

A code in MATLAB® has been created to perform the inversion and obtain relative location of hypocenters. Extracted azimuth, takeoff angle and arrival times at each station from the absolute location of the master event, these values can be used as inputs in the code. The waveforms have to be band-pass filtered, and a suitable window of analysis has to be chosen. The cross-correlation of these time-shifted waveforms is performed to obtain the data vector and inverted for the spatial distribution of the hypocenters of the cluster using the Equation 3.6 in matrix notation. Then, to assess the reliability of the results and their uncertainties, the same analysis is performed several times changing many times filters, window of analysis and wave phases.

3.2.1 The underestimation of the master-slave distance

One of the main issues when this relative location technique is applied is the well-known underestimation of the real distance between master and slave event. This problem has

been highlighted in several works [*Frémont and Malone*, 1987; *Deichmann and Garcia-Fernandez*, 1992; *Scarfì et al.*, 2003]. The time difference between two events, measured through the normalized cross-correlation of the time-shifted waveforms included into a cluster, do not represent the actual time difference between the P-wave onset at each station that recorded the events. The cross-correlation of a *segment of the signal* is actually performed. This means that also the sharpness of the signals, their energy and frequency content are taken into account in performing the cross-correlation. This values are similar, but of course not identical, among the waveforms of a cluster and this can affect the relative locations. Because the correlation function is given as a sum of the products of corresponding values, all these differences will reflect the lag at which maxima and minima of the signals match best, resulting in a disagreement with respect to the P-wave onset lag that leads to the underestimation of the actual master-slave distance.

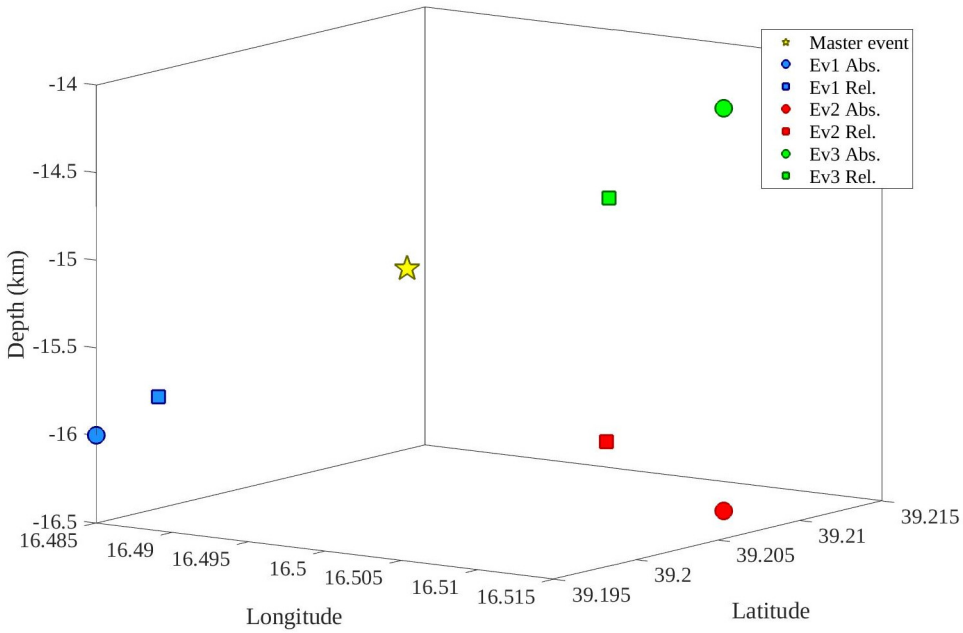

Figure 3.5: Absolute locations of a reference event (yellow star) and of three events (circles). These locations have been compared to their relative locations (squares) with respect to the reference event. Same colors link absolute and relative location of the same event.

This assertion has been proved, performing a synthetic test and comparing the master-slave distances using absolute and relative locations. The synthetic hypocenters have been chosen in the central region of Calabria region, area surrounded by a dense network

of operating stations. Having fixed a priori the locations of sources and receivers, azimuth,

Event	Latitude	Longitude	Depth
Master	39.200	16.500	15.0
Ev1	39.195	16.485	16.0
Ev2	39.2100	16.5100	16.3
Ev3	39.2100	16.5100	14.2

Table 3.4: Absolute locations of 4 events in the central part of the Calabrian Arc. The first is chosen to be the master event.

take-off angle and travel time have been estimated for each event at each station of the network. The *absolute* distances between master and slaves have been computed (Table 3.5). Then, the relative location of the three events compared to the master location have been computed as described in Subsection 3.2 obtaining the *relative* master-slave distances (Table 3.5). The comparison between relative and absolute locations highlights

Event	Δx_{rel}	Δx_{abs}	Δy_{rel}	Δy_{abs}	Δz_{rel}	Δz_{abs}
Ev1	-1.076	-1.3	-0.408	-0.6	0.770	1.0
Ev2	0.441	0.9	0.829	1.1	0.801	1.3
Ev3	0.438	0.9	0.851	1.1	-0.387	-0.8

Table 3.5: Absolute and relative component of three master-slave distances.

in a clear way how the results obtained by the former method, although qualitatively correct, are always different and smaller in absolute value from those obtained by the latter one (Figure 3.5). This example confirms that the relative location methodology underestimates the distances between couples of sources. Encouraging is the perfect agreement between the signs of the components Δx, Δy and Δz obtained applying the two methodologies, where $z - axis$ increases downward.

3.3 The Pollino case of study

Master-slave method for relative location of earthquakes have been applied to part of the seismic events of the 2010-2014 sequence that affected the western sector of the Pollino area. Our aim is a high detailed image of the seismogenic structure responsible for the sequence. These are compared with the results obtained from the absolute locations computed in previous papers in the same area. Moreover, the source mechanisms were computed, and the development of the swarm was followed through time and interpreted in terms of the main geological structures of the area.

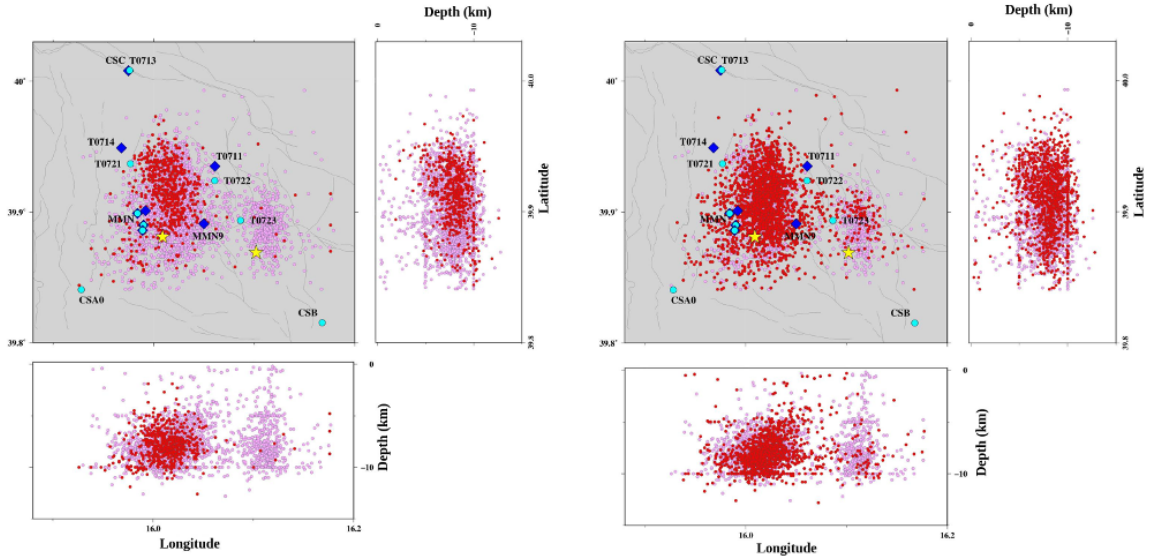

Figure 3.6: Maps of the earthquakes used in this work. Pink circles represent all the hypocenters, located in the catalogue, related to the whole sequence. In the left panel, the red map and cross-section the red circles represent the hypocenters selected in the Period 1, while on the right they represent the hypocenters selected in Period 2. The two stars represent the strongest events of the sequence. Blue diamonds are the seismic stations installed in Period 1, the cyan circles the ones installed in the Period 2.

3.3.1 Data selection

To perform the analysis, 6261 earthquakes of the 2010-2014 Pollino seismic sequence have been selected. These events belong to the two most intense periods of the swarm: November 2011 - April 2012 (*period 1*, 3263 events, left panel in Figure 3.6) and September 2012 - June 2013 (*period 2*, 2998 events, right panel in Figure 3.6).

This selection was performed first running an automatic picker to continuous recordings at a reference station (MMN during the period 1, MMN1 during the period 2)[5], the closest stations to the swarm area, characterized by the highest signal-to-noise ratio. These recordings were collected by the *Laboratorio di Sismologia* of the *Università della Calabria*. The automatic picker used in this work is based on the computation of kurtosis and STA/LTA ratio. This algorithm is very efficient in the identification of any signals characterized by impulsive onset like local earthquakes. Since the seismic stations were installed in the Mormanno village, some of the signals found by the automatic picker were not earthquakes but disturbances of anthropic origin. For this reason, the signals re-

[5]The reference stations are extremely close to each other, the one with the highest number of recordings has always been used.

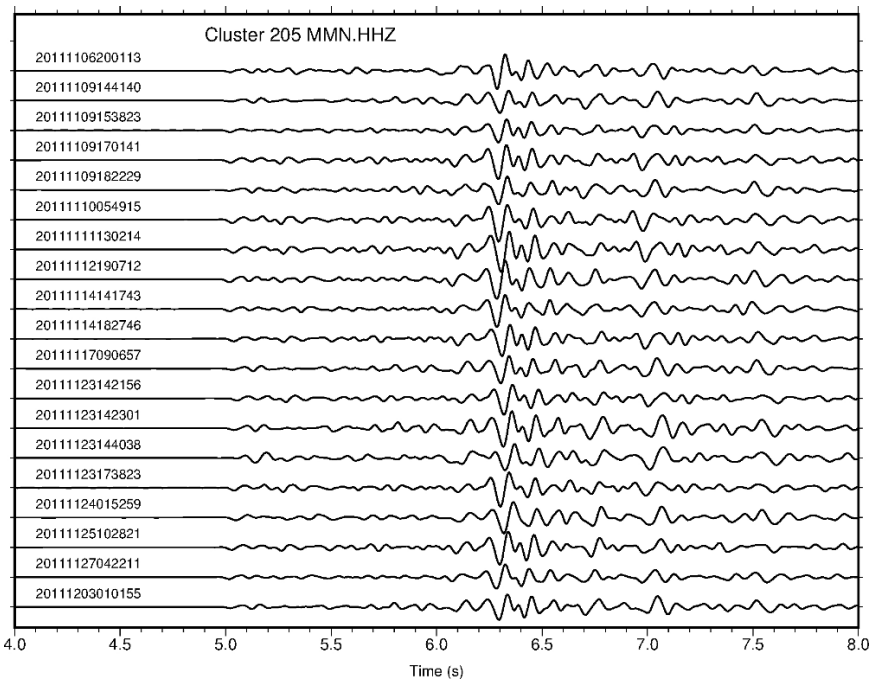

Figure 3.7: Vertical component of similar waveforms of cluster 205, recorded at the reference station MMN.

sulting from the software used for the automatic picking were manually revised, in order to reject any non-seismic event. Then, the P-waves were manually re-picked as precise as possible to align the waveforms. The selection of these two periods was necessary due to the highly changing number of available stations in the area. In period 1, this number reached 12 within an epicentral distance of 50 km. The network comprised permanent and temporary stations operated by *Università della Calabria* and *Istituto Nazionale di Geofisica e Vulcanologia (INGV)* [*Margheriti et al.*, 2013]. As explained in Section 2.3, the temporary stations were removed to be installed in northern Italy to monitor the Emilia earthquake sequence that begun on 20 May 2012. Starting from September 2012, 15 seismic stations operated by *Università della Calabria*, *Istituto Nazionale di Geofisica e Vulcanologia (INGV)* and *GFZ (Geoforschungszentrum, Potsdam, Germany)* [*Passarelli et al.*, 2012], were installed within an epicentral distance of 50 km, allowing for performing the relative location methodology. The selected events were characterized by magnitude ranging between 0.7 and 2.8, epicentral distance between 1 and 50 km, depth between 0 and 25 km (in Figure 3.6 the few events below 15 km were removed to make the cross-section clearer). All these information were estimated using the absolute locations selected from the official Italian Catalogue [*ISIDe*, 2010]. It is evident mainly from the cross-sections of both periods that from these locations was unreasonable to

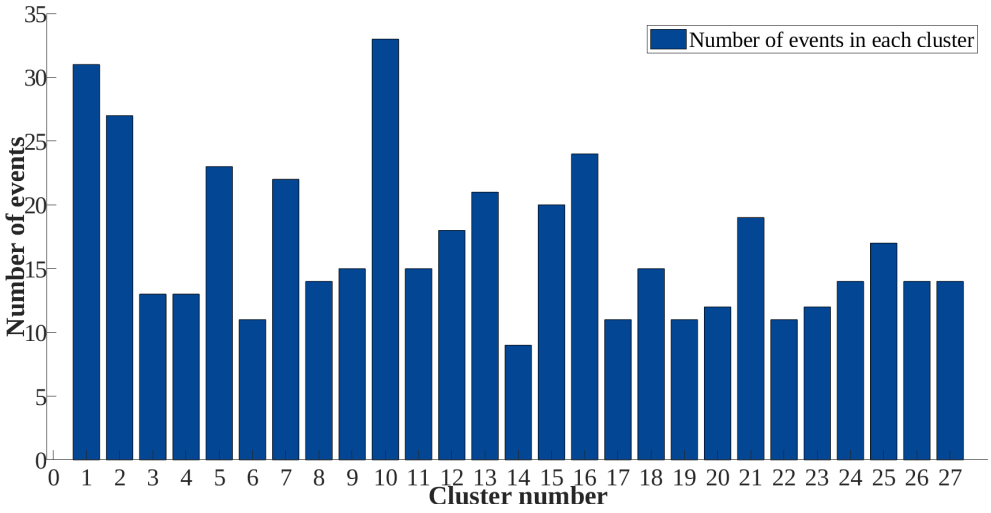

Figure 3.8: Bar graph showing the number of events in each cluster. Clusters 14 and 10 are the ones comprising the lowest and the highest number of earthquakes, 9 and 33, respectively. Clusters 1-18 are referred to Period 1, 19-27 to Period 2.

depict the fault plane responsible for the swarm. Moreover, some locations were clearly fixed to 10 km. This is a well-known issue in seismology, and constitutes a limit in the interpretation of the seismogenic structures.

3.3.2 Cluster selection using cross-correlation analysis

The cross-correlation analysis [*Watts and Jenkins*, 1968] was performed on the selected 6261 events to find earthquake pairs characterized by very similar waveforms at the reference station (Figure 3.7). The cross-correlation was computed on band-pass filtered signals between 1 and 18 Hz on a 3 s window, starting 0.5 s before the P-wave arrival and including the direct phases and the early coda waves. All event pairs characterized by normalized cross-correlation greater than 0.8 (lowered at a later time to 0.75 to add some other events) and RMS[6] greater than 1500 counts at the reference station were selected. These values roughly corresponded to a lower magnitude threshold of $m_L = 0.7$. A minimum number of 5 events per cluster was required.

From this selection 27 clusters (432 earthquakes) were collected: 18 clusters in period 1 (295 earthquakes) and 9 clusters in period 2 (137 earthquakes). The number of events comprised in each cluster ranges from a minimum number of 9 to a maximum of 33, as shown by the bar graph in Figure 3.8. The events that appear in more than one cluster,

[6]The square root of the arithmetic mean of the squares of the values, $RMS = \sqrt{1/n \cdot (x_1^2 + x_2^2 + \cdots + x_n^2)}$

Depth range (km)	$v_P(km/s)$	$v_S(km/s)$
$-1.00 - 0.67$	4.00	2.29
$0.67 - 2.67$	4.42	2.55
$2.67 - 4.67$	4.69	2.71
$4.67 - 6.67$	5.23	3.02
$6.67 - 12.34$	6.00	3.46
$12.34 - 18.34$	6.12	3.53
$18.34 - 30.00$	6.38	3.68
$30.00 - 36.67$	7.69	4.44
$37.67 - 43.34$	7.70	4.45
$43.34 - 60.00$	7.73	4.46
$60.00 - 210.00$	8.10	4.62

Table 3.6: Velocity model by *Barberi et al.* [2004], used in this work

due to their proximity in space, were retained only once. However, these common events were useful to assess the reliability of the locations being the link between two or more close clusters.

3.3.3 Single cluster analysis

For each cluster all the waveforms recorded by all the available stations for each event revealed by the cross-correlation analysis were collected and stored. They were visually inspected. Among them, the *master event* was chosen by considering high magnitude and signal quality, number of recording stations and their azimuthal coverage.

Adopting the velocity model by *Barberi et al.* [2004] (Figure 3.9), the absolute location of the *master event* was computed using the code $EqLoc$ (Table 3.7).

The waveforms were over-sampled at 500 sps to increase time resolution. Then, relative locations of each master-slave couple of each cluster were performed as explained in details in Section 3.2. To assess the stability of the hypocenter locations and the reliability of the methodology, two band-pass filters ($\Delta f_1 = 2 - 15\ Hz$ and $\Delta f_2 = 2 - 12\ Hz$) and two different windows have been chosen to perform the cross-correlation analysis between master and slaves ($w_1 = 2s$ and $w_2 = 3s$). The windows started 0.3 s before P-wave arrivals and S-wave arrivals. In this way, eight positions for the same event could be estimated, giving an idea about the uncertainties of the hypocenter locations.

The error estimate is not straightforward, due to the many parameters that can affect the locations: the accuracy when locating the master event, the resulting azimuth and takeoff angles, the number of the seismic stations and their spatial distribution in the

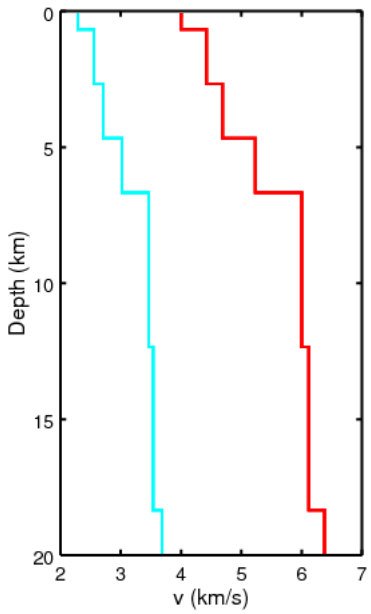

Figure 3.9: Velocity model by *Barberi et al.* [2004], used in this work to perform the absolute locations.

area, the SNR of the events, the synchronization of the instruments. The cross-correlation value approximately decreases for increasing distances. The highest is this value, the smallest is the spatial distribution of the eight locations of the same hypocenter, obtained changing band-pass filters, windows of analysis and wave phases. The error, equally distributed over the three components, ranges from 20 m for the closest hypocenters to the master event, characterized by the highest cross-correlation value, to $150-200$ m for the farthest points, characterized by the smallest cross-correlation values. Differently from the absolute location method, the vertical component does not show a higher error if compared to the horizontal components.

Best fitting plane Results of relative locations were plotted in 3D space, and then fitted by a plane to find the orientation of the fault that likely produced these similar earthquakes (example in Figure 3.10). This was possible measuring two of the three angles that identify a fault plane: *strike* and *dip* angle. The strike represents the fault-trace direction in decimal degrees, ranging from 0 to 360, relative to North, defined so that the fault dips to the right side of the trace. The dip is the angle between the fault and the horizontal plane, ranging from 0 to 90 degrees, relative to horizontal [*Aki and Richards*, 2002]. Basically, by intersecting the horizontal plane, representing the free

Cluster	Event	M_L	Date	Hour	Latitude	Longitude	Depth(km)	RMS	GAP
205	20111112190712	1.5	20111112	19:07:16.271	39.91897	16.00699	5.583	0.035256	241.4
483	20111123015535	1.6	20111123	01:55:38.596	39.92657	16.00477	5.929	0.061268	135.8
526	20111123150700	1.0	20111123	15:07:03.240	39.91253	16.01230	6.659	0.179041	140.6
705	20111124195324	1.4	20111124	19:53:27.418	39.90809	16.03643	6.663	0.341861	107.5
886	20111128151608	1.3	20111128	15:16:11.464	39.92137	16.00760	6.215	0.085898	114.8
911	20111129064101	1.1	20111129	06:41:04.394	39.93245	16.00536	6.086	0.220050	129.2
914	20111129093126	1.2	20111129	09:31:29.758	39.92131	16.01148	6.455	0.186071	131.4
1168	20111203130411	1.0	20111203	13:04:14.663	39.93285	16.01165	4.508	0.146903	113.0
1175	20111203160508	1.5	20111203	16:05:11.608	39.92862	16.00770	5.944	0.213259	103.0
1262	20111205035916	1.6	20111205	03:59:20.057	39.92923	16.00373	4.280	0.116462	106.2
1631	20120102121739	1.5	20120102	12:17:42.398	39.91368	16.01298	6.104	0.020663	103.1
1842	20120115230517	1.3	20120115	23:05:21.085	39.92597	16.01502	5.073	0.211732	135.5
1904	20120116225045	1.3	20120116	22:50:48.374	39.93464	16.01255	5.307	0.342682	88.7
1918	20120117050224	1.6	20120117	05:02:27.838	39.91945	16.01616	6.500	0.248833	97.2
1937	20120117142935	1.5	20120117	14:29:39.065	39.94033	15.99993	5.644	0.199260	117.0
2031	20120122111225	1.2	20120122	11:12:28.909	39.91173	16.01822	5.789	0.195031	100.5
2032	20120122113854	1.9	20120122	11:38:58.287	39.91544	16.02134	5.606	0.222025	101.7
2480	20120214153256	1.4	20120214	15:33:00.300	39.92012	16.00108	5.118	0.176177	147.6
197	20121007212603	1.3	20121007	21:26:06.465	39.92093	16.00013	6.090	0.079316	155.8
1003	20121029165220	1.9	20121029	16:52:24.482	39.90088	15.97508	4.874	0.015822	144.9
1257	20121113223550	1.4	20121113	22:35:54.160	39.89128	16.01611	3.310	0.098207	125.6
1274	20121114090459	1.8	20121114	09:05:02.592	39.91020	16.02226	4.046	0.064578	97.4
1344	20121116223134	1.2	20121116	22:31:37.310	39.88564	16.02909	4.521	0.263716	109.8
1483	20121121231711	1.3	20121121	23:17:14.316	39.90840	16.02646	5.952	0.355406	98.2
1538	20121123103526	1.4	20121123	10:35:29.598	39.91209	16.00799	4.887	0.058256	102.9
1552	20121123220130	1.4	20121123	22:01:33.908	39.91653	16.00688	5.398	0.099930	84.2
1696	20121125231433	1.4	20121125	23:14:36.655	39.91307	16.00739	6.038	0.076533	79.1
1978	20121204105615	1.9	20121204	10:56:18.213	39.91146	16.02122	5.361	0.126875	119.2

Table 3.7: Absolute location of all the master events obtained using *EqLoc* and the velocity model by *Barberi et al.* [2004]

surface of the Earth, described by the equation $z = 0$ with a generic plane in 3D space, described by $ax + by + cz + d = 0$, the resulting fault plan is described by

$$f(x, y) = ax + by + d \tag{3.8}$$

from which strike S and dip D are

$$S = \arctan\left(-\frac{b}{a}\right) \qquad D = \arctan\sqrt{a^2 + b^2} \tag{3.9}$$

Duration magnitude Many earthquakes occurred during the most intense periods of the swarm, were not present in the official catalogue [*ISIDe*, 2010]. Missing the detection of some earthquakes during intense swarms is very common, either because of their small magnitude or because they occur one after another in a very short time. For sake of completeness, beside computing their location also their *duration magnitude* were estimated. The logarithm of RMS of band-pass filtered signals ($1 - 20\ Hz$), averaged

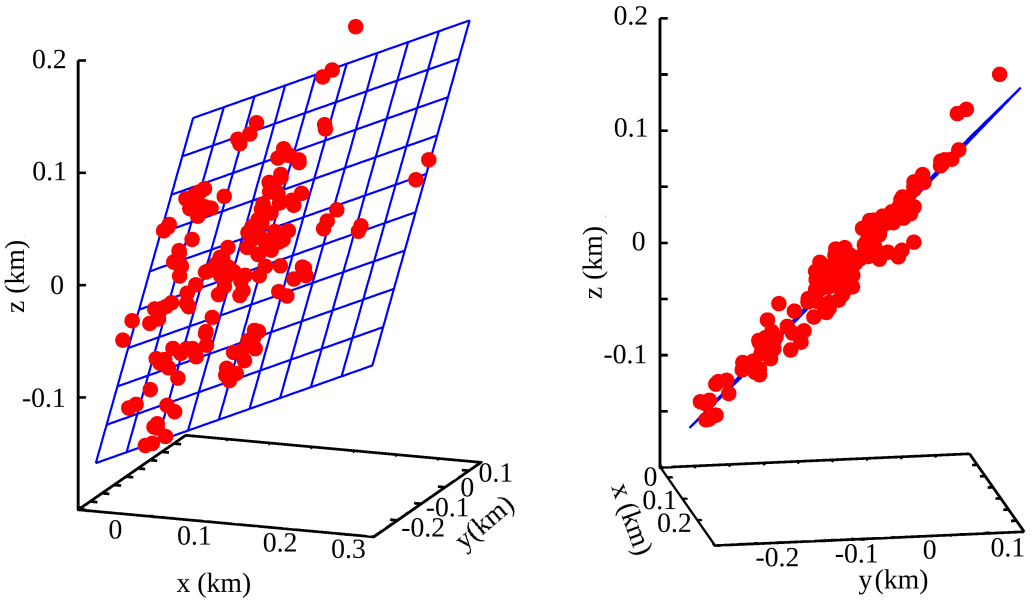

Figure 3.10: Example of results of hypocenters (red circles) located with respect to a master event and best fit plane computed (blue plane). The cluster extension is $300m \times 300m$.

among the three components were plotted. The assumption is that the event ends when the S-coda amplitude returns to the seismic noise level preceding the event [*Sato et al.*, 2012]. The duration magnitude has been computed through the empirical equation

$$M_d = a \cdot log(d) + b \tag{3.10}$$

where d is the duration in seconds, and $a = 2.2$ and $b = -1.4$ are two coefficients, estimated for the Pollino area by comparing the computed M_d with the M_L of the events shown in the catalogue [*ISIDe*, 2010]. In some cases a discrepancy of $0.1 - 0.2$ was found between M_L and M_d for the same event, but overall they are strongly in agreement. The use of these parameters was justified and the results were reliable.

Focal mechanisms and synthetic seismograms Focal mechanisms of several events associated to each cluster have been computed by using the software *FOCMEC* [*Snoke*, 1984, 1989]. Azimuth, take-off angles and the P- and, whenever possible, S-waves polarities have been computed at all the stations characterized by a high signal-to-noise ratio, taking into account the output of the location procedure *EqLoc*. In some cases the waveform similarity has been useful to improve the SNR of the smallest events through the signal stacking, to facilitate the detection of direct wave polarities, especially

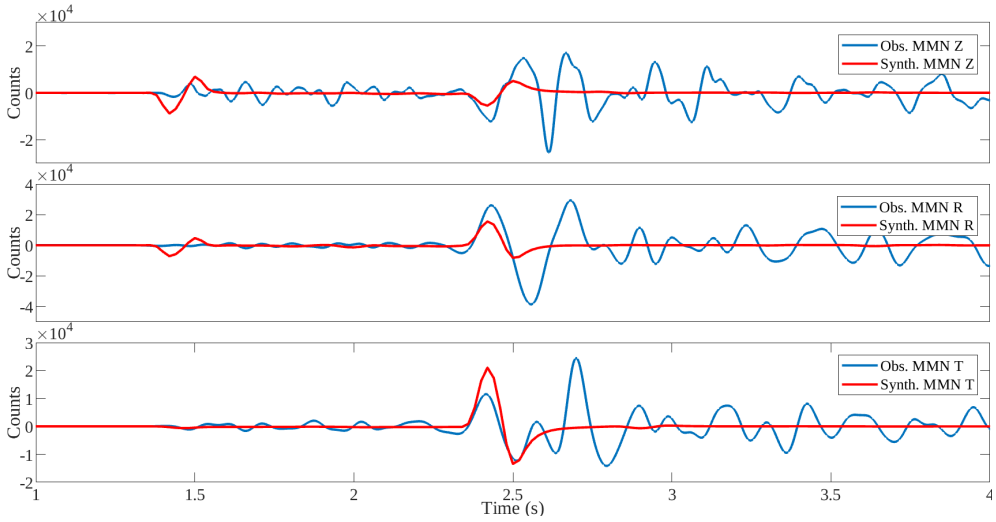

Figure 3.11: Example of a synthetic seismogram (red line) computed for using vertical, radial and transverse components at the station MMN, compared with the observed seismogram (blue line) for the master of cluster 1552.

in case of recordings at the farthest stations. In previous papers about the 2010-2014 swarm in the Pollino area, several focal mechanisms of the strongest earthquakes were computed ($M > 2.7$, *Totaro et al.* [2015]; *Passarelli et al.* [2015]). Here, focal mechanisms characterized by the reduction of the magnitude threshold from M2.7 until M1.2 were computed, increasing the number of mechanisms and thus favouring the knowledge of the source properties.

Furthermore, the focal mechanisms computed here have been used as first input, together with the azimuth and the epicentral distance, to compute the *synthetic seismograms* at different stations (an example is shown in Figure 3.11), using *Computer Programs in Seismology* [*Herrmann*, 2013]. The results of focal mechanisms were confirmed by synthetic seismograms. In few cases a slight rotation of the fault plane was needed to improve the similarities with the real seismograms. The final focal mechanisms were compared to the best fit plane of each cluster in order to assess the reliability of the results.

Absolute locations of all the events of the clusters The events selected from the official Italian catalogue [*ISIDe*, 2010] to perform this analysis, as explained in Section 3.3.1, highlighted some issues with regards to several hypocenter locations, frequent problems when a sequence lasts for years with peaks of hundreds of earthquakes per day. For these reason, semi-automatic programs to perform absolute locations are

routinely used, resulting often in questionable locations. To overcome these issues, the absolute locations of all the events within the clusters have been also performed in order to clarify the improvement of the hypocenter locations. This step was crucial to fill the catalogue with events lost during the swarm because of their small magnitude or temporal proximity. The code $EqLoc$ was used for this purpose and the results of the locations were compared with the ones obtained using another software *HYPOSAT*. More than one hundred locations were compared. The uncertainties estimated using *HYPOSAT* were approximately $dx = dy \simeq\ 200 - 700m$ and $dz \simeq\ 0.8 - 2\ km$. The wide range of values depends mainly on the seismic network configuration changed many times, and on the number of recordings of the event. Relying on the location similarity between the two codes, $EqLoc$ has been chosen to perform all the absolute locations. This code has also the advantage to compute azimuth and take-off angles, needed for relative location and focal mechanisms. Finally, these new absolute locations have been compared to the hypocenters obtained applying the relative location technique to appreciate the enhancement.

3.3.4 Relative location of master events

After the relative location of the earthquakes within each cluster were performed, a comparison of the location of the master event of each cluster with the ones of the other clusters was needed in order to improve the image of the seismogenic volume responsible for the Pollino swarm. Several issues came up applying the re-location technique to master events. The different configuration of the seismic network between the two selected period did not allow to just perform the relative location using the master events of all the clusters within the two periods. Useful information about the proximity of events belonging to cluster of the two different periods were achieved by performing the normalized cross-correlation between them to search for similar waveforms. Some of the events of clusters occurred in period 2 joined clusters of period 1, bringing the information that those two clusters should be the same one or at least very close to each other. The second issue was the dissimilarity of the waveforms belonging to different clusters. By applying the relative location method to all the master event, as it has been applied in the case of a single cluster, was not possible. Modifying the procedure was a needed step to make the waveforms as similar as possible among them. The waveforms, over-sampled at 500 sps, were band-pass filtered between $10Hz$ and $20Hz$. Then those signals characterized by negative first impulse were multiplied by -1 in order to make them comparable to each other. The signals were manually cut by retaining only the

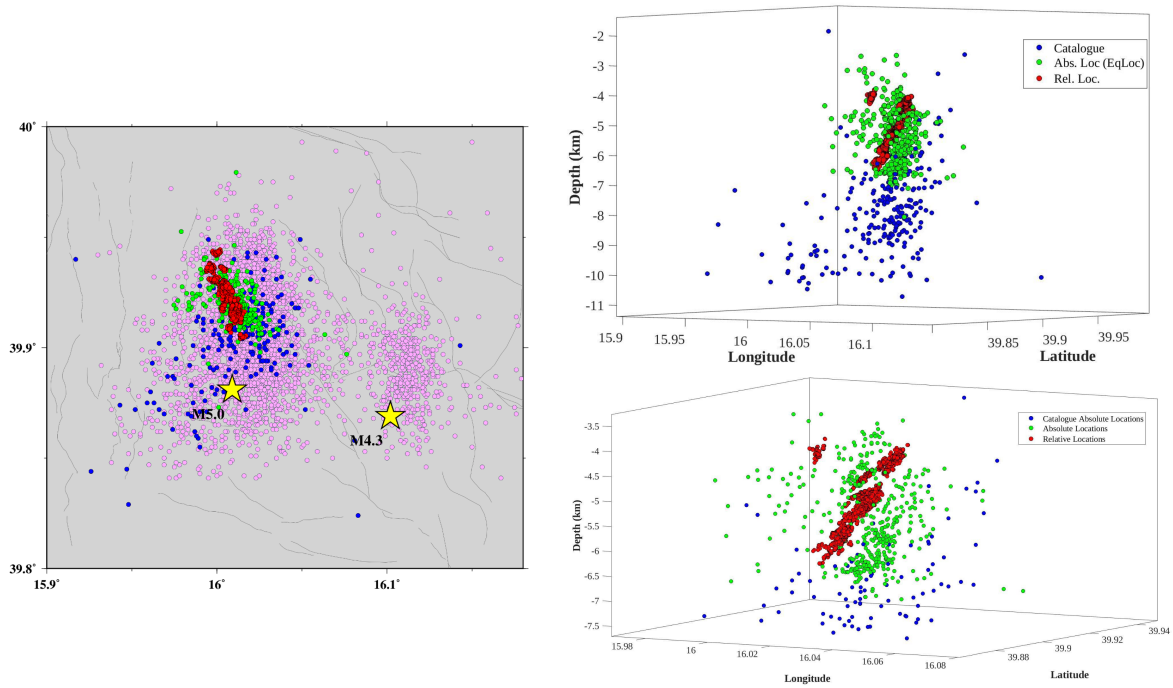

Figure 3.12: Red circles represent the fault plane obtained performing the relative location method. Green circles represent the same events obtained performing the absolute location using the program *EqLoc*, blue circles are the absolute locations of the same events extracted from the Italian Catalogue [*ISIDe*, 2010]. The lower right panel shows an enlargement of the image in the upper panel. The left panel is a map of the same events compared together with the whole sequence (pink circles) and with the two mainshocks (yellow stars).

first 2 pulses after a short window of noise. After this procedure all the signal windows showed the earthquake starting by positive pulses.

The cross-correlation of these signals gave an estimate of the time differences between the current event with respect to the master event, as has been done for each single cluster re-location. (Section 3.2). This step enhanced the seismogenic volume imaging.

3.3.5 Results and interpretation

Relative location of the selected clusters of similar waveforms, occurred during the 2010-2014 Pollino seismic swarm, were performed in order to image with high resolution the structures responsible for the sequence, and to follow its evolution in space and time. Figure 3.12 shows the most straightforward result of the whole analysis, that is the enhancement of the hypocenter locations when applying the relative location

technique with respect to the absolute locations. In this Figure the red circles represent the hypocenter locations resulting by the application of the relative location technique. These locations were compared with the absolute location of the same events achieved from the catalogue (blue circles) and located using *EqLoc* (green circles). As explained in subsection 3.3.2, the number of hypocenters achieved using relative and absolute location in this work is 432. The same earthquakes were searched in the catalogue. Only 223 events, that is around the 52% of the 432 earthquakes located in this work, have been found (blue circles in Figure 3.12). The lack of almost half of these events is due either to their low magnitude or to their short time separation (or even overlap) in periods of intense seismic activity. Furthermore, Figure 3.12 shows that the hypocenters from the catalogue are very scattered and they occupy a volume larger than the absolute location computed in this work. The reason of this difference is related to the fact that the catalogue locations are obtained by semi-automatic softwares. Commonly, the locations are checked by different researchers, that use different techniques to pick the waveforms, increasing the uncertainties. The image is enhanced but not enough to interpret it in terms of clear seismogenic fault structure. The real powerful improvement is obtained by performing the relative location of these events. Through the use of this technique the hypocenter locations of these hypocenters basically collapse into a clear seismogenic volume.

The fault obtained re-locating the different clusters has been fitted with a plane to give an idea about the structure orientation in space (Figure 3.13). The color gradient of the circles has been applied in order to give an additional information about the distance of each hypocenter to the fitting plane: from white to red for increasing distances. The fault plane, obtained excluding the two southern detached clusters that likely belong to another structure, is fitted by the plane of equation

$$f(x,y) = (0.95 \pm 0.01)x + (0.56 \pm 0.01)y - (0.15 \pm 0.01) \tag{3.11}$$

From Eq 3.9, strike and dip angles can be estimated as follows

$$Strike = 150^\circ \qquad Dip = 48^\circ$$

The fitting plane suggests a structure oriented NW-SE, dipping towards the Tyrrhenian Sea with a intermediate dip angle around 48°. The distance of these hypocenters from the fitting plane is at most 500 m, likely depicting a single seismogenic volume, characterized by an area $5 \times 2\ km^2$. The volume is located 4.5 km east from the village of Mormanno (Cosenza), at depth between 4.5 and 6.5 km b.s.l. The overall focal

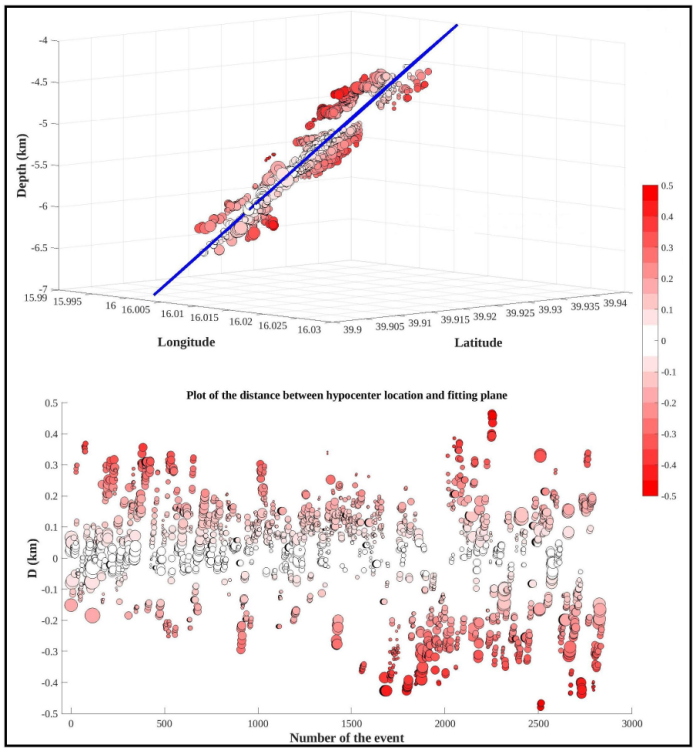

Figure 3.13: *Upper panel:* cross-section of the seismogenic volume found in this work, coloured from white to red as frequency increases. Blue plane is the fit plane. *Lower panel:* distance of each hypocenter from the fit plane. The palette is exactly the same as the upper panel.

mechanism of this structure and the one estimated for the mainshock of the swarm ($M5.0$), likely occurred southern on the same structure, match pretty much perfectly: $(s,d,r) = (166,47,-84)$. The focal mechanisms of the strongest events of the swarm ($M > 2.7$) have been computed in previous works [*Totaro et al.*, 2015; *Passarelli et al.*, 2015]. The number of focal mechanisms has been increased by adding other beach balls of the master events (Figure 3.14), whose size is smaller and whose location more reliable. Table 3.8 shows the comparison between the focal mechanisms computed using FOCMEC, checked using synthetic seismograms computed at different stations for most of the events, and the best fit plane estimated using the relative locations of the hypocenters of each cluster.

The analysis of the rake angles indicates a source mechanism of normal faults for each cluster, in some cases with a strong lateral component of the motion. A substantial agreement between focal mechanism and best fit plane has been found for each cluster. The few discrepancies between the respective angles (Table 3.8) have to be referred to a

	FOCMEC + synthetic seism.			**Best fit plane**	
Cluster	**Strike** (°)	**Dip**(°)	**Rake**(°)	**Strike**(°)	**Dip**(°)
205	120 ± 15	40 ± 10	-70 ± 10	118	36
483	150 ± 5	49 ± 5	-120 ± 10	153	36
526	120 ± 5	48 ± 5	-156 ± 5	166	37
705	118 ± 10	60 ± 10	-128 ± 5	128	32
886	135 ± 20	48 ± 5	-120 ± 20	147	37
911	131 ± 5	49 ± 5	-145 ± 5	155	40
914	151 ± 5	55 ± 5	-137 ± 5	153	35
1168	143 ± 20	68 ± 20	-129 ± 20	134	37
1262	145 ± 10	52 ± 5	-123 ± 5	105	37
1631	152 ± 5	55 ± 5	-98 ± 5	142	55
1842	162 ± 10	45 ± 5	-105 ± 10	155	38
1904	130 ± 20	58 ± 15	-120 ± 10	165	37
1918	115 ± 5	57 ± 5	-129 ± 5	145	38
1937	150 ± 20	45 ± 15	-100 ± 15	135	38
2031	130 ± 10	55 ± 10	-139 ± 10	131	29
2032	105 ± 5	45 ± 5	-76 ± 5	120	35
2480	112 ± 20	44 ± 20	-125 ± 20	108	47
197	140 ± 10	60 ± 10	-70 ± 10	123	43
1003	210 ± 20	80 ± 20	-20 ± 20	165	49
1257	165 ± 10	41 ± 10	-70 ± 10	110	35
1274	202 ± 20	66 ± 20	-19 ± 20	169	30
1344	20 ± 20	55 ± 20	-20 ± 20	120	35
1483	216 ± 20	73 ± 20	-14 ± 20	198	45
1538	173 ± 10	41 ± 10	-70 ± 10	159	35
1552	175 ± 10	42 ± 5	-50 ± 5	128	60
1696	170 ± 10	50 ± 10	-60 ± 5	155	36
1978	222 ± 20	57 ± 20	-5 ± 20	160	30

Table 3.8: Focal mechanisms in the central column, obtained for the masters of each cluster using the program FOCMEC and improved computing synthetic seismograms. Right column shows strike and dip obtained computing the best fit plane using relative locations.

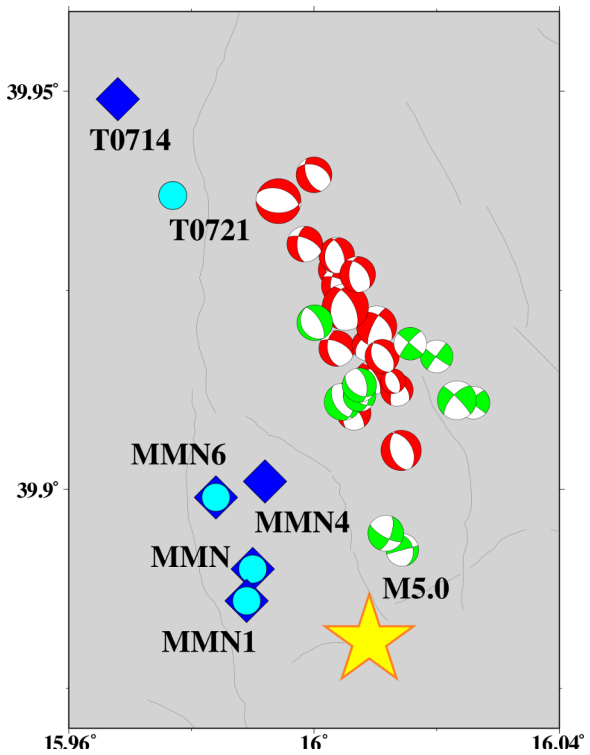

Figure 3.14: In the Figure, red and green beach balls represent the source mechanisms of the first and second period events, respectively. Seismic stations of the first and second period of analysis are shown using blue diamonds and cyan circles, respectively. The yellow star is the mainshock of $M5.0$.

barely sufficient number of available phases because of their low signal-to-noise ratio. Strike angles estimated through focal mechanisms range from 100° to 180° and dip angles between 30° and 60°. These results confirm the focal mechanisms computed in previous works using the strongest events ($M_L > 2.7$) of the seismic sequence. Moreover, they improve the knowledge about the complexity of the rupture process, revealing different fault patches orientations along the same seismogenic volume. Very few clusters, likely belonging to lateral small branches, deviate from the main structure direction.

Moreover, the analysis also allows to follow the time development of the sequence with extreme precision. This is an interesting analysis not only for this certain swarm but to give new insights about the process behind the development of a seismic swarm-like sequence, still not fully understood. The Pollino swarm moved along the achieved seismogenic volume in the two considered periods (Figure 3.15). Unfortunately the sequence evolution cannot be followed from the beginning to the end due to the lack of a sufficient number of stations in some periods. However, many information can be

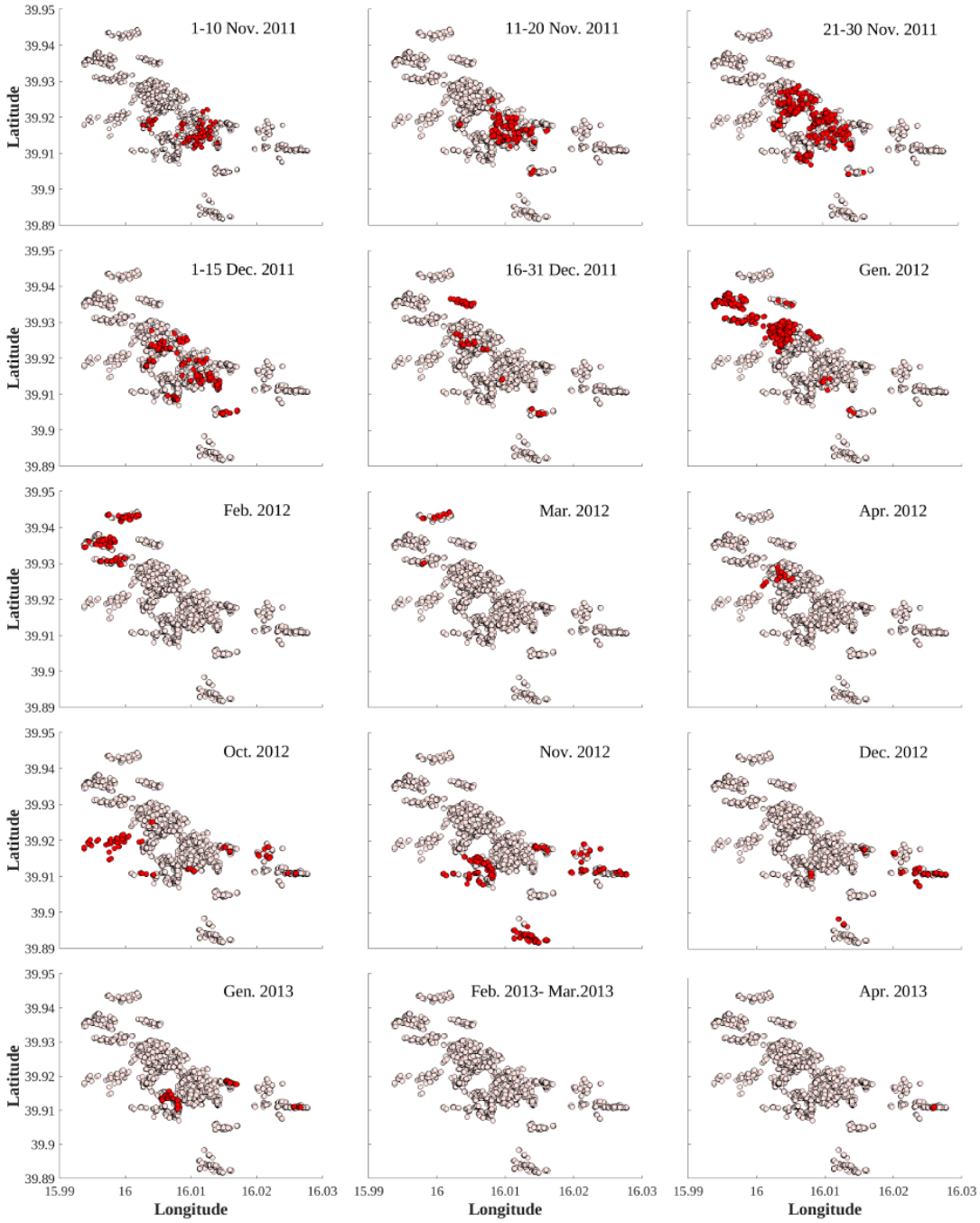

Figure 3.15: Top view of the time development of the Pollino swarm in the two considered periods. The events occurred in each time window are highlighted using red color.

achieved in these considered time windows. Apparently, the swarm started to nucleate from approximately the center of the seismogenic volume, and then it expanded in all the directions around the nucleation area during the first two analyzed months (November 2011 - December 2011). From the middle of December 2011 to April 2012, last month with a sufficient number of stations, the hypocenters migrated northwestward. From October 2012 the seismicity started to fill deeper areas on the western sector and shallower areas on the eastern side of the seismogenic volume, widening the focal area.

A serious issue is the lack of the temporary stations at the beginning of the swarm and between the two selected periods (May - August 2012). In these time windows is not possible to apply the relative location methodology. But it is know from *Passarelli et al.* [2015] and *Totaro et al.* [2015] that in this time range the seismicity migrated mainly on the eastern fault. It started on 28 May 2012 with the $M4.3$ event, followed by aftershocks and lasted for just one month. For this reason the results are likely a true representation of the evolution of the whole swarm on this seismogenic volume, apart from the very first day at the beginning of the sequence.

New insights about the nucleation, mechanism and development of the sequence may be given integrating these results with previous geological and statistical works. Locations and focal mechanisms are in agreement with the transtensional stress regime of the region. Moreover, the assertion that the $M5.0$ event likely occurred on the southern edge of the same seismogenic structure imaged using relative locations, the seismogenic volume activated during the whole swarm should be capable of stronger events. This option cannot be excluded in the future, even though in this area of slow strain swarms are quite recurrent. This work could be relevant for seismic risk assessment and mitigation of the Pollino area and helpful in order to improve the knowledge of seismic swarms.

3.3.6 Conclusions

The relative location methodology is a powerful tool to image with high detail fault structures in tectonic environment or in exploiting geo-resources. In well-instrumented seismically active areas these results could be greatly improved, giving new insights on the fault system geometry, very difficult to guess from the absolute location of hypocenters. The computation of the focal mechanisms confirmed by synthetic seismograms make the results more reliable. The number of hypocenters was also proper to follow the evolution of the swarm, improving the knowledge of the rupture process.

It has been pointed out that within the two selected periods the swarm occurred on a $5 \times 2 \times 2km^3$ seismogenic volume, whose heterogeneity is shown by the different

orientations of its fault patches. The fault is located at a depth between 4.5 and 6.5 km, and it is characterized by normal fault mechanism. Moreover, the focal mechanism and location of the mainshock of $M5.0$ suggests that this events likely occurred on the same seismogenic volume, widening the focal area.

CHAPTER 4

SEISMIC SCATTERING AND ABSORPTION MAPPING

Amplitude and shape of the waveforms allow for an investigation about the interior of the Earth and of the geological structures within. The waveform variations in amplitude can be modelled taking into account different phenomena that occur during the wave propagation, such as the *geometrical spreading*, *reflection and transmission at interfaces*, *scattering* and *intrinsic attenuation* (also called *absorption*).

Geometrical spreading is the phenomenon through which the amplitude of a wave decreases with increasing distance. As soon as the seismic source triggers an earthquake, the seismic energy (E_0) spreads out from the source volume as spherical wavefronts, in an ideal homogeneous and isotropic medium. Each wavefront contains a constant amount of energy ($E(r) = E_0/2\pi r$) distributed on a spherical surface of radius r. The relationship between the energy E and the amplitude of seismic waveforms A is $E(r) \propto A^2$. By linking the last two equations trough $E(r)$ it turns out that $A \propto 1/r$, which means that an earthquake produces less damages as the hypocentral distance increases, if no site effects occur.

The *reflection and transmission at interfaces* occur any time a wavefront strikes an interface between two materials with different physical properties. A percentage of the seismic energy is reflected back, while the residual energy is transmitted through the interface, resulting in the decrease of the seismic energy along the ray path. The reflection (R) and transmission (T) coefficient are thus defined as follows

$$R = \frac{A_1}{A_0} = \frac{Z_2 - Z_1}{Z_2 + Z_1} \qquad -1 \leq R \leq 1$$

$$T = \frac{A_2}{A_0} = \frac{2Z_1}{Z_2 + Z_1} \qquad 0 \leq T \leq 2$$

where A_0, A_1 and A_2 are the incident, reflected and transmitted wave amplitudes, linked through the equation $A_0 = A_1 + A_2$, and Z is the *acoustic impedance*[1] of the two materials. Hence, a wavefront that propagates in media characterized by different properties loses energy due to reflection and transmission.

The aim of this chapter is to investigate *scattering* and *absorption* (or *intrinsic attenuation*) contribution to the total attenuation of the seismic waves [*Sato et al.*, 2012]. While the former causes energy loss and amplitude attenuation due to the presence of small-scale heterogeneities, the latter is related to anelastic processes and internal friction, resulting in heat dissipation. The absorption contribution depends mainly on temperature, melt or fluid content, and chemical composition [*Calvet and Margerin*, 2013]. The resulting envelope of seismic waveforms in randomly heterogeneous media is a combination of both scattering and absorption contributions [*Saito et al.*, 2005; *Calvet and Margerin*, 2013].

At crustal scale, the broadening of body wave-packets, a direct measure of multiple forward scattering, is calculated in this work using the *peak-delay time methodology* [*Takahashi et al.*, 2007] (for the mathematical definition refer to section 4.2). The peak-delay method has been used to characterize the scattering properties of the Japanese lithosphere [*Saito et al.*, 2002; *Takahashi et al.*, 2007, 2009], in continent like North America or subduction zones, as well as Kamchatka and Japan [*Petukhin et al.*, 2003; *Tripathi et al.*, 2014]. The *coda waves*, scattered by random heterogeneities in the subsurface arriving at the tail of the seismogram, are the main manifestation of the redistribution of seismic energy caused by multiple scattering. The strength of coda waves attenuation is measured by the *inverse coda quality factor*, Q_c^{-1}, obtained from the exponential decay of coda envelopes with time [*Aki and Chouet*, 1975] (for the mathematical refer to section 4.3). In recent studies, the joint measurements of peak-delay and Q_c^{-1} methodology have been widely applied in order to separate scattering from absorption attenuation [*Calvet et al.*, 2013] in reconstructing local-to-regional scale tectonic interactions or in localizing sources feeding volcanism. Different strategies have been developed to image coda attenuation in the lithosphere: the standard regionalization approach [*Calvet et al.*, 2013; *De Siena et al.*, 2016], several sensitivity kernel-based approaches [*Prudencio et al.*, 2013; *Obermann et al.*, 2013; *Mayor et al.*, 2014; *Del Pezzo et al.*, 2016], lapse-time-dependent sensitivity kernel-based approach [*Sketsiou et al.*,

[1]The acoustic impedance $Z = \rho V$ is the product of density of the medium and S or P wave velocity.

2020]. In this thesis the second approach has been applied, using the sensitivity kernels by [*Del Pezzo et al.*, 2016] to perform the inversion for the spatial distribution of Q_c^{-1}, while the regionalization strategy has been applied to perform 2D maps of peak-delay.

In this chapter the MATLAB® code *MuRAT* (Multi-Resolution Seismic Attenuation Tomography) developed by Luca De Siena, Associate Professor in Geophysics at the *Johannes Gutenberg Universität (JGU)* in Mainz (Germany), have been used in order to compute the peak-delay time and inverse coda quality factor to assess the lateral variations of scattering and absorption in the Pollino area. Then, the results have been interpreted in terms of main geological features [*Brozzetti et al.*, 2017] and historical seismicity of the area [*Ferranti et al.*, 2017].

4.1 Data pre-processing

Selection and pre-processing of the earthquakes is crucial to obtain reliable results by the code *MuRAT*. The first step of the analysis is the **selection of the area to be investigated**. The success of the analysis mainly depends on the number and distribution of earthquakes and seismic stations in the study area, to gain as much information as possible. Most important is that earthquakes and seismic stations are spread in the whole area in order to obtain as many seismic ray intersections as possible throughout the selected area. These preconditions are mandatory to achieve an appropriate ray coverage to achieve a high level of reliability of the results. The earthquake distribution can preliminarily be ascertained by taking a look at the available catalogue. As in the case under study, seismicity may be more concentrated in some areas and more scarce in others. If a huge number of earthquakes is available, the best ones in terms of high SNR, and number of available waveforms should be selected. Where the seismicity is scarce, it can happen to lower the threshold for their selection, after a visual inspection, in order to achieve as many events as possible. At this step it is useful to write all the station information in the header of the *.sac* file, as for instance latitude (*STLA* field), longitude (*STLO* field) and elevation (*STEL* field).

The second step is the **collection of the waveforms**, recorded by the available stations operating in the area. All the waveforms that comply with some basic requirements are retained: high coda-to-noise ratio, absence of significant trends, absence of overlapping earthquakes altering the coda shape, no signal interruptions or transients due to instrumental problems. These waveforms are cut some seconds before the P-wave

arrival time[2]. Their length depends on the dataset characteristics. Usually around 100 seconds is approximately a good choice in order to take into account the whole coda length.

The last and crucial steps are the **absolute location** of the earthquakes and P- and S-wave **pickings**. When the seismic waveforms are available, this step is mandatory to improve picking and locations of the selected events, lowering the high uncertainties of the information provided by the catalogues, mainly when a sequence occurred with high seismicity rate. The new and more reliable hypocenter locations have to be stored in the header of the *.sac* files (latitude in *EVLA* field, longitude in *EVLO*, depth in *EVDP* and origin time in *OMARKER*); *AMARKER* and *T0MARKER*, the P-wave and the S-wave arrivals, respectively. Origin time, P- and S-wave arrivals are computed in seconds after *KZTIME*, the starting time of the trace.

4.2 Peak-delay time methodology

Waves travelling through the Earth are necessarily involved in processes like multiple forward scattering due to the presence of small and medium size heterogeneities. This is directly expressed by the broadening of the wave-packet that expands as the epicentral distance increases [*Saito et al.*, 2002]. The need of a measure of the strength of multiple scattering resulted in several definitions of the *peak delay-time*. The peak-delay time has been interpreted as *the time lag between the S-wave onset and the maximum amplitude of the waveform*. In Figure 4.1, the difference between T_r, the time at which the envelope reaches the maximum value, and T_S, the time of the S-wave onset, represents the *peak-delay time* definition used in this work. However, this methodology requires the accurate picking of the S-wave phase that in some cases may not be clearly detectable, making their picking really tough. For instance, this is the case of the waveforms in volcanic environment or tectonic swarms characterized by low-magnitude earthquakes. *De Siena et al.* [2016] overcame this issue by defining the peak-delay time as the lag between the P-wave onset and the maximum of the envelope (for the mathematical definition refer to *De Siena et al.* [2016]) in the case of Mount St. Helens. This method has been applied in this work. Seismograms were band-pass filtered using a 4^{th}-order Butterworth filter

[2]The beginning of the cut window depends on the average travel-time of the dataset. If local earthquakes are selected, 10 seconds before the P-wave arrival time is sufficient to include in the window the origin time.

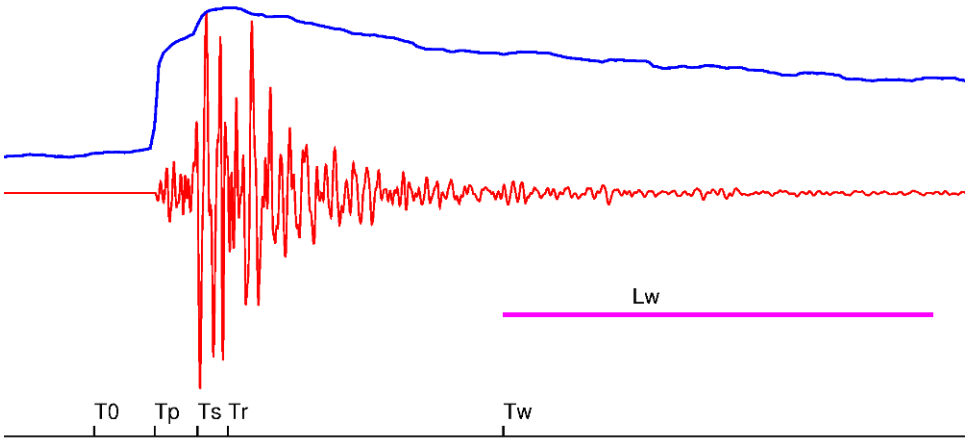

Figure 4.1: Example of a waveform (red solid line) and its envelope (blue solid line). I named T_p and T_s the P- and S- arrivals, t_r is the time at which the waveform reaches the maximum value, T_W is the beginning of the coda window (violet segment) and L_W is its length. All these times are referenced to the origin time T_0.

in 5 frequency bands[3](1 - 2 Hz, 2 - 4 Hz, 4 - 8 Hz, 8 - 16 Hz, 12 - 24 Hz) in forward and backward direction to avoid phase shifting. The envelopes have been computed through the absolute values of the Hilbert transform of the signal. Then, a moving window of length 8 times the inverse central frequency has been used for smoothing (bottom signal in Figure 4.1). Lastly, the time lag between the P-wave onset and the maximum amplitude has been measured, obtaining a peak-delay value for each source-receiver ray.

4.2.1 Peak-delay variation mapping

Peak-delay increases with increasing hypocentral distance (R, in km). Specifically, the theoretical base-10 logarithm of the peak-delay time ($t_r^T(f)$, in seconds, y-axis) is a function of the base-10 logarithm of the hypocentral distance through the following power law [*Saito et al.*, 2002]:

$$log_{10}(t_r^T(f)) = A_r(f) + B_r(f) log_{10}(R) \tag{4.1}$$

where A_r and B_r are the coefficients of the best linear fit for a fixed frequency band (thin black line in Figure 4.2). This linear fit is one of the simplest examples of a *linear inverse problem* in which the data vector of N measurements of logarithmic peak-delay time for each source-receiver ray is $\mathbf{d} = [log_{10}(t_r^T)_1, ..., log_{10}(t_r^T)_N]^T$. It is related to the model

[3]In the following figures I will refer to this frequency bands writing their central frequency instead of all the whole interval: 1.5 Hz, 3 Hz, 6 Hz, 12 Hz, 18 Hz.

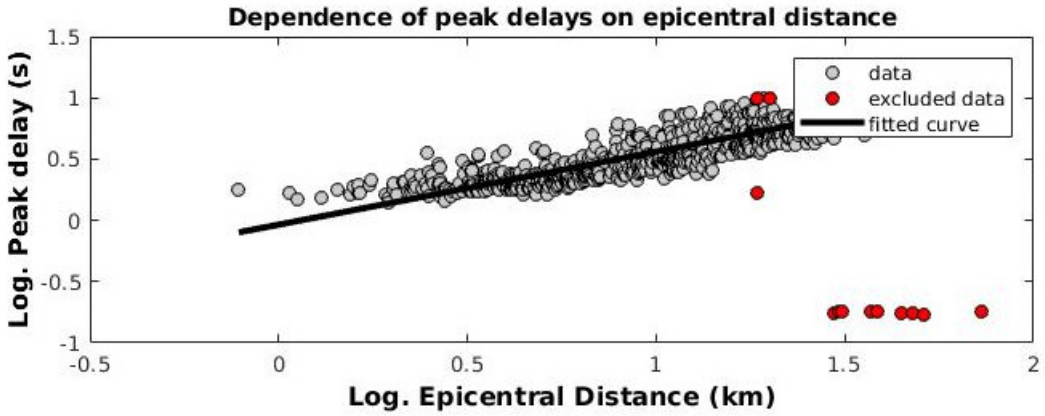

Figure 4.2: Log-log plot of the peak delay (in seconds) as function of the epicentral distance. The solid line represents the best fit of grey data.

parameters vector $\mathbf{m} = [A_r, B_r]$ by N relationships of the form of equation 4.1, which can be arranged as the matrix equation $\mathbf{d} = \mathbf{Gm}$ as follows:

$$\begin{bmatrix} log_{10}(t_r^T)_1 \\ log_{10}(t_r^T)_2 \\ \vdots \\ log_{10}(t_r^T)_N \end{bmatrix} = \begin{bmatrix} 1 & log_{10}R_1 \\ 1 & log_{10}R_2 \\ \vdots & \vdots \\ 1 & log_{10}R_N \end{bmatrix} \begin{bmatrix} A_r \\ B_r \end{bmatrix}$$

The following step is to compute the variation of the peak-delay time with respect to this theoretical trend, using the equation:

$$\Delta log_{10}(t_r(f)) = log_{10}(t_r(f)) - log_{10}(t_r^T(f)). \tag{4.2}$$

These variations represent the relative strength of accumulated P-wave scattering along each ray path [*De Siena et al.*, 2016] and, more specifically:

- **positive variations** of the peak-delay time indicate relative high scattering zones compared to the trend;
- **negative variations** of the peak-delay time indicate relative low-scattering zones compared to the trend.

Figure 4.2 shows an example of the log-log relative peak-delay plot and fit, computed at a fixed frequency band. The retained data are shown as grey circles, while the outliers are shown using red circles. The latter have been excluded because *1) the norm of the residuals between the data and the fit exceeds 2 times their standard deviation* and/or *2)*

the lag time does not range between a minimum and a maximum value, manually fixed according to the dataset.

In order to produce a map of the variations of scattering, the selected area[4] has to be divided into a fixed number of blocks, whose size changes mainly according to the distribution of the dataset. Then, using Equation 4.2, the mean values of $\Delta log_{10}(t_r(f))$ are computed for each source-receiver ray. Using a *regionalization approach*, that is a basic average of all the $\Delta log_{10}(t_r(f))$ crossing a block (requiring at least 5 rays crossing the block), the relative peak-delay map is obtained at different frequency bands. Low scattering is shown using red colour, high scattering is represented by yellow colour. The stability of the maps cannot be tested using a forward model, but two valuable tests can be performed: the node spacing variation of the grid in order to assess if the main patterns are reproduced; the *bootstrap*, which consists of performing several time the same analysis removing each time a random number of samples from the dataset.

4.3 Coda Q measurement methodology

The second mechanism investigated in this section is the *intrinsic attenuation*, or *absorption*. This is defined as the irreversible energy loss through heat while the wave propagates in a medium. The energy envelope of seismic coda waves decay was quantified by *Aki and Chouet* [1975] through the equation:

$$E(t,f) = S(f)t^{-\alpha}\exp\left(\frac{-2\pi f t}{Q_C}\right) \tag{4.3}$$

in which $E(t,f)$ is the power spectral density, $S(f)$ is a source/site term, t is the lapse time starting from the origin time of the event, α is a positive coefficient fixed at 1.5 in a *multiple scattering* interpretation [*Calvet and Margerin*, 2013], and $Q_c^{-1}(f)$ is the frequency-dependent inverse coda quality factor. *Hennino et al.* [2001] pointed out that the equipartition of energy puts forward the role of multiple scattering in the generation of coda waves. *Souriau et al.* [2011] demonstrated that this equipartition regime can be obtained a few seconds after the S-wave onset. Within the multiple scattering interpretation, the physical meaning of Q_c^{-1} is different from the single-scattering interpretation. Indeed, while for the single-scattering regime $Q_c^{-1} = Q_{sc}^{-1} + Q_i^{-1}$ (where Q_{sc} and Q_i are respectively the scattering and absorption quality factors), for the multiple-scattering regime $Q_c \approx Q_i$. The choice of $\alpha = 1.5$ implies a multiple scattering regime, so the Q_c^{-1} in Equation 4.3 could be interpreted as the absorption inverse coda

[4]The area could be of local or regional scale.

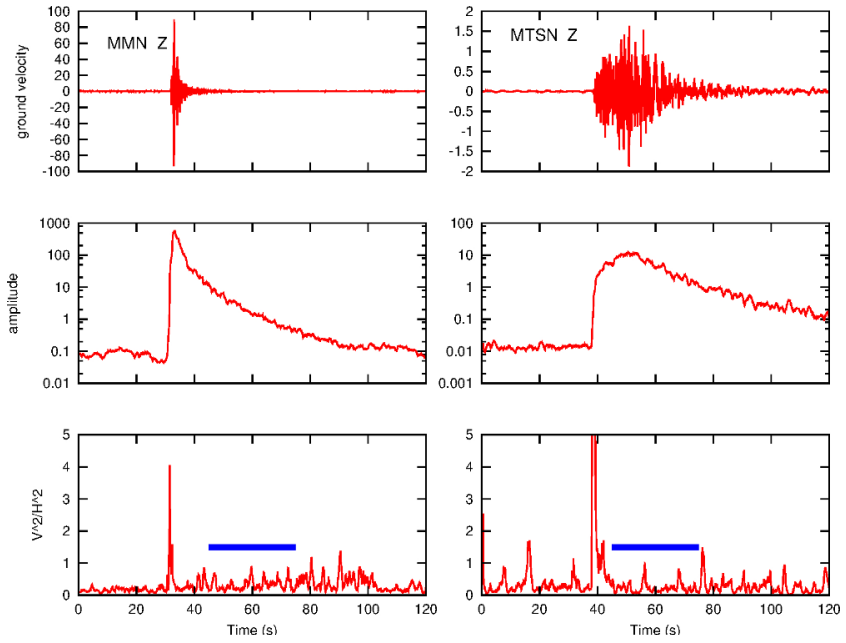

Figure 4.3: From top to bottom: example of waveform used in this work, its smoothed envelope in the middle and the equipartition regime in the bottom panel.

quality factor Q_i^{-1} in the attenuation problem. Similarly to the peak-delay methodology, seismograms were band-pass filtered with a 4^{th}-order Butterworth filter at different frequency bands in the forward and backward direction to avoid phase shifting. The envelopes obtained computing the absolute values of the Hilbert transform (central panels in Figure 4.1) of the signal were smoothed using a moving window of length 8 times the inverse central frequency (bottom signal in Figure 4.1). Selected the coda window, several techniques may be applied to calculate Q_c^{-1}. Here are briefly described only two of these: a *linear* approach, not applied but discussed for completeness, and a *non linear* approach.

Linear approach Still widely used but not applied in this thesis, it consists of the linearization of the Equation 4.3 using the following simple steps:

1. Rearrange Equation 4.3 and, including $S(f)$ in $E(t,f)$, obtaining

$$E(t,f)t^{\alpha} = e^{\left(\frac{-2\pi f t}{Q_C}\right)}$$

2. Apply the logarithm to both sides of the Equation

$$log_{10}\left(E(t,f)t^{\alpha}\right) = \frac{-2\pi f t}{Q_C}$$

3. Bring $2\pi f$ on the left side of the Equation

$$\frac{log_{10}\left(E(t,f)t^{\alpha}\right)}{2\pi f} = \frac{-t}{Q_C}$$

The result is a straight line in which $\frac{log_{10}\left(E(t,f)t^{\alpha}\right)}{2\pi f}$ is the y-axis variable, t is the x-axis variable and $-1/Q_c$ is the gradient. One Q_c^{-1} value is obtained for each source-receiver ray.

Non-linear approach The second approach to assign a Q_c^{-1} value to each source-receiver ray is the non-linear approach. The starting point of this approach is again Equation 4.3. The difference is that in this case a *grid search algorithm* is applied. This algorithm consists of searching in a list of Q_c^{-1} values for the one that minimizes the difference between the observed (the energy obtained directly from the waveform at fixed frequency and lapse time) and predicted values (the energy achieved through equation 4.3). This non-linear solution is more stable than the standard linearized technique for coda signals [*Ibáñez et al.*, 1993]. More details will be given in Subsection 4.4.1.2, for the specific Pollino case of study.

4.3.1 Inverse Q_c mapping

The final aim of this section is the 2D map of Q_c^{-1} of the selected area. One mapping strategy consists in the regionalization approach, as in the case of the peak-delay mapping. The use of an inversion for the spatial distribution of Q_c^{-1} instead of regionalization has been preferred [*Sketsiou et al.*, 2020]. Firstly, the area is divided in blocks. The data vector contains the Q_c^{-1} associate to each waveform. After the inversion a Q_c^{-1} value for each block (model parameters vector) is obtained. Data and model parameters are connected through the matrix whose elements are the *sensitivity kernels* developed by *Del Pezzo et al.* [2016]. These kernels, for each source-receiver pair of coordinates (x_s, y_s) and (x_r, y_r), are defined as follows:

$$\begin{aligned} f[x,y,x_r,y_r,x_s,y_s] = &\frac{1}{4\pi\delta_x D^2\delta_y} exp\left[-\frac{(x-\frac{x_r+x_s}{2})^2}{2(\delta_x D)^2} + \frac{(y-\frac{y_r+y_s}{2})^2}{0.5(\delta_y D)^2}\right] + \\ &+ \frac{1}{2\pi\delta_x D^2\delta_y} exp\left[-\frac{(x-x_s)^2}{2(\delta_x D)^2} + \frac{(y-y_s)^2}{2(\delta_y D)^2}\right] + \\ &+ \frac{1}{2\pi\delta_x D^2\delta_y} exp\left[-\frac{(x-x_r)^2}{2(\delta_x D)^2} + \frac{(y-y_r)^2}{2(\delta_y D)^2}\right] \end{aligned} \tag{4.4}$$

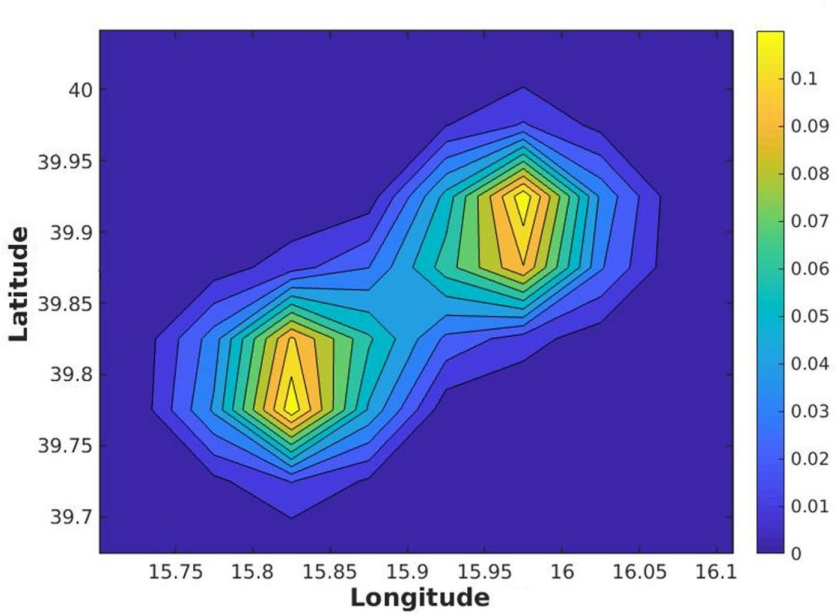

Figure 4.4: Sensitivity kernels for a random source-receiver couple.

where δx and δy are the spatial apertures of the weighting functions along the x- and the y-axis, respectively. These apertures can be set to 0.2 for a wide range of crustal scattering parameters in a diffusive regime. As it is shown in figure 4.4 the kernels give more sensitivity near the sources and receivers, widening also the sensitivity around the ray path between them. Mapping Q_c^{-1} in each block means solving the inverse problem **d=Gm** in which the data vector of N measurements of Q_c^{-1} (for each source-receiver ray) is $\mathbf{d} = [Q_{c_1}, \ldots, Q_{c_N}]$, $\mathbf{m} = [Q_c^1, \ldots, Q_c^M]$ is the model parameters vector $M \times 1$ where M is the number of nodes, through the $N \times M$ matrix **G** composed by the kernels for each source receiver couple k_{ij} with $i = 1, \ldots, N$ and $j = 1, \ldots, M$, arranged as follows:

$$\begin{bmatrix} Q_{c_1} \\ Q_{c_2} \\ \vdots \\ Q_{c_N} \end{bmatrix} = \begin{bmatrix} k_{11} & k_{12} & \ldots & k_{1M} \\ k_{21} & k_{22} & \ldots & k_{2M} \\ \vdots & \vdots & \ddots & \ldots \\ k_{N1} & k_{N2} & \ldots & k_{NM} \end{bmatrix} \begin{bmatrix} Q_c^1 \\ Q_c^2 \\ \vdots \\ Q_c^M \end{bmatrix}$$

The inverse problem is solved using a zero-order *Tikhonov regularization*. This approach is often used in solving inverse problems that are ill-posed[5]. Part of this process is the application of the *Singular Value Decomposition* (SVD) to decompose the **G** matrix into

[5]Ill-posed inversion problems are characterized by so unstable solutions that a small change in measurement can lead to an enormous change in the estimated model [*Aster et al.*, 2018]

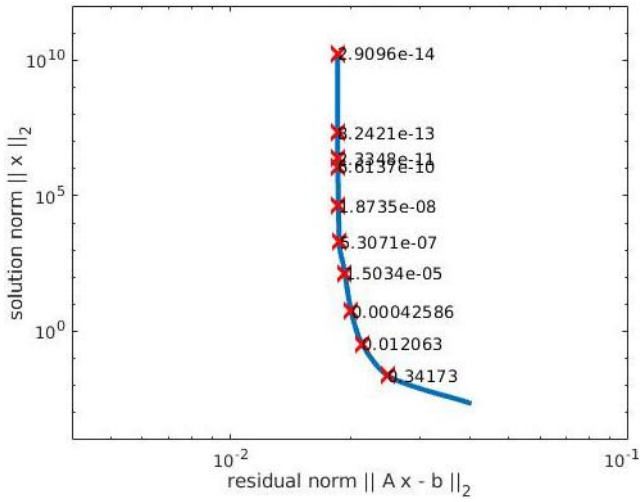

Figure 4.5: Example of the computed L-curve.

$\mathbf{G} = \mathbf{USV}^*$, that in the case of a matrix composed only by real numbers, becomes just $\mathbf{G} = \mathbf{USV}^T$. By definition of SVD, while $\mathbf{S}$ is an $m \times n$ rectangular diagonal matrix whose elements are *non-negative* real numbers [6], $\mathbf{U}$ and $\mathbf{V}$ matrices consist of columns that are the eigenvectors of, respectively, $\mathbf{GG}^*$ and $\mathbf{G}^*\mathbf{G}$, and can therefore easily contain negative values. This can affect the results of the inversion, giving negative values in the model parameters vector, and therefore in the Q_c^{-1} map. This issue cannot be adjusted but can be mitigated, as explained below. The second part of the Tikhonov regularization is the choice of the most suitable *damping parameter* for the inverse problem from the **L-curve**. Computed for different frequency bands, the **L-curve** is a log-log plot of the norm of a regularized solution versus the residual norm, an output produced by the code MuRAT using the MATLAB Regularization Tools (Figure 4.5). Finding the best damping parameter is crucial to ensure that the solution would not be over-smoothed (high damping parameters, moving along the x-axis) or, on the contrary, too rough (low damping parameters, moving along the y-axis). Having obtained a Q_c^{-1} value at each node, the contour plot has been used to map these values with a palette ranging from darker colours (low Q_c^{-1}, low absorption) to brighter ones (high Q_c^{-1}, high absorption). Several checkerboard tests have been performed to evaluate which zone of the plot was well-resolved. In this way all the areas in which the results are not reliable are discoloured.

[6] The square root of the eigenvalues of GG^* and G^*G displayed in descending order

4.4 The Pollino area case of study

The aim of this chapter is to separate and assess the scattering and absorption contribution to the total attenuation of seismic waves and to map their lateral variations in the Pollino area and surroundings (Figure 4.6). The region appears suitable to test the technique, since it has the potential to image the extension of highly-fractured volumes, especially if fluid-filled, inducing seismicity [*De Siena et al.*, 2016, 2017; *Amoroso et al.*, 2017]. The high number of earthquakes of the 2010-2014 seismic swarm (Section 2.3) and surroundings, together with a large number of available seismic stations, provide an appropriate dataset to perform the analysis. In this area of slow-strain [*Cheloni et al.*, 2017], the results may confirm the possible main role of fluids in driving the 2010-2014 sequence, as proposed by *Passarelli et al.* [2015]. In a wider perspective, the separation of scattering and absorption could confirm the connection between attenuation, presence of fluids, and likely fluid-filled connected fractures [*Quintal et al.*, 2014; *Vinci et al.*, 2014], as proposed in rock physics papers.

Finally, the resulting maps have been interpreted in terms of the main geological features and historical and recent seismicity of the area.

4.4.1 Data and methods

The area to be investigated has been chosen [lon = 15.4 - 16.4; lat = 39.6 - 40.4]. Then, 117 local earthquakes have been selected, characterized by source-receiver distances ranging from 1 to 72 km, local magnitude (m_L) between 1.8 to 4.3 and depth between 2 and 56 km. The selection aimed at obtaining an appropriate distribution of sources and receivers to achieve an adequate ray coverage. Since the seismic sequence lasted for years at a variable rate [*Passarelli et al.*, 2015], the number of temporary stations often changed in the area. The selected dataset included recordings from 21 different seismic stations (Figure 4.7). Some of them were permanent, while some others were provisionally installed. These stations were operated by three institutions: 1) *Università della Calabria* (blue diamonds in Figure 4.7); 2) *Istituto Nazionale di Geofisica e Vulcanologia, INGV* (violet diamonds in Figure 4.7); 3) *GFZ*, stations installed for the *temporary Pollino Seismic Experiment*, FDSN network code 4A, to monitor the earthquake sequence between November 2012 and September 2014 (green diamonds in Figure 4.7). The data of INGV and GFZ stations were downloaded from the EIDA online database (*http://eida.gfz-potsdam.de/webdc3/*). Since the seismic events were collected from different databases, they were located by performing the code *EqLoc* for absolute

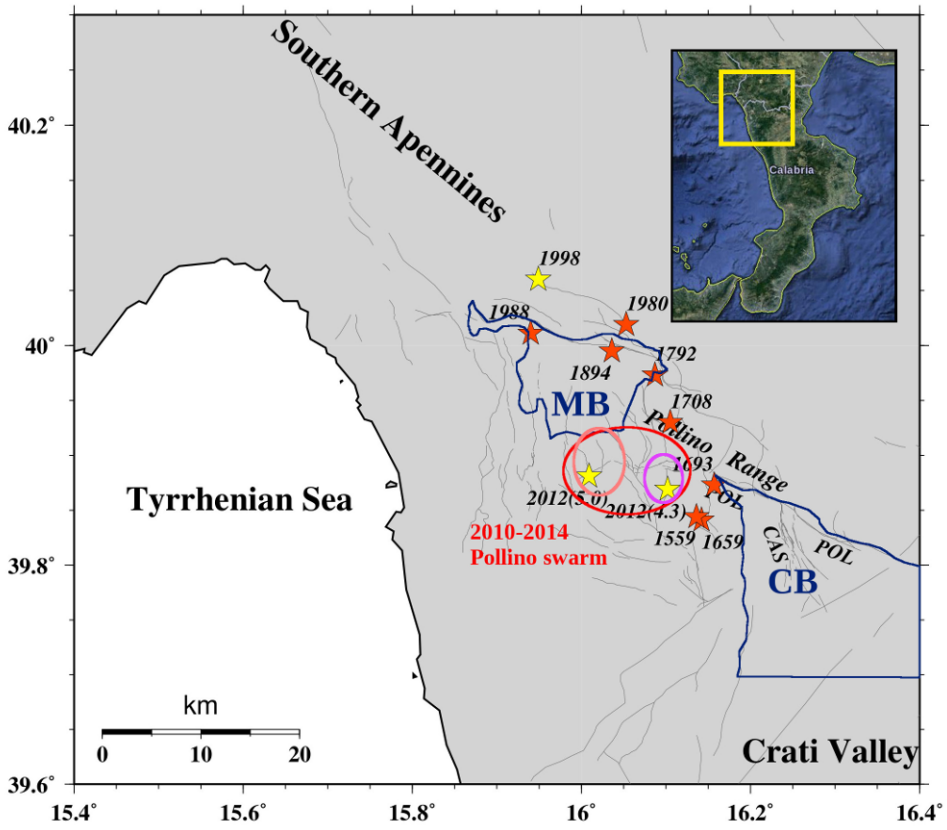

Figure 4.6: Map of the Pollino transition zone, located between the southern Apennines and the Crati Valley (yellow rectangle in the top right panel). Orange stars represent the presumed epicenters of historical earthquakes until 1988, yellow stars represent main shocks occurred in the area in the last 20 years. MB and CB are the Mercure Basin and the Castrovillari Basin, respectively. CAS and POL show the Castrovillari and Pollino Faults. The red ellipse surrounds the area of the 2010-2014 seismic sequence, which occurred in two slightly separated areas (smaller ellipses). Thin black lines are the detailed faults from *Brozzetti et al.* [2017] in the Pollino area and from ITHACA catalogue for the outermost faults surrounding the Pollino area.

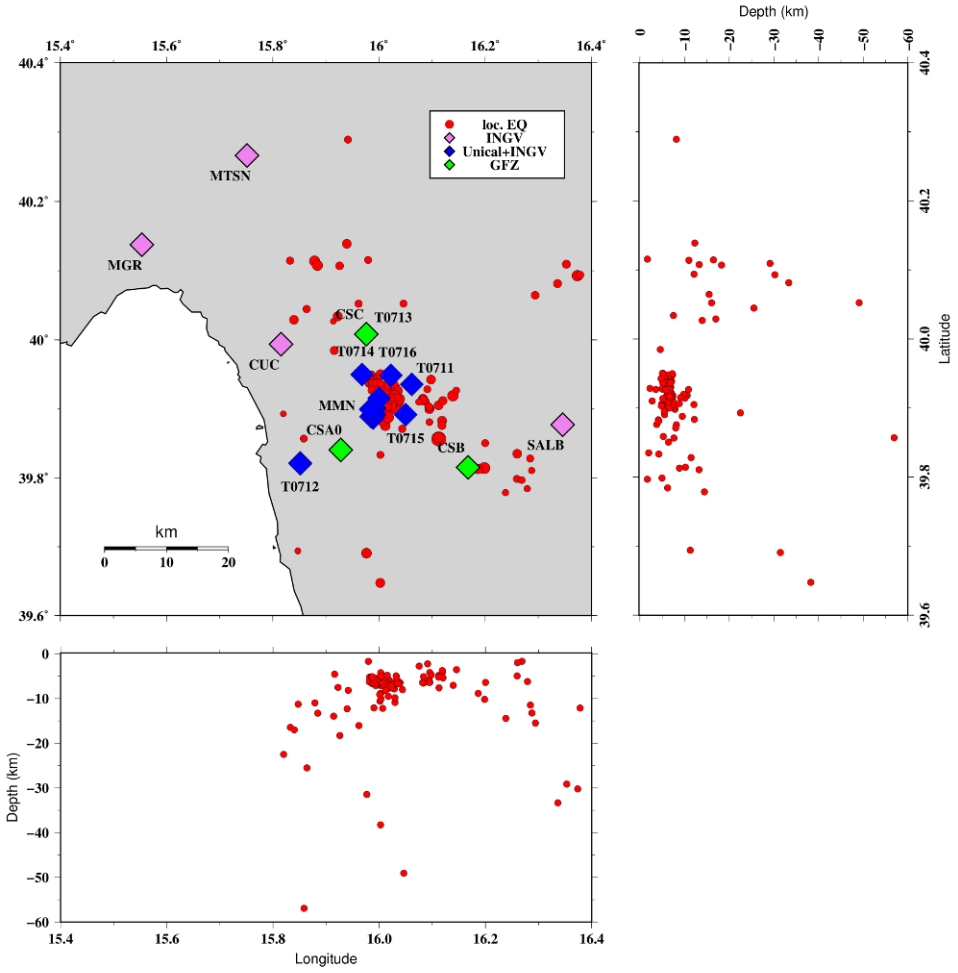

Figure 4.7: Source and receiver distributions in the target area. Red circles represent the epicenters of the events used for this analysis. The three seismic network operating in the area are shown using different colors, specified in the legend.

locations, using the 1D velocity model by *Barberi et al.* [2004]. This step is crucial to achieve a homogeneous dataset, characterized by lower uncertainties, and re-located by the same operator, using the same velocity model for the whole dataset. All the event information were stored in the header of the *.sac* file, as shown in section 4.1.

After these steps, 911 waveforms were collected, characterized by clear P-wave onset and coda-to-noise ratio higher than 3 at 30 s from the origin time, in the frequency range 1 Hz - 32 Hz. Moreover, due to the high quality of the data, also the S-wave arrivals were picked, whenever possible. The final dataset comprises 357 waveforms with a clear picking of both P- and S-waves (Figure 4.1, in section 4.2).

The seismograms were band-pass filtered in 5 frequency bands (1 - 2 Hz, 2 - 4 Hz, 4 - 8

Hz, 8 - 16 Hz, 16 - 32 Hz) applying a Butterworth filter of order 4, forward and backwards. The envelopes were computed from the absolute value of the Hilbert transform of the signal. Then, they were smoothed with a moving window of length 8 times the inverse central frequency (lower panel, Figure 4.1, in section 4.1).

4.4.1.1 Peak-delay time measurement and mapping

For each source-receiver pair, the lag between the P-wave onset and the maximum of the envelope has been computed. The use of P-wave instead of S-wave onset, as discussed and applied in *De Siena et al.* [2016], is motivated by the low number of S-wave pickings, not sufficient to cover such wide area. The difference between the peak-delay value of a source-receiver pair and the average has been obtained (Equation 4.2) for each node of the grid by applying a regionalization approach [*Takahashi et al.*, 2007] in 5 frequency bands (1 - 2 Hz, 2 - 4 Hz, 4 - 8 Hz, 8 - 16 Hz, 16 - 32 Hz).

Figure 4.8 shows from top to bottom the peak-delay maps obtained with increasing frequency, using two different node spacing. Panels of the left column show the peak-delay maps obtained dividing the study area into 320 (20×16) rectangular blocks of size $0.05° \times 0.05°$. Panels of the right column show the same maps obtained using 80 (10×8) rectangular blocks of size $0.1° \times 0.1°$. The color scale ranges from yellow (high scattering) to red (low scattering). The blue triangles represent all the seismic stations used in this work, while the thin black lines are the fault by *Brozzetti et al.* [2017].

4.4.1.2 Inverse coda Q measurement and mapping

The first step to obtain absorption maps is to apply a non-linear approach based on the *grid search* algorithm. It searches in a list of 1000 Q_c^{-1} values for the one that minimizes the difference between the observed and predicted values of the coda energy in Equation 4.3. This analysis gave stable results for the first 4 frequency bands (1 - 2 Hz, 2 - 4 Hz, 4 - 8 Hz, 8 - 16 Hz). On the contrary the results are unstable at the highest frequency band ($c_f = 18Hz$).

After the computation of the seismogram envelopes (Section 4.2), the selection of the coda window is crucial to obtain reliable results. Taking into account Figure 4.1 in Section 4.2, to compute Q_c^{-1} two parameters were chosen: the starting time of the coda window, also called *lapse time*, $t_W = 15s$ from the origin time; the coda window length, $L_W = 10s$ from the origin time. By using the code *MuRAT*, the Q_c^{-1} is obtained dividing the 10s-coda window into five smaller sub-windows of length $2s$ for each source-receiver

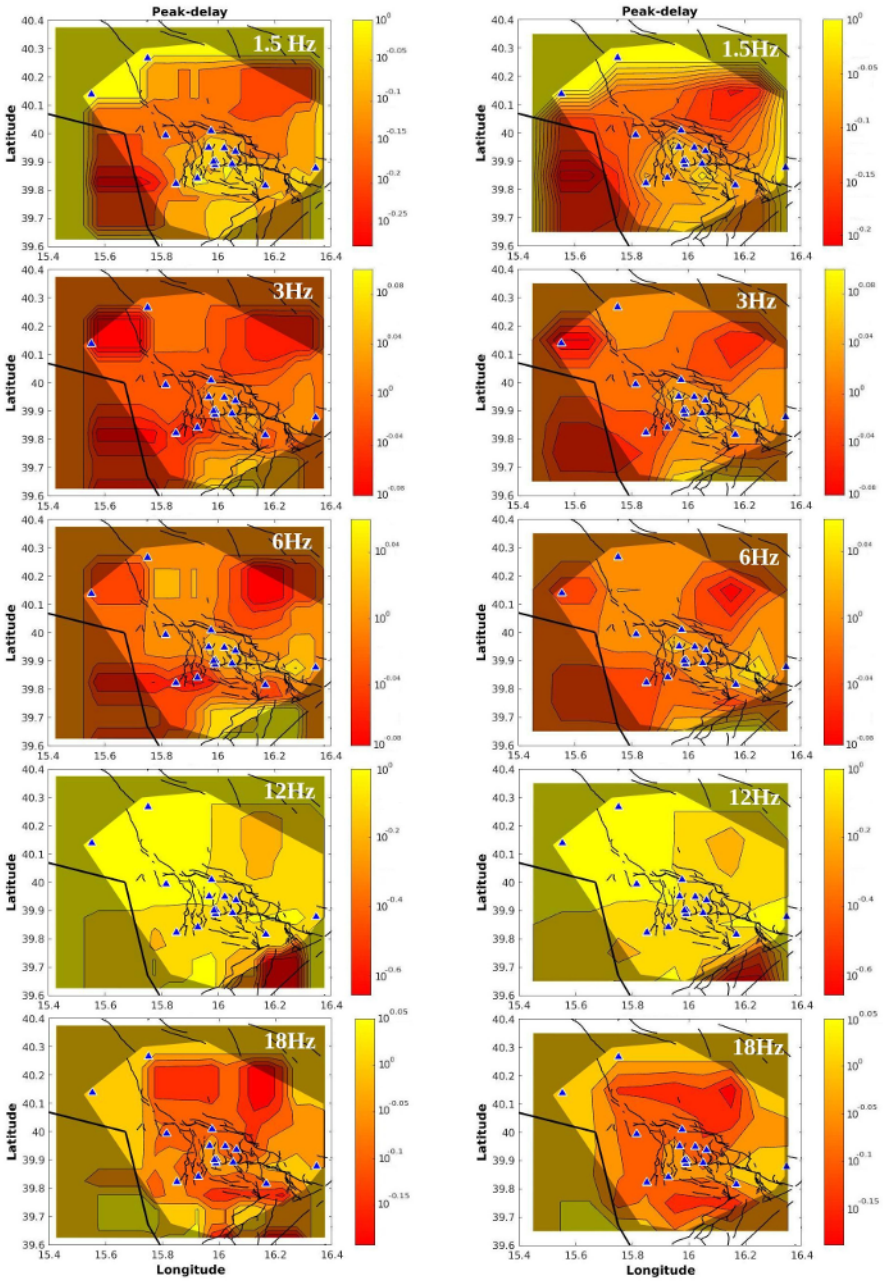

Figure 4.8: Peak-delay map in 5 frequency bands achieved using blocks $0.05° \times 0.05°$ wide (on the left) and a $0.1° \times 0.1°$ wide (on the right). Palettes are the same, ranging from yellow (higher scattering) to red (lower scattering).The blue triangles represent all the seismic stations used in this work, while the thin black lines are the fault by *Brozzetti et al.* [2017].

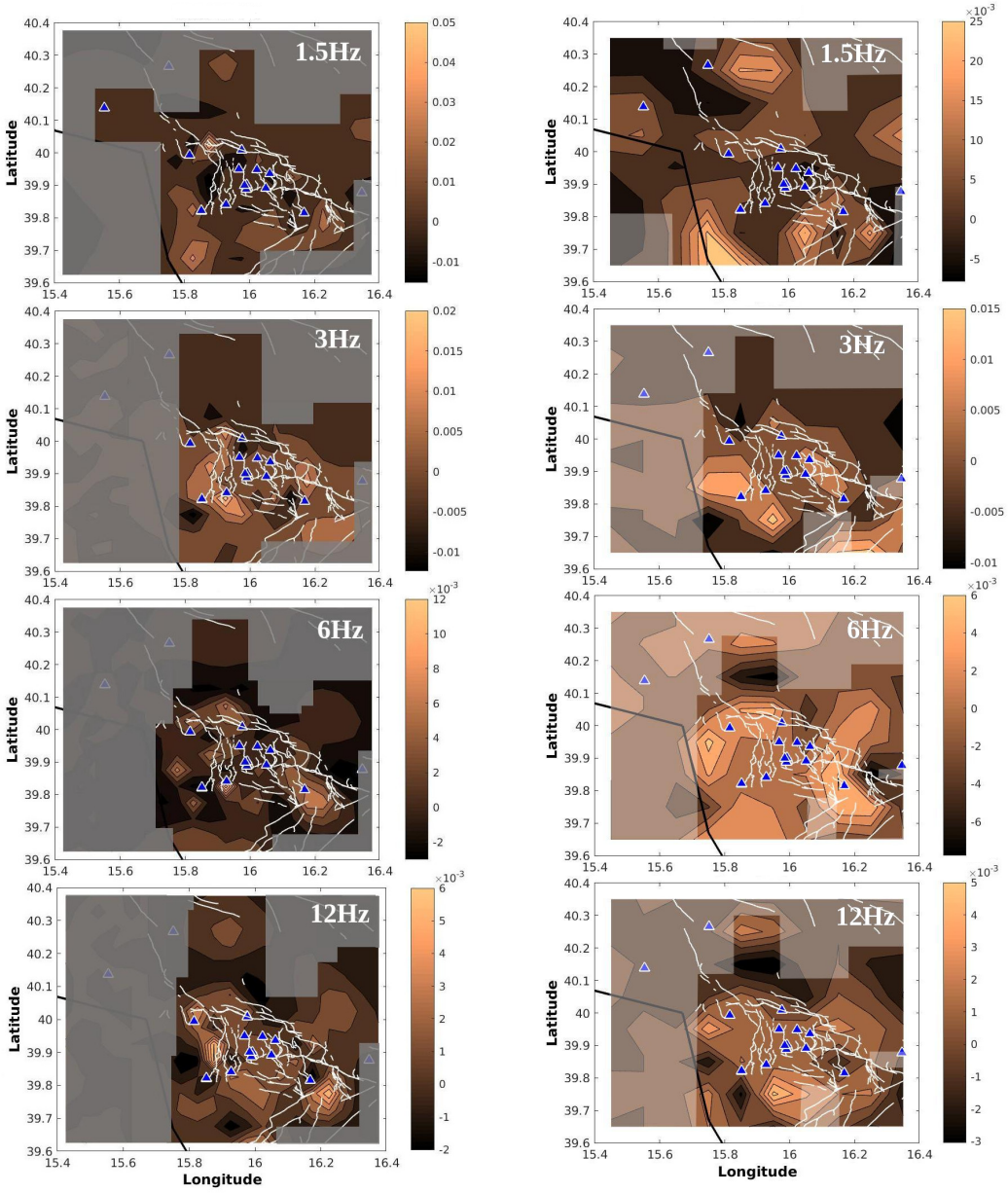

Figure 4.9: Q_c^{-1} map in 4 frequency bands achieved using blocks $0.05° \times 0.05°$ wide (on the left) and a $0.1° \times 0.1°$ wide (on the right). Palettes are the same, ranging from bright colours (higher absorption) to darker colours (lower absorption).

pair. The signal energy in each sub-window was computed. The energy of the last sub-window has been used to normalize these energies, in order to remove the source effect, $S(f)$. Then, the grid-search algorithm has been applied. The Q_c^{-1} that minimizes the difference between the observed and the predicted values of coda energy within the

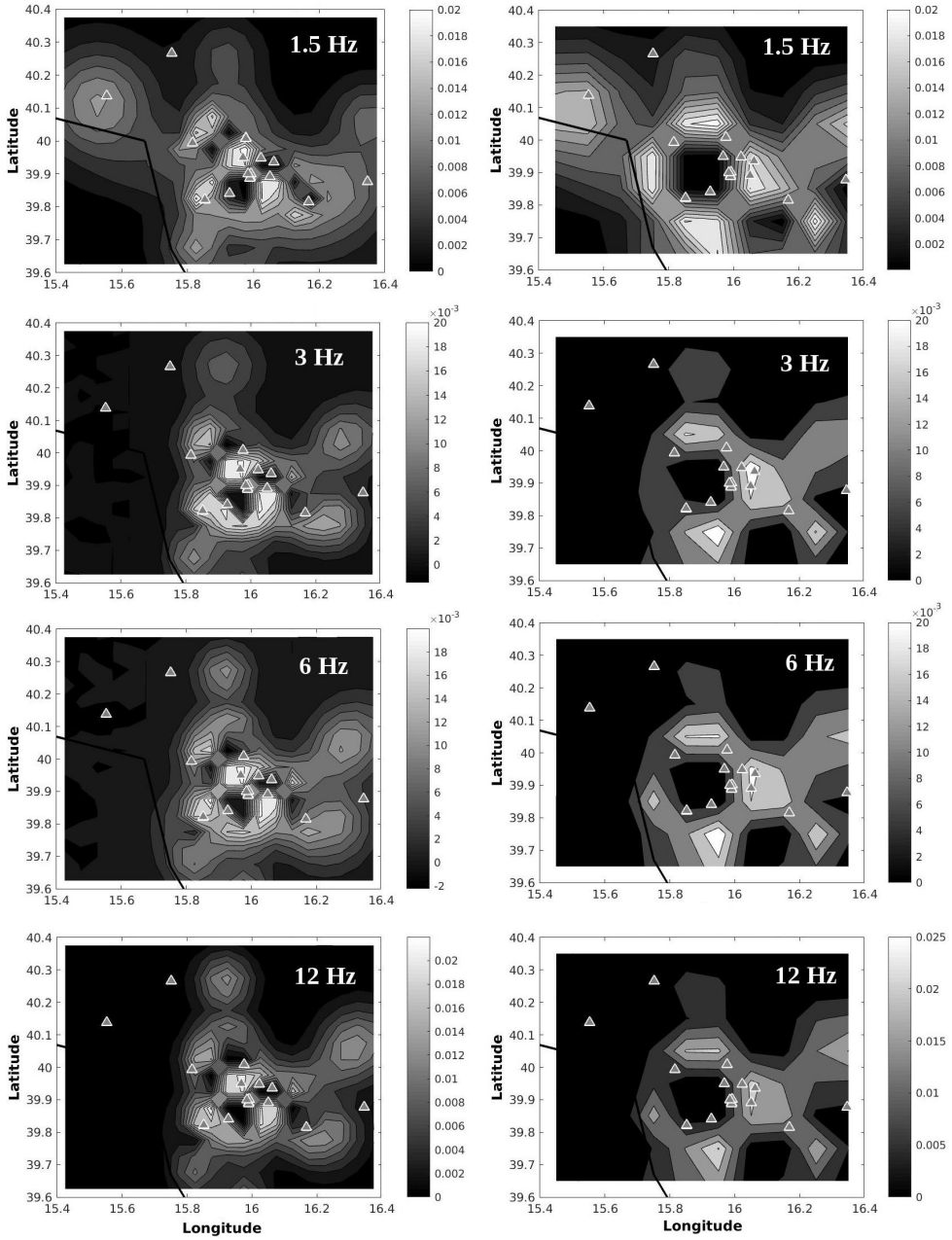

Figure 4.10: Checkerboard test used to hide the unreliable zones of the Q_c^{-1} map in figure 4.9. The left panel show the checkerboard test for the $0.05° \times 0.05°$ grid, while the right panel for the $0.1° \times 0.1°$ grid.

10s-window have been obtained for a specific source-receiver pair. The inversion for the spatial distribution of Q_c^{-1} through the kernels developed by *Del Pezzo et al.* [2016] have been finally performed (as explained in Section 4.3), obtaining a single Q_c^{-1} value for each node of the grid, representing the absorption quality factor.

Figure 4.9 shows the absorption map, for increasing frequencies from top to bottom. The color scale ranges from brighter colors (high Q_c^{-1}, high absorption) to darker colors (low Q_c^{-1}, low absorption). In this map the areas not resolved by the checkerboard test have been obscured (Figure 4.10). The size of the map and node spacing is exactly the same applied computing the peak-delay measurements. Left panels show the results with respect to 320 (20×16) rectangular blocks of size $0.05° \times 0.05°$. Right panels show the map obtained using 80 (10×8) rectangular blocks of size $0.1° \times 0.1°$.

4.4.1.3 Parameter space variation and mapping

Combining scattering and absorption maps is necessary for a more straightforward interpretation of the results. This is possible using the parameter space variation (left panel in figure 4.11). The parameter space has been divided into four quadrants. The average value from the relative peak-delay $\Delta log_{10}(t_r(f))$ and from Q_c^{-1} have been removed in order to obtain their variations on x- and y-axis, respectively [*De Siena et al.*, 2016]. Each point is characterized by a relative peak-delay and Q_c^{-1} with regards to their average values. These points have been plotted in the *parameter separation map* (central panels in Figure 4.11). Different color have been set for each possible combination of the parameter space: red for high scattering and high absorption (HS-HA), orange for low scattering and high absorption (LS-HA), light blue for high scattering and low absorption (HS-LA), green for low scattering and low absorption (LS-LA). Gray color shows values with a level of discrimination between two quadrants less than 1% of the maximum variations. The analysis has ben carried out at different frequencies, because bigger structures scatter at lower frequencies, while smaller structures scatter at higher frequencies. High scattering and high absorption red patterns have been interpreted in terms of fluid-filled connected fractures. Low scattering and low absorption red patterns represent compact and dry medium. The cyan pattern characterized by high scattering and low absorption is instead the representation of a highly fractured medium not permeated by fluids, and finally the orange patterns mark areas not characterized by heterogeneities but showing presence of fluids. This palette has been used to characterize the block of the grid associated to the colored point of the parameter space.

This visual method is useful because it sheds light on the main geological patterns,

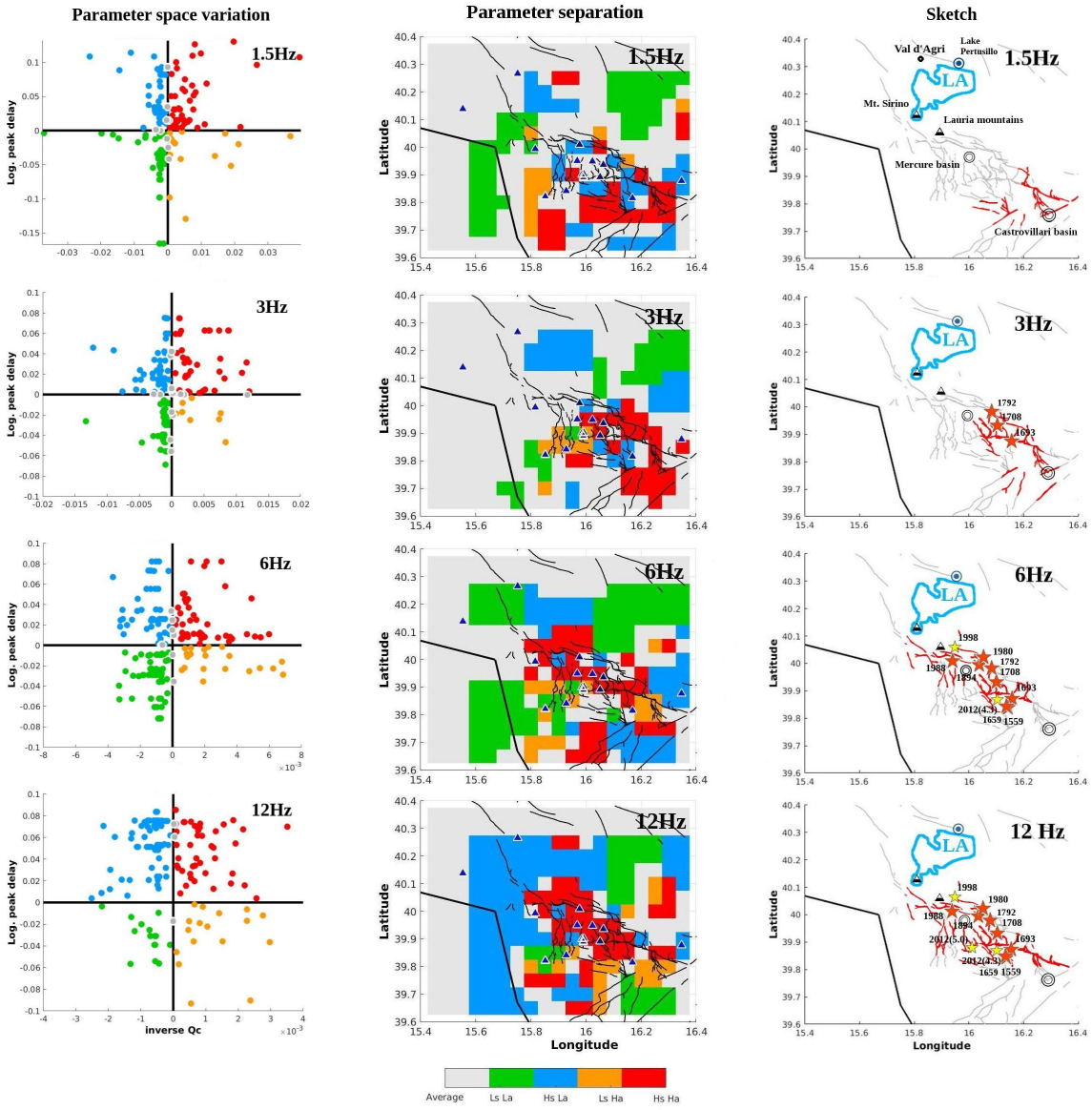

Figure 4.11: Parameter space separation (on the left), parameter space plot (center) and sketch of the main pattern achieved from the analysis in 4 frequency bands. Color palette: red for high scattering and high absorption (HS-HA), orange for low scattering and high absorption (LS-HA), light blue for high scattering and low absorption (HS-LA), green for low scattering and low absorption (LS-LA). The cyan pattern corresponding to the Lucanian Apennines (shortly named *LA*) extends from the Mount Sirino (SW) to the Lake Pertusillo (NE). Faults are coloured and stars (orange for earthquakes before 1998, yellow for more recent earthquakes) are displayed each time they are located in a red high scattering/high absorption block.

whether they are stable or migrating on the map at different frequencies. This may be clearer in the sketch on the right hand side of Figure 4.11. Due to the fact that HS-HA patterns represent highly fractured and fluid-filled structures, any time a portion of a fault [*Brozzetti et al.*, 2017] passed through the HS-HA blocks, it is marked using red colour. Moreover, if one or more historical or more recent earthquakes occurred on this patch of the faults, it is displayed on the map.

4.4.2 Results and discussion

In Figure 4.11 the results have been shown (central panel) and interpreted (right panel) in terms of relative scattering and absorption for each frequency band. The main assumption is that heterogeneities and fluid content are located mostly in the upper crust due to the depths of the hypocenters used in this work. Therefore the aim is to find any relationships between the main scattering/absorption patterns and the geological features of the investigated area.

No orange zones (LS-HA) are stable and big enough to be discussed on the map. The Calabro-Lucania coastal range (western side of the maps - Figure 4.11, central panel) changes from LS-LA at low frequency (green, 1.5 Hz and 6 Hz) to HS-LA (cyan) at 12 Hz. One of the patterns most stable in frequency, the green LS-LA zone, appears in the north-eastern sector of the maps. However, in both cases the resolution tests show that the areas are unresolved and no reliable connection with geological features on the map can be established.

The most stable pattern in frequency is the light blue HS-LA pattern. It comprises some of the highest mountains of the southern Apennines and it is a well-resolved area. This zone is located at the southern part of the Lucanian Apennines (named LA in Figure 4.11, right panel), extending from Mount Sirino to Lake Pertusillo [*Schiattarella*, 1998]. Geologically, this is a compact stand-alone carbonate block, surrounded by faults and isolated through clay formations. Fractured volumes of minor importance are present in this block due to the high-compression regime in the region. The geological configuration explains the stable high scattering values at all frequencies. The low-absorption values are likely a consequence of the cohesion of the carbonate block surrounded by clay, which acts as a shield between the extensive northern hydrocarbon deposit in the Val D'Agri zone and the southern Pollino area.

The most remarkable and well-resolved pattern on the map is the red-coloured HS-HA patterns. The faults falling into these patterns at each frequency are highlighted using the red colour in the right panels of Figure 4.11. The Mercure and the Castrovillari basins

(MB and CB, respectively) are both characterized by shallow-marine deposits. The former is filled with alluvial, fluvial-deltaic and lacustrine sediments [*Ferranti et al.*, 2017]; the latter is filled with clay, sand (in the shallower layer), fine marine sediments, and conglomerates [*Schiattarella*, 1998]. Because of their composition, both basins are likely characterized by high absorption, contributing to the red pattern. The HS-HA red pattern marks the 120° fault system underlying the Pollino Range at frequencies of 6 and 12 Hz. A relationship with the prominent geological characteristic of a multiple fragmented shallow-water carbonate succession has been suggested. The same HS-HA (red) at the same frequencies characterize the Lauria Mountains (LM), the north-west extension of the carbonate succession of the Pollino Ridge. The HS-HA pattern is not stable on the map, but migrates with changing frequency. At 1.5 Hz, the red area marks the S-SE sector of the map, inside and around the Castrovillari Basin, crossed by extensive fault networks; at 3 Hz the pattern is still present in the SE sector but becomes predominant in the Pollino Range area. At 6 Hz the red color spreads across the Mercure basins and slightly above Lauria Mountains. Finally, at 12 Hz it fills the area of the 2010-2014 seismic sequence. The relatively high-absorption values correlate well with the high v_P/v_S values found in the same area by *Barberi et al.* [2004] and by *Piana Agostinetti and Amato* [2009]. Furthermore, the results confirm the scenario proposed by *Passarelli et al.* [2015] for the 2010-2014 seismic sequence. In this paper the authors suggest a combination of pore-pressure increase and hydro-fracturing that can cause an expansion of the focal area due to an incremental stress accumulation.

Historical earthquake locations are usually obtained with methods based on the evaluation of the epicenter as the center of mass of largest intensities (e.g. the *Boxer method* used for the Pollino area, *Gasperini et al.* [2010]). These hypocenter locations are affected by significant uncertainties, differently from those events occurred in the last 20 years. A relevant result of this analysis is that the historical seismicity clearly follow a SE-to-NW trend through time, even if the location errors are estimated to be at least 5 km due to the low densely populated Pollino region. This trend stopped after the 1998 Mercure basin earthquake. The red HS-HA pattern moves in the same direction with increasing frequency, following the epicenter trend. Recent earthquakes likely reactivated small fracture networks as they migrate along the main faults, modifying the way fluids permeate fault structures. Poro-elasticity studies proved the central role of fluid pressure diffusion between connected fractures [*Quintal et al.*, 2014; *Vinci et al.*, 2014]. *Hunziker et al.* [2018] pointed out that the still-unknown relationship between seismic attenuation, diffusion of fluid pressure and fracture connectivity can be crucial

to identify a highly-fractured volume and track its hydraulic behavior. The results obtained strongly suggest such a relationship in fault areas demonstrated through physical evidence. In fact, changes of peak-delay and Q_c^{-1} at different frequencies mark heterogeneities of different size [*Saito et al.*, 2002]: in the case of faults, small fractured volumes in active zones can only be imaged by shorter-wavelength (higher-frequency) attenuation parameters. While these fracture networks heal quickly in seismically-active areas, they are continuously being reactivated due to distant seismicity [*Xue et al.*, 2009], at least where fluids are abundant. The healing of smaller fractures is instead permanent in areas not deformed by recent activity. Here, larger unhealed structures should be visible from their long-wavelength (low-frequency) high scattering and high absorption signatures.

Here it is thus inferred that the migration of the HS-HA patterns with increasing frequency shows the effect of fracture healing [*Xue et al.*, 2009]. The anomalies effectively track the earthquake migration since the 16^{th} century (Figure 4.6) by mapping the fracture-network scattering and absorption changes in frequency. While the role of fluids in nucleating historical and recent seismicity is confirmed, the results also support the view that the last Pollino sequence represented a change in the usual seismicity trend of the area. In fact, the sequence seemed to be composed mainly of fore-shocks, which likely occurred on the same fault structures more than once, then followed by two main-shocks, whose after-shocks represent only one quarter of the total amount of the events [*Passarelli et al.*, 2015]. Here it is finally suggested that the SE-to-NW migration of the HS-HA pattern was stopped by the shield represented by the high scattering compressed carbonates of the Lucanian Apennines. Since the Pollino swarm, a permanent network has been installed in the area and it may provide sufficient data to test these inferences in the presence of renewed seismic activity.

4.4.3 Conclusions

Peak-delay and inverse coda quality factor have been measured and mapped using a 2D approximation in four frequency bands to image the scattering and absorption properties of the slowly-deforming Pollino area (Southern Italy). The pattern of anomalies obtained from the analysis shows a correlation with the geological features of the area and with the progressive shift in location of earthquakes. High scattering and high-absorption anomalies (HS-HA) change their position from faults in the south/southeastern Castrovillari basin (1.5 Hz) to the northwestern Mercure Basin and Pollino swarm area (6-12 Hz) across the fault systems (3 Hz). It is inferred that the Lucanian Apennines com-

pressed carbonates, marked by high scattering, constitute a barrier for fracture network connectivity and fluid propagation. The two sedimentary basins are characterized by high absorption. However, high-absorption and high-scattering patterns observed at higher frequency likely reveal fluid-filled fractured volumes of shorter dimension.

At low frequency, the patterns map the structures of the inactive fault systems (1.5 Hz) or fractured by seismic sequences dating back to the 16^{th}-18^{th} century (3 Hz). Here, shorter fractures are progressively healed, with high scattering and absorption marking extended fault areas permanently deformed. At 6 Hz the anomalies characterize the NW branch of the faults, tracking the seismic activity of the last two centuries up to the Mercure basin earthquake (1998). The earthquake migration is likely due to the progressive increase of the contribution of small-scale fluid-filled fractures to scattering and absorption. At the highest frequency (12 Hz) the HS-HA area becomes broader and covers the fault system that generated the last Pollino swarm (2010-2014), SW of the Mercure basin. Here it is inferred that the fracture propagation trend was blocked NW by the high scattering Lucanian Apennine carbonates. The scattering and absorption picture described by this interpretation provides an independent view on the well-known geological features of the area, the known fault network, and the migration of seismogenic zones through the last five centuries, focusing on the important role of fluid saturation. Further observations with better distributed earthquakes and seismic stations may give deeper insights about the physics underlying these processes. More efforts are necessary to successfully apply the laboratory results to the Earth crust, which means in our case to measure or estimate the time scale of processes such as fracture healing and fluid migration throughout connected/not connected fracture networks. Still, this work supports the view that attenuation and scattering parameters are able to reconstruct shape and dynamics of fluid-filled fracture networks in fault areas.

CHAPTER 5

SEISMIC SITE EFFECTS AND POLARIZATION ANALYSIS

The earthquake evolution history comprises mainly three steps: the source process, i.e. the *fault activation* characterized by a certain focal mechanism; the *wave propagation* along the source receiver path in attenuating media; the *seismic site response*. This chapter will focus on the third step of this chain, performing an accurate evaluation of the *site effects*, whose main manifestation are the change in amplitude, frequency content and polarization of the ground motion nearby at any investigated site. This analysis is crucial in order to assess and mitigate the seismic risk of an area [*Pitilakis*, 2004; *Panzera et al.*, 2015].

Geological and morphological features affect the local seismic response, changing waves characteristics even at a distance of few meters. Since the San Francisco earthquake in 1906, the increasing number of seismic network allowed the estimation of this phenomenon [*Singh and Ordaz*, 1993; *Bonilla et al.*, 1997; *Parolai et al.*, 2010; *Clemente-Chavez et al.*, 2014].

The difference in local seismic response has to be searched among several factors:

- presence of soft layers on the underlying bedrock;
- topographic irregularities;
- presence of water, landslides and underground cavities;
- presence of faults.

Soft soil layers represent the consequence of the process of erosion and sedimentation in the foothills of mountain ranges. In the last few years, increasing importance has been given to convex and concave topographic irregularities [*Chávez-García et al.*, 1997; *Rigano et al.*, 2008; *Buech et al.*, 2010; *Pischiutta et al.*, 2010; *Formisano et al.*, 2012], presence of faults [*Pischiutta et al.*, 2012, 2014, 2017; *Panzera et al.*, 2015, 2017] and their relationship with site effects in terms of directional resonance [*Bonamassa and Vidale*, 1991]. Several papers on the argument reveal that the topography modifies the relative amplitude of horizontal motion parallel to the slope of the closer relief. On the contrary fault zones make the polarization orthogonal to the fault strike, due to multiple reflections, resonances and wave trapping. For these reasons, polarization analysis may improve the site effects assessment.

The aim of this chapter is the evaluation of site effects in the Pollino area through the use of: the H/V Spectral Ratio method [*Nakamura*, 1989], applied both on seismic noise (*HVNR*) and earthquakes (*HVSR*), and the polarization analysis.

5.1 Empirical approaches to evaluate site effects: the HVSR method

In the second half of the 20^{th} century, several techniques have been developed to evaluate ground motion amplifications related to local geo-morphological conditions. One of the first techniques applied and still widely used to assess site amplifications is the *Standard Spectral Ratio*, SSR [*Borcherdt*, 1970; *Borcherdt and Gibbs*, 1976]. This approach requires the use of a seismic station installed on bedrock (usually outcropping rock, free of any kind of site effect) used as reference site. The technique consists of estimating the ratio between the Fourier amplitude spectra of the soil-site recorded earthquakes with respect to that computed at the reference site for the same earthquake. Indeed, if the two seismic stations are installed very close to each other the input at the source and the path attenuation parameters have to be necessarily the same. The only feature that can produce a different Fourier amplitude spectra are the soil geo-morphological conditions. The validation of the results depends on the simultaneity of the recordings between stations and reference site and the smaller reference-soil site distance if compared with the epicentral one. The former request can be overcome with the application of the *Generalized Inversion Scheme Technique, GIS* [*Andrews*, 1986]. The main advantage of this approach is the separation of the source, propagation path and local site effects. In

this case the absence of simultaneous earthquake recordings at all the stations of the network is not an issue [*Field and Jacob*, 1995].

Phillips and Aki [1986] proposed another method to assess site effects using the latest part of the seismograms, the *coda-wave ratios* technique. The main advantages of this technique are the separation into source, path and site contribution of the coda spectrum and the lack of saturation that affect S-waves. In suitable conditions (three-component seismometers, small-to-moderate earthquakes recording with large SNR) S-waves can be used to apply the same technique [*Field et al.*, 1992; *Steidl*, 1993; *Margheriti et al.*, 1994; *Hartzell et al.*, 1996; *Su et al.*, 1996]. By comparing the results from direct S-waves and coda waves, many authors have shown that coda waves give more stable estimates of the amplification [*Su et al.*, 1996; *Bonilla et al.*, 1997]. The main limitation that affects all the above-mentioned techniques is the use of a reference site. Effectively, an appropriate reference site is not always available. This has led to the development of several non-reference approaches.

The H/V Spectral Ratio Method The *Horizontal-to-Vertical Spectral Ratio* method, *HVSR* [*Nakamura*, 1989] was developed to overcome the need of a reference site (that can be affected by site effects as well) and of a high seismicity area. This method, proposed by *Nogoshi* [1971], taking the idea by *Kanai and Tanaka* [1961], works also with seismic ambient vibrations recordings. It is based on the principle that *on soft layers only the horizontal components of the ground motion, not the vertical one, seems to be affected by amplification*. Technically, the HVSR is based on the ratio between the horizontal and the vertical velocity Fourier spectra[1]. It is evaluated as follows

$$HVSR = \frac{H_{NS} + H_{EW}}{2V} \tag{5.1}$$

where H_{NS}, H_{EW} and V are the velocity Fourier spectra of the North-South, Est-West and vertical component of the ground motion, respectively. The value $\frac{H_{NS}+H_{EW}}{2}$ is the arithmetic mean of the horizontal components, used in this thesis. Useful guidelines for the implementation of the HVSR technique on ambient vibration have been edited during the *SESAME, Site EffectS assessment using AMbient Excitations* project [*Bard et al.*, 2004].

In spite of the simplicity of the equation, the theoretical background of the technique is still not totally understood. In the last few years some authors [*Mucciarelli and Gallipoli*, 2001; *Lunedei and Malischewsky*, 2015] tried to summarize the theories about the precise

[1] Amplitude or acceleration Fourier spectra are commonly used as well.

physical interpretation of the results given by the HVSR method, on the nature of the seismic noise and on its sources. Most of the proposed models look at the Earth as a one-dimensional homogeneous and isotropic horizontal layers on bedrock. The early theories were body-waves based. They interpret the ambient vibrations as a combination of S- and Rayleigh waves [*Nakamura*, 1989] or separate body-waves from Rayleigh contribution (*QTS, quasi transfer spectrum*, *Nakamura* [2000]). Both of them assert that the peak frequency and amplitude of the H/V spectral ratio represents the resonance frequency and the amplification factor of the S-waves reverberating in a soft soil layer. At the same time, a larger number of papers [*Lachet and Bard*, 1994, 1995; *Konno and Ohmachi*, 1998; *Wathelet et al.*, 2004] discussed the role of the ellipticity of Rayleigh waves and on the energy of surface waves. They concluded that Nakamura's interpretation of resonance frequency and amplification factor had to be referred to surface waves, instead of S-waves. Taking into account also the role of the source, *Lachet and Bard* [1994, 1995] stated that *the overall shape of the H/V spectral ratio is due to multiple sources and, while the H/V peak-frequency is related to the ellipticity peak-frequency of the Rayleigh fundamental mode as well as to the first-peak position of the ratio between horizontal and vertical ground-motion produced by S-waves incident from a range of angles, the peak amplitude does not correspond to the amplification factor*. *Bonnefoy-Claudet et al.* [2008] using numerical simulations confirmed this statement. They concluded that the peak-frequency could be explained in terms of S-wave resonance, Rayleigh ellipticity, Love Airy phase or a mix of them, depending on the stratigraphy. Nowadays H/V spectral ratio technique is regularly applied worldwide, from microzonation [*Kobayashi et al.*, 1991; *Lachet et al.*, 1996; *Strollo et al.*, 2007], to resonance frequency detection related to depth in sedimentary basins [*Ohmachi et al.*, 1991; *Duval et al.*, 1994; *Gosar et al.*, 2001]. It is also applied to assess the thickness of a basin (H) from the measured frequency peak (f_0) using the well-known equation $f_0 = \frac{V_S}{4H}$, where v_S is the S-wave velocity through the soil [*Bodin and Horton*, 1999; *Delgado et al.*, 2000; *Giampiccolo et al.*, 2001]. It is useful to discover landslide detachment surface [*Gallipoli*, 2000; *Imposa et al.*, 2017], or underground cavities [*Sgarlato et al.*, 2011]. In the last few years, it has also been applied to achieve the fundamental frequencies of buildings in order to investigate possible couplings between civil constructions and soil frequencies [*Ganev et al.*, 1995; *Mucciarelli and Monachesi*, 1998, 1999].

5.2 The polarization analysis

The *polarization analysis* have been applied in this work with the aim for a better knowledge of the main source of the local site effects. In fact, site effects can modify the seismic waves polarization, mainly in absence of flat stratigraphy, which is where topographic irregularities or fault damage zones prevail.

Fault damage zones are everything but simple geological structures. The combination of several phenomena such as resonance, reflection, and wave trapping may lead to an amplification of horizontal motion components. The resulting wave polarization appears nearly perpendicular to the fault strike [*Pischiutta et al.*, 2012, 2014, 2017; *Panzera et al.*, 2015, 2017]. Similar direction of the wave polarization may be caused by *topographic effects*. They usually occur as a horizontal polarization nearly perpendicular to the ridge elongation [*Chávez-García et al.*, 1997; *Buech et al.*, 2010; *Pischiutta et al.*, 2010; *Formisano et al.*, 2012]. Considering all these reasons, the joint observation of *HVSR* and *polarization analysis* may give a more exhaustive interpretation of site effects.

The polarization analysis has been computed using the *covariance matrix method in time domain* [*Montalbetti and Kanasewich*, 1970; *Jurkevics*, 1988]. The covariance m_{ij} (zero-lag cross-correlation) is given by the equation:

$$m_{ij} = \frac{1}{N} \sum_{k=1}^{N} A_i^k A_j^k \tag{5.2}$$

in which A_i^k and A_j^k represent the amplitude of the k^{th} sample (k=1,...,N) of the trace A recorded by the i^{th} and j^{th} channel (i,j=1,...,3; e.g. NS, EW and Z component). In a three-dimensional space the *covariance matrix* is obtained. Its on-diagonal terms are the variances, while the off-diagonal terms represent the covariances between the three possible directions:

$$M_C = \begin{bmatrix} m_{11} & m_{12} & m_{13} \\ m_{21} & m_{22} & m_{23} \\ m_{31} & m_{32} & m_{33} \end{bmatrix}$$

The matrix is symmetric and positive defined, so the eigenvalues, $\lambda_1 \geq \lambda_2 \geq \lambda_3$, are real and non-negative. This matrix is linked to a "covariance ellipsoid", a quadratic function whose shape changes according to eigenvalues combination. The covariance matrix method is applied on seismic ambient vibration due to the fact that noise and scattering distortion tend to be uncorrelated among three components over a window. These eigenvalues represent the average energies of the seismic event emitted in the three direction represented by the three associated eigenvectors u_1, u_2, u_3 that define

a new Cartesian system of coordinates [*Cliet and Dubesset*, 1987]. This means that, for instance, if only one eigenvalue is non-zero, the polarization is linear. Usually all the three eigenvalues have non-zero values. Their values depend on the strength of the polarization. If they are similar there is not a predominant direction of polarization, while the presence of a bigger value compared to the other two means a strong directionality.

Starting from eigenvalues and eigenvectors it is possible to define the *rectilinearity* of the particle motion:

$$RL = 1 - \frac{\lambda_2 + \lambda_3}{2\lambda_1} \tag{5.3}$$

that is equal to unity when there is only one non-zero eigenvalue (body waves). Then, the *polarization azimuth* defines the angle between the North and the projection of the polarization vector, i.e. the direction given by the eigenvector associated to the largest eigenvalue λ_1, on the horizontal plane [*La Rocca et al.*, 2010]:

$$P_{Az} = tan^{-1}\left(\frac{u_{21} sign(u_{11})}{u_{31} sign(u_{11})}\right) \tag{5.4}$$

where u_{j1} ($j = 1,2,3$) are the three direction cosines of eigenvector u_1 and the *sign* function is introduced to resolve the 180° ambiguity by taking the positive vertical component of u_1.

Other characteristics of the ground motion that can be evaluated through the analysis of the covariance matrix are the *degree of planarity* that is given by:

$$P = 1 - \left(\frac{2\lambda_3}{\lambda_1 + \lambda_2}\right) \tag{5.5}$$

and gives the the *apparent incident angle*:

$$P_{inc} = cos^{-1}|u_{11}| \tag{5.6}$$

In this work the azimuth angle will be plotted at different frequency ranges, between 0° and 180° in polar histograms calculated at bins of 10°. This visualization allows to see if the polarization direction is frequency dependent, but it does not account for the horizontal-to-vertical amplification. Therefore the *HVSR* curves were computed as a function of the azimuth using the software *GEOPSY*. In this way, H/V ratios are displayed as function of both frequency and azimuth. This graphical representation reveals the frequency band within which the wave-field is polarized. HVSR and polarization analysis have been performed to the western side of the Pollino area, study region of the thesis.

5.3 The Pollino case of study

The Horizontal-to-Vertical Spectral Ratio has been applied to both noise and local-to-regional earthquake recordings in the western sector of the Pollino area and surroundings (Southern Italy). The analysis has been improved by performing the polarization analysis to detect the sources responsible for the ground amplification.

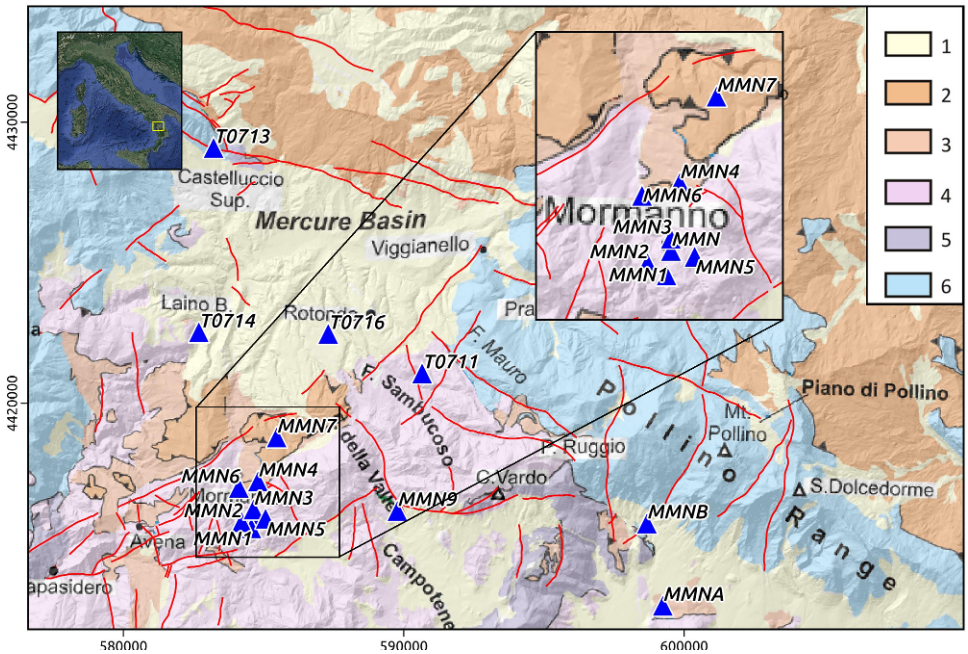

Figure 5.1: Geological and topographic map of the western Mt. Pollino area modified after Brozzetti et al. (2017). Red lines show known faults, blue triangles are the used seismic stations. Key: 1 = Sin-extensional deposits of the continental basins and of the Castrovillari basin; 2 = Allochthonous Liguride unit; 3 = Fiume Lao schist formation; 4 = Apennine Platform western Unit; 5 = Metalimestones and metapelites of the San Donato metamorphic core; 6 = Apennine Platform eastern Unit.

Site effects and polarization analysis have been assessed for seismic risk mitigation purpose because of the high number of stations installed in the area, also very close to each other nearby the village of Mormanno, highly damaged by the M5.0 event. The 15 seismic stations used in this work have been installed in the area in different phases of the swarm. Some of them were operating for several months, while some others just for few days.

5.3.1 HVSR method applied to seismic noise

The first step of the analysis is the application of the HVSR method to seismic noise recordings. Several hours of noise recordings have been selected for each available site. Recordings affected by transient signals as passages of vehicles, spikes due to electronic problems, or instrumental interruptions have been discarded, in order to get stable results. At least 20 hours of noise recordings, up to 37 hours (as in the case of the station MMN), have been selected for each site. The recordings have been selected at different time during the day and at night, for different weekdays during several months, taking into account daily and seasonal environmental changes (Figure 5.2).

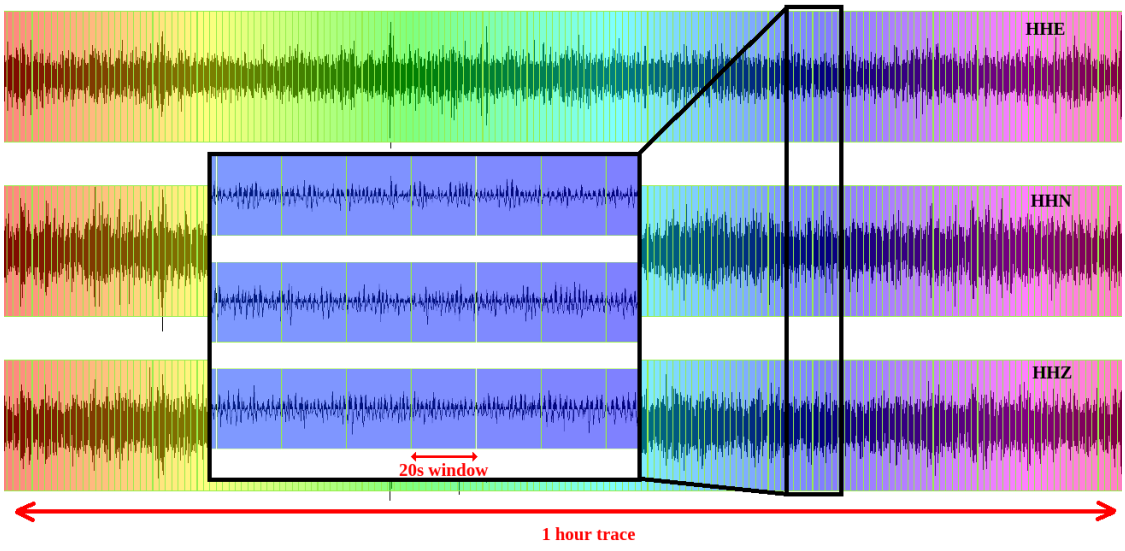

Figure 5.2: 1-hour traces of seismic noise recordings at the station MMN. From top to bottom: East-West, North-South and vertical component. The foreground image shows in more detail an example of the 20s window used for this analysis. No overlapping occur between two adjacent windows.

The HVSR curves were computed through different steps:

- each hour-long seismic noise trace have been divided in 180 windows lasting for 20 seconds. This is done for all the three components: North-South, East-West, Vertical;
- the velocity Fourier spectra have been computed through the Fast Fourier Transform (FTT) algorithm for each 20s-window;
- by using the amplitude of velocity Fourier spectra of the N, S and vertical components of the $i-th$ 20s-window, the associated HVSR curve has been computed;

- the HVSR computation have been repeated for all the 20s-windows, by using at least 20 hours of seismic noise recordings, at each of the 15 sites;

- all the HVSR curves achieved for each site have been averaged and standard deviation has been computed. These curves have finally been plotted in the frequency range 0.5 - 20 Hz, large enough for the purpose of this work.

5.3.2 HVSR method applied to earthquakes

The HVSR has been performed using local and regional earthquakes selected in the time range between 2010 and 2014. A signal-to-noise ratio greater than 3 in the $0.5 - 10Hz$ frequency band has been required to retain the events. In the case of a limited number of events recorded by few seismic stations (MMNA, MMNB, MMN2, MMN3, MMN5) the SNR threshold has been lowered to 2. In the case of regional earthquakes 20s windows of analysis, that included direct S-waves and early coda, have been selected to perform the HVSR curves. In the case of local events 10s windows of analysis has been chosen instead. Using these windows, a single HVSR curve has been obtained for each event recorded at that site. These curves have been displayed individually and the average has been computed. To test the stability of the results, the earthquakes HVSR curves have also been compared with the ones obtained using a 10s window of noise recorded before the event. The analysis has been performed using 83 earthquakes recorded at 15 sites for a total amount of 276 HVSR curves. The number of earthquake HVSR curves at each site ranges from a minimum of 7 up to 52 curves.

5.3.3 Polarization analysis of seismic noise

The presence of directional effects have been studied through the polarization analysis of noise recordings computed in the time domain. The polarization direction given by the eigenvectors of the covariance matrix associated with the largest eigenvalue have been computed (Section 5.2). The polarization azimuth, the angle between the north and the projection of the polarization vector on the horizontal plane, have been evaluated at different frequency ranges (1 - 2 Hz, 2 - 4 Hz, 3 - 6 Hz and 4 -8 Hz). Then they have been plotted in polar histograms with azimuth shown in intervals of 10° to reveal likely frequency dependence. To assess the reliability of the results the tool H/V *rotate*, included in the software GEOPSY, has been used to display the HVSR as a function of both azimuth and frequency.

5.3.4 Results

Seismic Noise HVSR curves. The noise HVSR curves computed at the 15 selected sites are shown in Figure 5.3. The red lines represent the average HVSR curves. The hours of analyzed noise is shown on the top left side of each panel. This number ranges from 20 to 37, depending on the operating time period of each station. The standard deviation is shown using black solid lines (Figure 5.3).

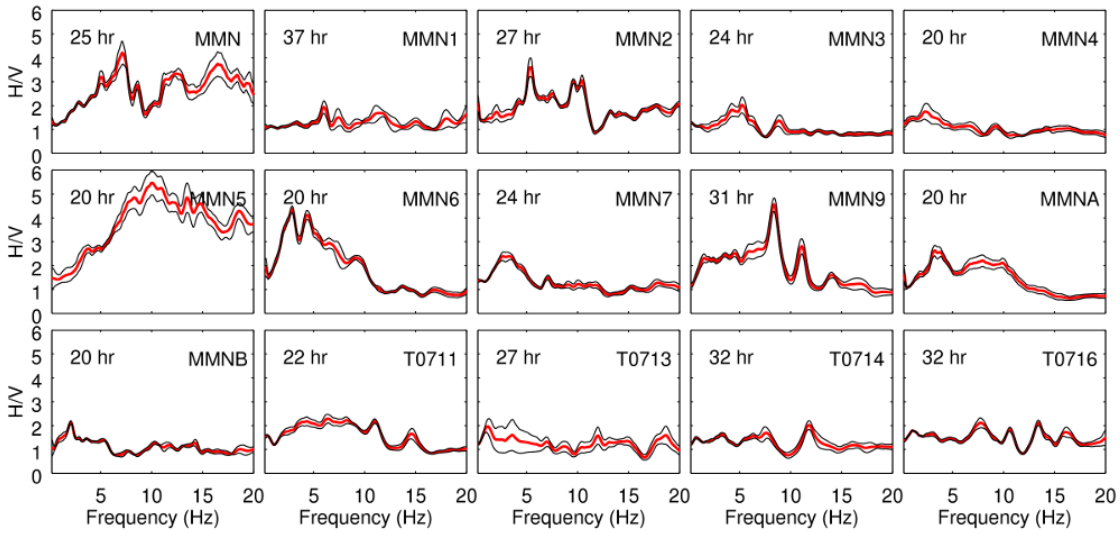

Figure 5.3: Horizontal-to-vertical spectral ratio (HVSR) average curve and its standard deviation obtained from the analysis of noise recordings at the 15 studied sites. The number of hours of analyzed data is written in each plot. Modified after *Napolitano et al.* [2018]

The curves reveal interesting characteristics that have been interpret as follows:

- MMN1, MMN3, MMN4, MMN7, MMNB, T0711, T0713, T0714, and T0716 are sites characterized by flat HVSR curves, nearly always less than 2, with some weak peaks between 2 and 3. Further, MMN7 and T0711 are characterized by nearly flat HVSR. The former shows a broad peak of amplitude greater than 2 in the 2 – 4 Hz frequency range, while the latter HVSR slightly higher 2 in the frequency range between 3 and 12 Hz. The site T0713, although showing flat HVSR curves in the entire considered frequency band, it shows the highest standard deviation, particularly between 1 and 8 Hz. The shallow lithology consists of compact limestone at seven of these nine sites. In fact, MMN4 and T0716 are located on fractured limestone and recent deposits, respectively (Figure 5.1)

- The sites MMN and MMN5 show HVSR higher than 2 at any frequency greater than 3 Hz. At MMN two peaks of amplitude 4 at 7 Hz and 16 Hz are clearly distinguishable, whereas MMN5 shows a broad peak of amplitude greater than 5 at 10 Hz. These results indicate that the two sites are affected by a pretty high amplification, even though they are situated on competent local lithology;

- At MMN2, the HVSR curve is greater than 2 in the 4 – 11 Hz frequency range, with a sharp peak of amplitude 3.5 around 5.5 Hz and two close peaks of amplitude around 3 at 9.5 Hz and 10.5 Hz. The high peaks at this site were unexpected considering the competent local lithology on which the station is installed;

- The site MMN6, located upon competent rock (limestone), shows HVSR values greater than 2 in the 1 – 10 Hz frequency range, with two separate peaks of amplitude 4 at 2.8 Hz and 4.3 Hz;

- MMN9 shows values of HVSR greater than 2 in the 1 – 9 Hz frequency range and two peaks around 8 Hz and 11 Hz. The peak at 8 Hz is characterized by amplitude of 4.5, the highest peak among those observed in this study. The observed HVSR is compatible with the local geology characterized by consolidated deposits of unknown thickness;

- At MMNA and T0711, the HVSR curves are characterized by values around 2 in a wide-frequency band between 2 and 12 Hz, but without any clear peaks. MMNA station was installed upon schists of poor competence, whereas T0711 site is characterized by quite competent dolostones.

Summarizing these results, MMN1, MMN3, MMN7, MMNB, T0711, T0713 and T0714 are sites characterized by negligible site effects, in agreement with the local competent lithology. The sites MMN4 and T0716 are also characterized by small or negligible amplification, even though the local geology consists of low-competent formations. Finally the sites MMN, MMN2, MMN5, MMN6 and MMN9 show at least one peak of amplitude greater than 3 at frequency lower than 10 Hz. However, these four sites are installed on competent soil. This means that the cause of their amplification must be independent from the local geological structure. The results related to MMN and MMN2 are of particular interest for engineering and risk mitigation purposes, being these stations installed inside the village of Mormanno. The small standard deviation (less than 0.3) at each station, except for T0713, highlights the stability of the resulting HVSR curves.

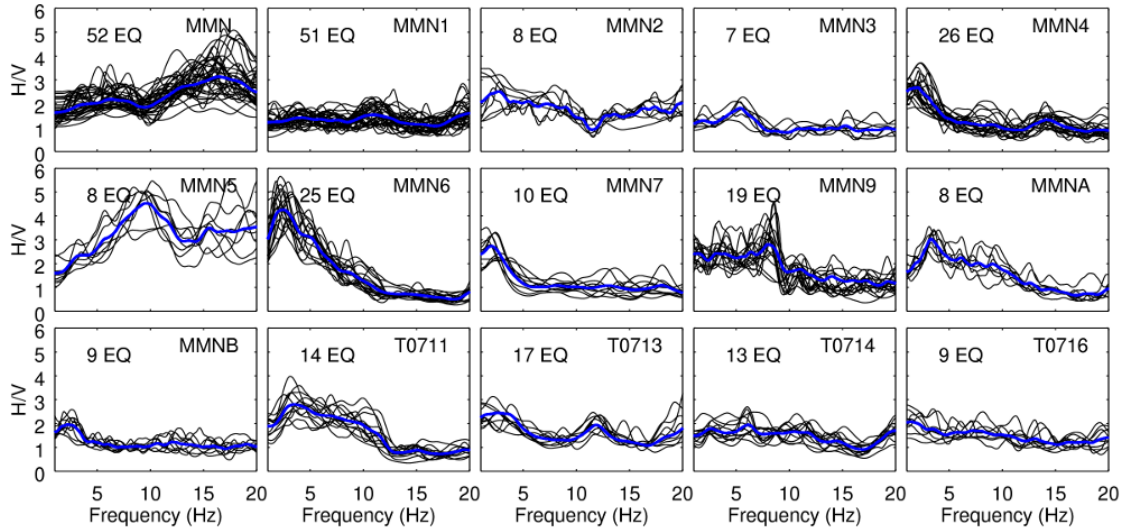

Figure 5.4: Results of HVSR obtained from the analysis of earthquakes at the 15 sites studied. Each plot shows the results of individual events by the thin line and the average by the thick line. The number of analyzed earthquakes is written in each plot. EQ, earthquake. Figure 4 from *Napolitano et al.* [2018]

Earthquakes HVSR and comparison with noise HVSR curves. The results obtained from the HVSR analysis of 83 local and regional earthquakes at the 15 chosen sites are shown in Figure 5.4 by 276 HVSR curves. In each panel, the thin black line represent the HVSR curve for a single analyzed earthquake, while the thick blue solid line represents their average.

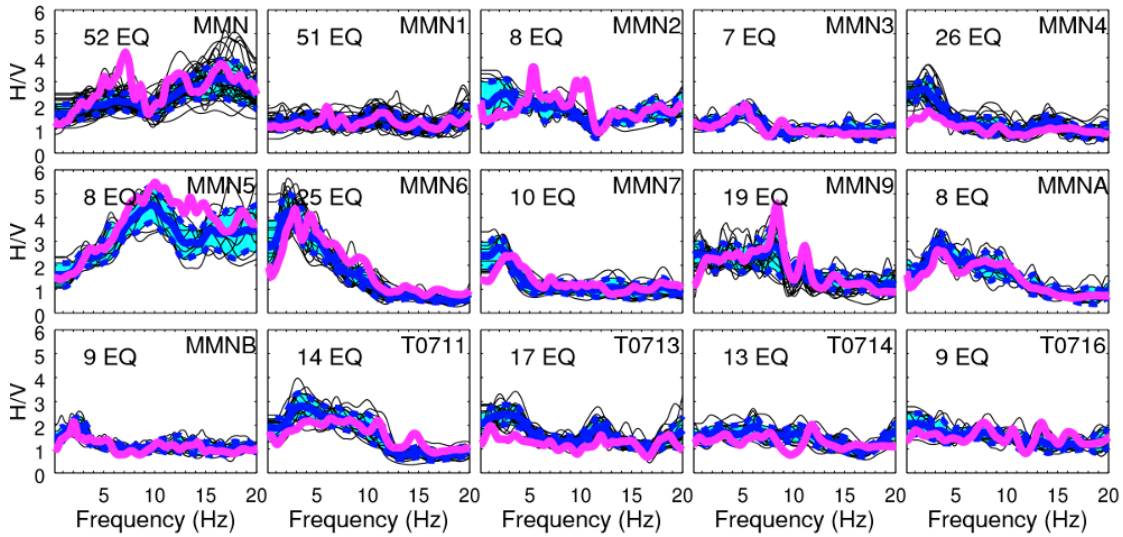

Figure 5.5: Comparison between earthquakes (thin dark lines) and average seismic noise (thick violet line) HVSR at each of the analyzed sites. The earthquake HVSR average is shown by a thick continuous blue line, whereas its standard deviation is shown by thick dashed blue lines. EQ, earthquake.

The number of analyzed earthquakes varies from site to site, from a minimum of 7 events at the site MMN3 to a maximum number of 52 events at MMN. This clearly depends on the data availability at these seismic stations. Figure 5.5 shows in addition the comparison between the earthquake HVSR curves and the average noise HVSR, whose mean value is represented by the solid violet line. The average earthquake HVSR curves are shown using thick solid blue lines, while the thick dashed blue lines represent the standard deviation. The distance between average and standard deviation curves is filled by cyan color.

The results obtained by earthquake HVSR are summarized in the following itemize. They have also been compared with the noise HVSR, highlighting similarities and differences that can help to improve the geological interpretation:

- the quite flat earthquake HVSR values shown at the sites MMN1, MMN3, MMNB, T0711, T0714, and T0716 suggest the absence of strong resonance associated with the local geological structure. Furthermore the earthquakes HVSR curves are very similar to those computed using seismic noise and most of their values are between 1 and 2. Among all these five sites, only T0716 is located on low-competent lithology;

- at MMN, the earthquake HVSR reaches the highest amplitude at frequency greater than 12 Hz. The noise and earthquakes HVSR curves are similar, except for the sharp peak at 7 Hz;

- at MMN2 there are many differences between noise and earthquakes HVSR. For frequencies lower than 11 Hz these curves are quite different. The three peaks at 5.5, 9.5 and 10.5 Hz are clearly discernible in the noise, not present in the earthquake HVSR. This means that those peaks characterizing the noise are not produced by a resonance of the local structure, which is composed by limestone (competent lithology). They have been interpreted as due to topography effects. Indeed, the the site is located on the edge of a small ridge. The polarization analysis supports this conclusion, as shown below.

- the sites MMN4 and MMN7 show quite similar noise and earthquake HVSR curves. They are both characterized by a nearly flat trend for frequencies greater than 4 Hz. They both also show a peak around 3 at frequencies 1-2 Hz. This is in agreement with the average noise HVSR for MMN7, not very clear at MMN4;

- at MMN5 noise and earthquakes HVSR curves are quite similar and show the highest peaks among the 15 sites, that is around 5 at some frequencies greater than 8 Hz;

- at MMN6 a high peak at frequencies 1-3 Hz and a regular decreasing amplitude up to 12 Hz is clearly visible in both noise and earthquakes HVSR curves. The only difference is that the two peaks around 2.8 and 4.3 Hz are not clearly separated in the earthquakes HVSR.

Resuming the comparison between noise and earthquake HVSR curves at each site, some features are remarkable. In some cases both noise and earthquakes curves are flat and very similar to each other (MMN1, MMN3, MMN4, MMN7, MMNB, T0714, T0716), meaning absence of site effects. Other 4 sites (MMN6, MMN9, MMNA and T0711) show curves characterized by very similar trends even in the case of amplifications or sharp peaks. This trend can be related most likely to local geological features of the soil - bedrock interface. Significant discrepancies between earthquake and noise HVSR curves are observed at MMN, MMN2, MMN5 and T0713. These discrepancies cannot be interpreted as due to local geological features of the soil, because in this case the same trend shoud have been observed. Other reasons have to be investigated to explain the different shape of the curves.

Polarization analysis. A useful tool to explain the differences between noise and earthquakes curves at MMN, MMN2, MMN5 and T0713 is the evaluation of the direction of particle motion in the horizontal plane. The polarization analysis of seismic noise have been performed using band-pass filtered signals in four frequency bands: 1-2 Hz, 2-4 Hz, 3-5 Hz, 4-8 Hz.

In Figures 5.6 and 5.7 polar histograms are shown in pairs with different colors covering the four frequency bands. In more detail, Figure 5.6 shows polar histograms in the frequency band 1 - 2 Hz (blue/cyan slices) and 2 - 4 Hz (red/transparent slices), while Figure 5.7 shows polar histograms in the frequency band 3 - 5 Hz (blue/cyan slices) and 4 - 8 Hz (red/transparent slices).

The first evidence is that only MMNA and T0714 show an isotropic polarization distribution at any frequencies, while at MMN4, MMN5, MMN7 and MMN9 the polarization is only isotropic at 1-2 Hz. At the other sites the polarization of the horizontal particle motion is well-defined and in some cases it can clearly change with the frequency. In order to verify that change with the frequency another contour plot have been added. It

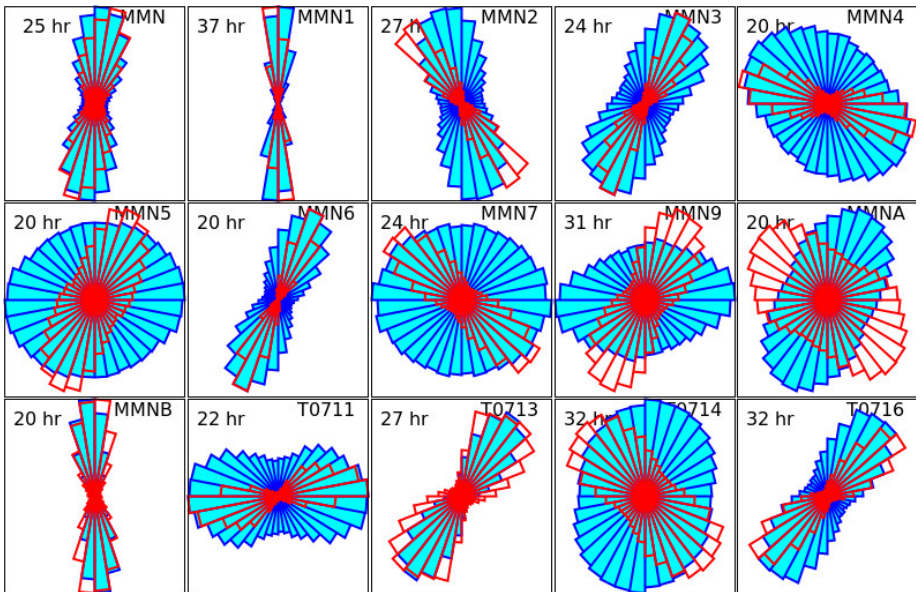

Figure 5.6: Stacked and normalized polar histograms showing the distributions of polarization azimuth in the frequency band 1–2 Hz (blue lines) and 2–4 Hz (red lines) at each station. The number of hours of analyzed seismic noise is written in each plot. Figure 8 from *Napolitano et al.* [2018]

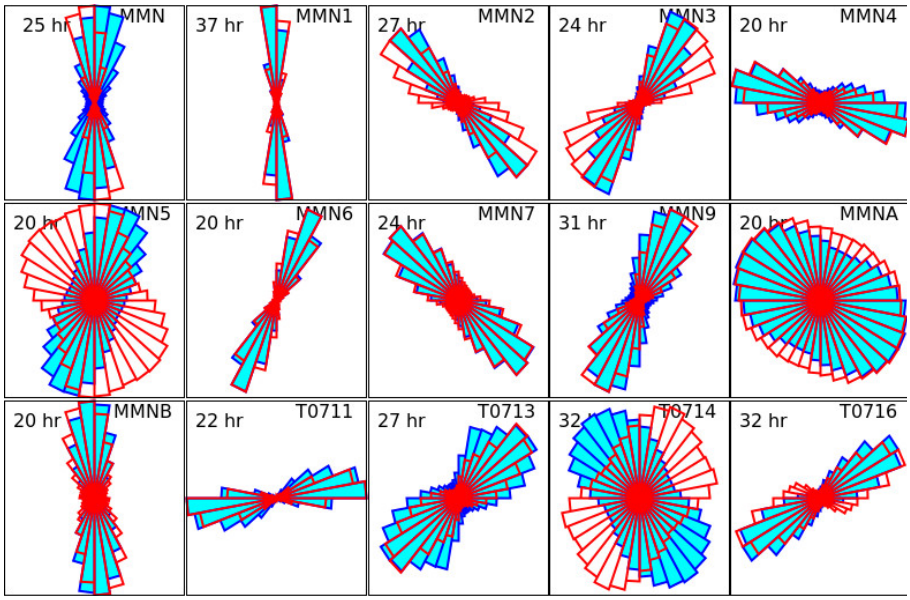

Figure 5.7: Stacked and normalized polar histograms showing the distributions of polarization azimuth in the frequency band 3–5 Hz (blue lines) and 4–8 Hz (red lines) at each station. The number of hours of analyzed seismic noise is written in each plot.Figure 9 from *Napolitano et al.* [2018]

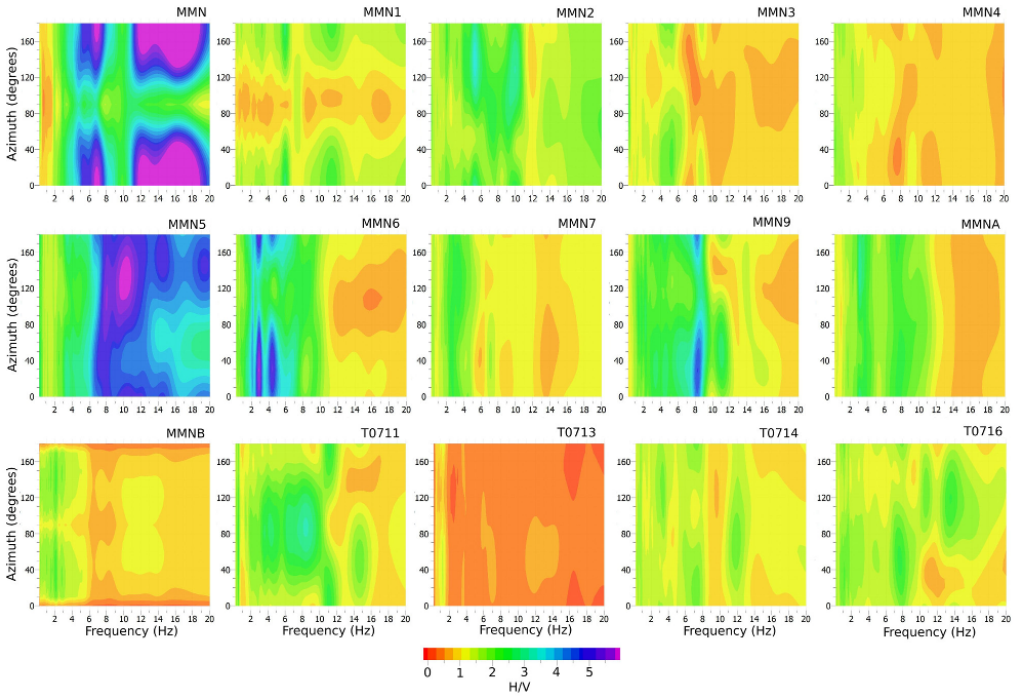

Figure 5.8: Frequency–azimuth horizontal-to-vertical (H/V) analysis. Each plot shows the H/V ratio versus frequency and azimuth. The color scale shown at the bottom is the same for all plots.Figure 10 from *Napolitano et al.* [2018]

is obtained using the software GEOPSY and shown in Figure 5.8. It shows HVSR curves plotted as a function of both frequency and azimuth, ranging from 0° to 180°. The main peaks that characterize MMN6 at 3 and 5 Hz and the other two peaks for MMN9 at 8 and 11 Hz are strongly polarized both between 0° – 80° and 160° – 180°. Almost the same angle is covered by the main peaks at MMN. The sites MMN1 and MMNB show a north-south polarization at all frequencies, T0711 a pretty east-west polarization, T0713 and T0716 a northeast-southwest polarization. The three peaks at the site MMN2 (at 5.5, 9.5 and 10.5 Hz) are polarized between almost 110° – 180°. The polarization of the peak that characterize MMN3 around 2 at 5 Hz is orthogonal compared to the one of MMN2, that means between 10° – 80°. Because the direction of polarization are very different from site to site, even at a distance as short as a few hundred meters, as for the sites MMN, MMN1, MMN2, MMN3 and MMN5, it is clearly evident that the source may not be a feature of the background noise. The final aim of this work is to link all the HVSR and polarization results with topography and presence of faults, that may be the main causes of site effects at MMN, MMN2, MMN5, T0713, where the discrepancy of the shape of the HVSR curves is extremely evident.

5.3.5 Discussion and conclusions

Site effects have been evaluated through the analysis of the HVSR curves both on the noise and local-to-regional earthquakes recorded by 15 seismic stations in the area. The analysis have been improved through the assessment of the polarization azimuth to better understand the cause of the amplification effects at some close sites. The comparison of noise and earthquakes HVSR curves show that they are quite similar at most of the analyzed sites. Clear discrepancies in noise and earthquakes HVSR curves are observed at 4 sites (MMN, MMN2, MMN5 and T0713). The possible source of these differences has been investigated.

First, the relationship between polarization and topography has been investigated. The angle between polarization direction and the slope of the closest mountain to each site have been resumed in Table 5.1.

Table 5.1: Relationship between Polarization and Slope

Site	Angle between Polarization and Slope
MMN	Parallel
MMN2	Parallel
MMN4	Parallel
MMN9	Parallel
MMNB	Parallel
T0711	Parallel
T0716	Parallel
T0713	Roughly Parallel
MMN7	Roughly Parallel
MMN1	Roughly Parallel
MMN3	Roughly Parallel
MMN6	Roughly Parallel
MMN5	Roughly Parallel
MMNA	Undefined (isotropic)
T0714	Undefined (isotropic)

The polarization direction is similar to the slope direction at nine of the analyzed sites, whereas it is normal at three other sites. The last three sites do not show a well-defined polarization. Those results seem to be in perfect agreement with the ones obtained in previous articles in other areas. A strong relationship between polarization direction and topography has been highlighted.

The relationship between the polarization direction and strike of the known faults close to the analyzed sites (at distances smaller than 250 m) has been taken into account

as well, as shown in Table 5.2.

Table 5.2: Relationship between Polarization and Known faults

Site	Distance to the fault (m)	Angle between Polarization and Strike
MMN4	About 200	60-70
MMN9	170	60-70
MMNB	30	40-50
T0711	240	85-90
T0713	30	35-40

Only five sites are located at a distance smaller than 250 meters from known faults and the angle between strike of the fault and polarization direction is roughly normal. But considering all the sites, no clear effects in the seismic wave-field can be ascribed to near faults at the analyzed sites, due to the small size of the faults, which makes them not capable to trap seismic waves, creating a clear polarization direction.

At 11 of the 15 analyzed sites, the noise HVSR curves are very similar to the average noise HVSR, whether they show peaks or they are flat. In both cases, the crucial role is played by the lithology, so the curves are *representative of the site*. Indeed, if a peak or an amplification is clearly distinguishable in both noise and earthquake HVSR curves, it can be ascribed to the contrast of impedance between bedrock and soil in the subsurface, as distinctly shown at MMN6 and MMN9. In the case of discrepancies between the noise and the earthquakes HVSR curves, as in the case for MMN, MMN2, MMN5 and T0713, the main cause of peaks or amplification cannot be ascribed to lithology, but rather to the topography or to the local known faults, after excluding other less reliable causes. Through the polarization analysis, the contribution of the faults has been excluded, due mainly to their small size. All of these sites are characterized by the polarization direction parallel to the slope direction of the surrounding topography. For instance, MMN2 is at the edge of a ravine, and the observed polarization is very narrow and normal to the rim for frequency greater than 2 Hz, becoming isotropic at lower frequency. MMN and MMN2 are installed inside the village of Mormanno, becoming of interest for engineering purposes and for damage scenario forecast in case of earthquakes. These results also highlight a crucial point: *much care must be taken when studying site effects*. Although the results of noise HVSR curves are stable and reliable at all the considered sites, characterized by a very small standard deviation, they are not necessarily representative of the site effects due to the local geological structure because

there may be local conditions which prevent the efficiency of the HVSR method. In fact, an amplification of the ground motion have been found at four sites that correlate much better with the topography than the geological structure of the subsurface. The results obtained indicate that in mountainous regions where the local geology is far from a horizontal layered structure, the HVSR alone is not sufficient to characterize the site response, but it has to be improved using other methods of analysis in order to have a more realistic interpretation of the causes of these site effects of an area. The Pollino region is a very challenging area where the topography and the fault zones coexist and the interpretation of the causes behind site effects becomes tough.

CHAPTER 6

CONCLUSION

The Pollino seismic sequence (Southern Italy) occurred between 2010 and 2014 has been analyzed with the aim of a complete study of source, propagation path and site effects. Earthquakes of the sequence and nearby have been used to perform a detailed imaging of the seismogenic volume responsible for the swarm, to estimate scattering and absorption contribution to the total attenuation of coda waves due to the medium properties surrounding the swarm, and to assess local site effects for seismic risk mitigation.

Starting from the source analysis, one of the simplest known methods to perform relative locations, the *master-slave* method, has been applied to relocate the hypocenters within clusters of similar waveforms, likely produced by the same fault patch of a larger and more complex seismogenic volume. An enhancement of the imaging of the seismogenic volume, that could only be guessed using absolute locations, has been obtained. Despite the difficulties due to the lack of a sufficient number of seismic stations that recorded the events, striking outcomes about the fault shape and dynamics, and the swarm development in space and time have been obtained. The hypocenter distribution achieved using relative location depicted a seismogenic volume characterized by strike 150°, dip 48° and an overall normal fault kinematics.

The seismogenic volume involved in the swarm is estimated to be $5 \times 2 \times 2 km^3$, at a depth ranging from 4.5 to 6.5 km below the sea level. The orientation of this fault seemed to be strongly in agreement with the focal mechanism of the mainshock of M5.0 computed during the swarm (strike=166°, dip=47°, rake=−84°). The agreement seems to suggest that the mainshock occurred on the same seismogenic volume, south of the

swarm and deeper if compared to the average depth of the swarm. The results highlight that the seismogenic volume involved during the Pollino sequence should be bigger than the one expected for the strongest event of the swarm, the M5.0 occurred on 25^{th} October 2012. This statement seems to be unmatched if the historical seismicity of the area is taken into account. In fact, since no events of $M > 6.5$ have been recorded in historical time, the region is classified as the most significant seismic gap in Italy. However, paleo-seismological investigations found evidence of at least two strong earthquakes ($M > 6.5$) occurred in the SE area of the Pollino range in the last 10000 years.

The detailed analysis of the last Pollino swarm proposed in this thesis may be very helpful in understanding the reason of the discrepancy between the lack of strong events and the presence of faults capable of generating them. Many papers suggest that during swarm-like sequences most of the events may be attributed to transient forcing. Evidences of aseismic transient slip along with micro-seismic activity have been recorded during the last Pollino swarm, probably favoured by the presence of fluids, also suggested by the high v_P/v_S anomaly found in the area. Starting from these results, it was necessary to prove with physical evidences the possible presence of fluids likely filling connected fractures, and their role in the evolution of the swarm. The application of peak-delay and coda Q_c method to part of the events of the swarm and nearby have been considered suitable to reach this goal and to separate scattering and absorption contribution to the total attenuation of coda waves. The results are very striking and highlight the main geological features of the medium surrounding the swarm in terms of heterogeneities and presence of fluids.

Interestingly enough it is the high scattering and high absorption pattern that characterize the 2D map at different frequencies. At low frequencies this pattern marks the SE sector of the map, where the Castrovillari basin is located, highlighting the biggest structures of the area, where the strongest events of the area occurred as highlighted in previous works. At higher frequencies, smaller structures located in the middle of the Pollino Range scatter, and notably they include the faults responsible for the 2010-2014 swarm. These results have been interpreted as a very complex set of fluid-filled connected fractures, opening new pathways for fluid migration in the area. The fluids seem to be stuck in the area due to the presence of a barrier extending from Mt. Sirino to Lake Pertusillo, marked by a stable high scattering and low absorption pattern. This shield between the southern Pollino Range and the northern Val D'Agri has been interpreted as a highly fractured carbonatic block, insulated by clay formations. In the light of what has been asserted and proved by physical evidence, future considerations about seismic

risk assessment must take these results into account.

Moreover, using the relative location of hypocenters achieved, it has been possible to follow the detailed evolution of the swarm in space and time, within the two analyzed periods. Considering the significant results about the likely transient process driving the swarm in previous papers, and the combined results of this thesis in terms of enhancement of the locations and presence of fluids, our understandings about the physical and rheological condition of the system of faults that led to the simultaneous seismic and aseismic strain release could be improved. The Pollino seismic swarm was triggered by a long lasting slow slip event that repeatedly loaded to failure fault patches with more brittle behaviour producing the observed seismic swarm. The massive presence of fluids permeating connected structures, demonstrated with physical evidences in this thesis, confirm such scenario as the likely habitat to produce long lasting earthquake swarm and slow slip event. Unfortunately geodetic data were not available at the beginning of the swarm, for lack of instrumentation, but is likely that this transient started before the swarm triggering. The combination of aseismic and seismic slip during the 2010-2014 Pollino sequence, equivalent to a M_w5.5 earthquake, might have partially released the tectonic strain accumulated over time in the northern part of the Pollino fault system. The 1998 M_w5.6 event also contributed to release strain in the region. However the proposed analysis suggests that the fault activated are much larger than the area ruptured in both seismic sequences, therefore in principle able to accommodate large magnitude events, already present in paleo-seismological records. For this reasons, a possible occurrence of a strong event in the area cannot be excluded

The results achieved corroborate the view of the Pollino as an area characterized by a high seismic hazard. For this reason the large number of recordings of the seismic stations installed in different years has been used to assess the local site effects. Horizontal-to-Vertical Spectral Ratio (HVSR) on both noise and earthquakes, and polarization analysis have been performed at 15 sites arranged in the area. The majority of the sites show the same HVSR curves using noise and earthquakes, whether they are flat or not. At few sites a discrepancy between noise and earthquakes HVSR curves has been evident. Through the use of polarization analysis it has been possible to ascribe these discrepancies to topographic effects. Amplification of seismic waves have been identified at some stations installed in the aged village of Mormanno, already damaged during the swarm, but future deeper analyses are suggested for engineering purposes and for damage scenario forecast in case of earthquakes.

One of the most important future development of this work could be the application

and the enhancement of the applied techniques to other tectonic settings. This has to be done in order to improve the actual knowledge about the seismic/aseismic interaction to release the strain of an area, to better understand the role of fluids in favouring the occurrence of slow strain events and to give reliable results in order to assess and mitigate the seismic risk of an area. The same technique may also be applied to areas of exploitation of geo-resources. In this case the imaging of the fluids beneath the subsurface could be more accurately depicted, giving new insights about the fluid migration through smaller fractures that generated low-magnitude man-induced swarms.

BIBLIOGRAPHY

Aki, K., and B. Chouet, Origin of coda waves: source, attenuation, and scattering effects, *Journal of geophysical research*, *80*(23), 3322–3342, 1975.

Aki, K., and P. G. Richards, *Quantitative seismology*, 2002.

Amoroso, O., G. Russo, G. De Landro, A. Zollo, S. Garambois, S. Mazzoli, M. Parente, and J. Virieux, From velocity and attenuation tomography to rock physical modeling: Inferences on fluid-driven earthquake processes at the irpinia fault system in southern italy, *Geophysical Research Letters*, *44*(13), 6752–6760, 2017.

Andrews, D., Objective determination of source parameters and similarity of earthquakes of different size, *Earthquake source mechanics*, *37*, 259–267, 1986.

Aster, R. C., B. Borchers, and C. H. Thurber, *Parameter estimation and inverse problems*, Elsevier, 2018.

Bai, L., Z. Wu, T. Zhang, and I. Kawasaki, The effect of distribution of stations upon location error: Statistical tests based on the double-difference earthquake location algorithm and the bootstrap method, *Earth, Planets and Space*, *58*(2), e9–e12, 2006.

Barberi, G., M. Cosentino, A. Gervasi, I. Guerra, G. Neri, and B. Orecchio, Crustal seismic tomography in the calabrian arc region, south italy, *Physics of the Earth and Planetary Interiors*, *147*(4), 297–314, 2004.

Bard, P.-Y., S. Team, et al., Guidelines for the implementation of the h/v spectral ratio technique on ambient vibrations, in *Measurements, processing and interpretation*, 2004.

Bodin, P., and S. Horton, Broadband microtremor observation of basin resonance in the mississippi embayment, central us, *Geophysical Research Letters*, *26*(7), 903–906, 1999.

Bonamassa, O., and J. E. Vidale, Directional site resonances observed from aftershocks of the 18 october 1989 loma prieta earthquake, *Bulletin of the Seismological Society of America*, *81*(5), 1945–1957, 1991.

Bonilla, L. F., J. H. Steidl, G. T. Lindley, A. G. Tumarkin, and R. J. Archuleta, Site amplification in the san fernando valley, california: variability of site-effect estimation using the s-wave, coda, and h/v methods, *Bulletin of the Seismological Society of America*, *87*(3), 710–730, 1997.

Bonnefoy-Claudet, S., A. Köhler, C. Cornou, M. Wathelet, and P.-Y. Bard, Effects of love waves on microtremor h/v ratio, *Bulletin of the Seismological Society of America*, *98*(1), 288–300, 2008.

Borcherdt, R. D., Effects of local geology on ground motion near san francisco bay, *Bulletin of the Seismological Society of America*, *60*(1), 29–61, 1970.

Borcherdt, R. D., and J. F. Gibbs, Effects of local geological conditions in the san francisco bay region on ground motions and the intensities of the 1906 earthquake, *Bulletin of the Seismological Society of America*, *66*(2), 467–500, 1976.

Brozzetti, F., P. Boncio, G. Lavecchia, and B. Pace, Present activity and seismogenic potential of a low-angle normal fault system (città di castello, italy): Constraints from surface geology, seismic reflection data and seismicity, *Tectonophysics*, *463*(1-4), 31–46, 2009.

Brozzetti, F., D. Cirillo, R. de Nardis, M. Cardinali, G. Lavecchia, B. Orecchio, D. Presti, and C. Totaro, Newly identified active faults in the pollino seismic gap, southern italy, and their seismotectonic significance, *Journal of Structural Geology*, *94*, 13–31, 2017.

Buech, F., T. Davies, and J. Pettinga, The little red hill seismic experimental study: Topographic effects on ground motion at a bedrock-dominated mountain edificelittle red hill seismic experimental study: Topographic effects on ground motion, *Bulletin of the Seismological Society of America*, *100*(5A), 2219–2229, 2010.

Calvet, M., and L. Margerin, Lapse-time dependence of coda q: Anisotropic multiple-scattering models and application to the pyrenees, *Bulletin of the Seismological Society of America*, *103*(3), 1993–2010, 2013.

Calvet, M., M. Sylvander, L. Margerin, and A. Villaseñor, Spatial variations of seismic attenuation and heterogeneity in the pyrenees: Coda q and peak delay time analysis, *Tectonophysics*, *608*, 428–439, 2013.

Chávez-García, F. J., M. Rodríguez, E. H. Field, and D. Hatzfeld, Topographic site effects. a comparison of two nonreference methods, *Bulletin of the Seismological Society of America*, *87*(6), 1667–1673, 1997.

Cheloni, D., N. D'Agostino, G. Selvaggi, A. Avallone, G. Fornaro, R. Giuliani, D. Reale, E. Sansosti, and P. Tizzani, Aseismic transient during the 2010–2014 seismic swarm: evidence for longer recurrence of m 6.5 earthquakes in the pollino gap (southern italy)?, *Scientific reports*, *7*(1), 576, 2017.

Cinti, F., M. Moro, D. Pantosti, L. Cucci, and G. D'addezio, New constraints on the seismic history of the castrovillari fault in the pollino gap (calabria, southern italy), *Journal of Seismology*, *6*(2), 199–217, 2002.

Cinti, F. R., L. Cucci, D. Pantosti, G. D'Addezio, and M. Meghraoui, A major seismogenic fault in a 'silent area': The castrovillari fault (southern apennines, italy), *Geophysical Journal International*, *130*(3), 595–605, 1997.

Clemente-Chavez, A., F. Zúñiga, J. Lermo, A. Figueroa-Soto, C. Valdés, M. Montiel, O. Chavez, and M. Arroyo, On the behavior of site effects in central mexico (the mexican volcanic belt, *Natural Hazards and Earth System Sciences*, *14*(6), 1391, 2014.

Cliet, C., and M. Dubesset, Three-component recordings: Interest for land seismic source study, *Geophysics*, *52*(8), 1048–1059, 1987.

D'Agostino, N., E. D'Anastasio, A. Gervasi, I. Guerra, M. R. Nedimović, L. Seeber, and M. Steckler, Forearc extension and slow rollback of the calabrian arc from gps measurements, *Geophysical Research Letters*, *38*(17), 2011.

De Gori, P., et al., 2010-2014 seismic activity images the activated fault system in the pollino area, at the appennines-calabrian arc boundary region, *GNGTS-Gruppo Nazionale di Geofisica della Terra Solida*, 2014.

De Siena, L., M. Calvet, K. J. Watson, A. Jonkers, and C. Thomas, Seismic scattering and absorption mapping of debris flows, feeding paths, and tectonic units at mount st. helens volcano, *Earth and Planetary Science Letters*, *442*, 21–31, 2016.

De Siena, L., A. Amoruso, E. D. Pezzo, Z. Wakeford, M. Castellano, and L. Crescentini, Space-weighted seismic attenuation mapping of the aseismic source of campi flegrei 1983–1984 unrest, *Geophysical Research Letters*, *44*(4), 1740–1748, 2017.

Deichmann, N., and M. Garcia-Fernandez, Rupture geometry from high-precision relative hypocentre locations of microearthquake clusters, *Geophysical Journal International*, *110*(3), 501–517, 1992.

Del Pezzo, E., J. Ibanez, J. Prudencio, F. Bianco, and L. De Siena, Absorption and scattering 2-d volcano images from numerically calculated space-weighting functions, *Geophysical Journal International*, *206*(2), 742–756, 2016.

Delgado, J., C. L. Casado, A. Estevez, J. Giner, A. Cuenca, and S. Molina, Mapping soft soils in the segura river valley (se spain): a case study of microtremors as an exploration tool, *Journal of Applied Geophysics*, *45*(1), 19–32, 2000.

Dewey, J., M. Helman, S. Knott, E. Turco, and D. Hutton, Kinematics of the western mediterranean, *Geological Society, London, Special Publications*, *45*(1), 265–283, 1989.

Duval, A., P. Bard, J. Meneroud, S. Vidal, and G. Duma, Usefulness of microtremor measurements for site effect studies, in *Proceedings of the 10th European Conference on Earthquake Engineering, Vienna, Austria*, 1994.

Ferranti, L., G. Milano, and M. Pierro, Insights on the seismotectonics of the western part of northern calabria (southern italy) by integrated geological and geophysical data: Coexistence of shallow extensional and deep strike-slip kinematics, *Tectonophysics*, *721*, 372–386, 2017.

Field, E., K. Jacob, and S. Hough, Earthquake site response estimation: a weak-motion case study, *Bulletin of the Seismological Society of America*, *82*(6), 2283–2307, 1992.

Field, E. H., and K. H. Jacob, A comparison and test of various site-response estimation techniques, including three that are not reference-site dependent, *Bulletin of the seismological society of America*, *85*(4), 1127–1143, 1995.

Formisano, L., M. La Rocca, E. Del Pezzo, D. Galluzzo, C. Fischione, and R. Scarpa, Topography effects in the polarization of earthquake signals: a comparison between surface and deep recordings., *Bollettino di Geofisica Teorica ed Applicata*, *53*(4), 2012.

Frémont, M.-J., and S. D. Malone, High precision relative locations of earthquakes at mount st. helens, washington, *Journal of Geophysical Research: Solid Earth*, *92*(B10), 10,223–10,236, 1987.

Gallipoli, D., Constitutive and numerical modelling of unsaturated soil, Ph.D. thesis, University of Glasgow, 2000.

Ganev, T., F. Yamazaki, and T. Katayama, Observation and numerical analysis of soil-structure interaction of a reinforced concrete tower, *Earthquake engineering & structural dynamics*, *24*(4), 491–503, 1995.

Gasperini, P., G. Vannucci, D. Tripone, and E. Boschi, The location and sizing of historical earthquakes using the attenuation of macroseismic intensity with distancelocation and sizing of historical earthquakes using attenuation of macroseismic intensity, *Bulletin of the Seismological Society of America*, *100*(5A), 2035–2066, 2010.

Ghisetti, F., and L. Vezzani, Deformazioni pellicolari mioceniche e plioceniche nei domini strutturali esterni dell'appennino centro-meridionale (maiella ed arco morrone-gran sasso), *Mem. Soc. Geol. Ital*, *26*, 563–577, 1983.

Giampiccolo, E., S. Gresta, M. Mucciarelli, G. De Guidi, M. Gallipoli, et al., Information on subsoil geological structure in the city of catania (eastern sicily) from microtremor measurements, *Annali di Geofisica*, *44*(1), 1–12, 2001.

Gillard, D., A. M. Rubin, and P. Okubo, Highly concentrated seismicity caused by deformation of kilauea's deep magma system, *Nature*, *384*(6607), 343, 1996.

Gosar, A., R. Stopar, M. Car, and M. Mucciarelli, The earthquake on 12 april 1998 in the krn mountains (slovenia): ground-motion amplification study using microtremors and modelling based on geophysical data, *Journal of applied geophysics*, *47*(2), 153–167, 2001.

Got, J.-L., J. Fréchet, and F. W. Klein, Deep fault plane geometry inferred from multiplet relative relocation beneath the south flank of kilauea, *Journal of Geophysical Research: Solid Earth*, *99*(B8), 15,375–15,386, 1994.

Guerra, I., P. Harabaglia, A. Gervasi, A. B. Rosa, et al., The 1998-1999 pollino (southern apennines, italy) seismic crisis: tomography of a sequence, *Annals of Geophysics*, 2005.

Hainzl, S., and T. Fischer, Indications for a successively triggered rupture growth underlying the 2000 earthquake swarm in vogtland/nw bohemia, *Journal of Geophysical Research: Solid Earth*, *107*(B12), ESE–5, 2002.

Hainzl, S., and Y. Ogata, Detecting fluid signals in seismicity data through statistical earthquake modeling, *Journal of Geophysical Research: Solid Earth*, *110*(B5), 2005.

Hainzl, S., T. Fischer, and T. Dahm, Seismicity-based estimation of the driving fluid pressure in the case of swarm activity in western bohemia, *Geophysical Journal International*, *191*(1), 271–281, 2012.

Hartzell, S., A. Leeds, A. Frankel, and J. Michael, Site response for urban los angeles using aftershocks of the northridge earthquake, *Bulletin of the Seismological Society of America*, *86*(1B), S168–S192, 1996.

Hennino, R., N. Trégourès, N. Shapiro, L. Margerin, M. Campillo, B. Van Tiggelen, and R. Weaver, Observation of equipartition of seismic waves, *Physical review letters*, *86*(15), 3447, 2001.

Herrmann, R. B., Computer programs in seismology: An evolving tool for instruction and research, *Seismological Research Letters*, *84*(6), 1081–1088, 2013.

Huang, Y., J.-S. YANG, and T.-Z. ZHANG, Relocation of the bachu-jiashi, xinjiang earthquake sequence in 2003 using the double-difference location algorithm, *Chinese Journal of Geophysics*, *49*(1), 148–156, 2006.

Hunziker, J., M. Favino, E. Caspari, B. Quintal, J. G. Rubino, R. Krause, and K. Holliger, Seismic attenuation and stiffness modulus dispersion in porous rocks containing stochastic fracture networks, *Journal of Geophysical Research: Solid Earth*, *123*(1), 125–143, 2018.

Ibáñez, J. M., E. del Pezzo, M. Martini, D. Patané, F. de Miguel, F. Vidal, and J. Morales, Estimates of coda-q using a non-linear regression, *Journal of Physics of the Earth*, *41*(4), 203–219, 1993.

Imposa, S., S. Grassi, F. Fazio, G. Rannisi, and P. Cino, Geophysical surveys to study a landslide body (north-eastern sicily), *Natural Hazards*, *86*(2), 327–343, 2017.

ISIDe, Italian seismological instrumental and parametric database, 2010.

Jordan, T. H., and K. A. Sverdrup, Teleseismic location techniques and their application to earthquake clusters in the south-central pacific, *Bulletin of the Seismological Society of America*, *71*(4), 1105–1130, 1981.

Jurkevics, A., Polarization analysis of three-component array data, *Bulletin of the seismological society of America*, *78*(5), 1725–1743, 1988.

Kanai, K., and T. Tanaka, On microtremor , *Bulletin, Earthquake Institute*, *39*, 97–114, 1961.

Kobayashi, H., K. Set, S. Midorikawa, T. Samano, and Y. Yamazaki, Seismic microzoning study of mexico city by means of microtremor measurements, in *Proc. 4th International Conference on Seismic Zonation*, vol. 3, pp. 557–564, 1991.

Konno, K., and T. Ohmachi, Ground-motion characteristics estimated from spectral ratio between horizontal and vertical components of microtremor, *Bulletin of the Seismological Society of America*, *88*(1), 228–241, 1998.

La Rocca, M., D. Galluzzo, S. Malone, W. McCausland, and E. Del Pezzo, Array analysis and precise source location of deep tremor in cascadia, *Journal of Geophysical Research: Solid Earth*, *115*(B6), 2010.

Lachet, C., and P. Bard, Theoretical investigations on the nakamura's technique, 1995.

Lachet, C., and P.-Y. Bard, Numerical and theoretical investigations on the possibilities and limitations of nakamura's technique, *Journal of Physics of the Earth*, *42*(5), 377–397, 1994.

Lachet, C., D. Hatzfeld, P.-Y. Bard, N. Theodulidis, C. Papaioannou, and A. Savvaidis, Site effects and microzonation in the city of thessaloniki (greece) comparison of different approaches, *Bulletin of the Seismological Society of America*, *86*(6), 1692–1703, 1996.

Lohman, R. B., and J. J. McGuire, Earthquake swarms driven by aseismic creep in the salton trough, california, *Journal of Geophysical Research: Solid Earth*, *112*(B4), 2007.

Lunedei, E., and P. Malischewsky, A review and some new issues on the theory of the h/v technique for ambient vibrations, in *Perspectives on European earthquake engineering and seismology*, pp. 371–394, Springer, Cham, 2015.

Margerin, L., Breakdown of equipartition in diffuse fields caused by energy leakage, *The European Physical Journal Special Topics*, *226*(7), 1353–1370, 2017.

Margheriti, L., L. Wennerberg, and J. Boatwright, A comparison of coda and s-wave spectral ratios as estimates of site response in the southern san francisco bay area, *Bulletin of the Seismological Society of America*, *84*(6), 1815–1830, 1994.

Margheriti, L., et al., Emergenza nell'area del pollino: le attività della rete sismica mobile, *Rapporti Tecnici INGV*, 2013.

Mayor, J., L. Margerin, and M. Calvet, Sensitivity of coda waves to spatial variations of absorption and scattering: radiative transfer theory and 2-d examples, *Geophysical Journal International*, *197*(2), 1117–1137, 2014.

Montalbetti, J. F., and E. R. Kanasewich, Enhancement of teleseismic body phases with a polarization filter, *Geophysical Journal International*, *21*(2), 119–129, 1970.

Mucciarelli, M., and M. R. Gallipoli, A critical review of 10 years of microtremor hvsr technique, *Boll. Geof. Teor. Appl*, *42*(3-4), 255–266, 2001.

Mucciarelli, M., and G. Monachesi, A quick survey of local amplifications and their correlation with damage observed during the umbro-marchesan (italy) earthquake of september 26, 1997, *Journal of Earthquake Engineering*, *2*(2), 325–337, 1998.

Mucciarelli, M., and G. Monachesi, The bovec (slovenia) earthquake, april 1998: preliminary quantitative association among damage, ground motion amplification and building frequencies, *Journal of earthquake engineering*, *3*(03), 317–327, 1999.

Nakamura, Y., A method for dynamic characteristics estimation of subsurface using microtremor on the ground surface, *Railway Technical Research Institute, Quarterly Reports*, *30*(1), 1989.

Nakamura, Y., Clear identification of fundamental idea of nakamura's technique and its applications, in *Proceedings of the 12th world conference on earthquake engineering*, vol. 2656, Auckland New Zealand, 2000.

Napolitano, F., A. Gervasi, M. La Rocca, I. Guerra, and R. Scarpa, Site effects in the pollino region from the hvsr and polarization of seismic noise and earthquakes, *Bulletin of the Seismological Society of America*, *108*(1), 309–321, 2018.

Nogoshi, M., On the amplitude characteristics of microtremor, part ii, *Journal of the seismological society of Japan*, *24*, 26–40, 1971.

Noguera, A. M., and G. Rea, Deep structure of the campanian–lucanian arc (southern apennine, italy), *Tectonophysics*, *324*(4), 239–265, 2000.

Obermann, A., T. Planès, E. Larose, C. Sens-Schönfelder, and M. Campillo, Depth sensitivity of seismic coda waves to velocity perturbations in an elastic heterogeneous medium, *Geophysical Journal International*, *194*(1), 372–382, doi:10.1093/gji/ggt043, 2013.

Ohmachi, T., Y. Nakamura, and T. Toshinawa, Ground motion characteristics of the san francisco bay area detected by microtremor measurements, 1991.

Ozawa, S., H. Suito, and M. Tobita, Occurrence of quasi-periodic slow-slip off the east coast of the boso peninsula, central japan, *Earth, planets and space*, *59*(12), 1241–1245, 2007.

Panzera, F., G. Lombardo, C. Monaco, and A. Di Stefano, Seismic site effects observed on sediments and basaltic lavas outcropping in a test site of catania, italy, *Natural Hazards*, *79*(1), 1–27, 2015.

Panzera, F., B. Halldorsson, and K. Vogfjörð, Directional effects of tectonic fractures on ground motion site amplification from earthquake and ambient noise data: a case study in south iceland, *Soil Dynamics and Earthquake Engineering*, *97*, 143–154, 2017.

Parolai, S., et al., Site effects assessment in bishkek (kyrgyzstan) using earthquake and noise recording data, *Bulletin of the Seismological Society of America*, *100*(6), 3068–3082, 2010.

Passarelli, L., S. Hainzl, S. Cesca, F. Maccaferri, M. Mucciarelli, D. Roessler, F. Corbi, T. Dahm, and E. Rivalta, Aseismic transient driving the swarm-like seismic sequence in the pollino range, southern italy, *Geophysical Journal International*, *201*(3), 1553–1567, 2015.

Passarelli, L., et al., Pollino seismic experiment (2012-2014), *Deutsches GeoForschungsZentrum GFZ. Other/Seismic Network*, doi:10.14470/9N904956, 2012.

Patacca, E., and P. Scandone, Post-tortonian mountain building in the apennines. the role of the passive sinking of a relic lithospheric slab, 1989.

Peng, Z., and J. Gomberg, An integrated perspective of the continuum between earthquakes and slow-slip phenomena, *Nature geoscience*, *3*(9), 599, 2010.

Petukhin, A., K. Irikura, S. Ohmi, and T. Kagawa, Estimation of q-values in the seismogenic and aseismic layers in the kinki region, japan, by elimination of the geometrical spreading effect using ray approximation, *Bulletin of the Seismological Society of America*, *93*(4), 1498–1515, 2003.

Phillips, W. S., and K. Aki, Site amplification of coda waves from local earthquakes in central california, *Bulletin of the Seismological Society of America*, *76*(3), 627–648, 1986.

Piana Agostinetti, N., and A. Amato, Moho depth and vp/vs ratio in peninsular italy from teleseismic receiver functions, *Journal of Geophysical Research: Solid Earth*, *114*(B6), 2009.

Pischiutta, M., G. Cultrera, A. Caserta, L. Luzi, and A. Rovelli, Topographic effects on the hill of nocera umbra, central italy, *Geophysical Journal International*, *182*(2), 977–987, 2010.

Pischiutta, M., F. Salvini, J. Fletcher, A. Rovelli, and Y. Ben-Zion, Horizontal polarization of ground motion in the hayward fault zone at fremont, california: dominant fault-high-angle polarization and fault-induced cracks, *Geophysical Journal International*, *188*(3), 1255–1272, 2012.

Pischiutta, M., M. Pastori, L. Improta, F. Salvini, and A. Rovelli, Orthogonal relation between wavefield polarization and fast s wave direction in the val d'agri region: An integrating method to investigate rock anisotropy, *Journal of Geophysical Research: Solid Earth*, *119*(1), 396–408, 2014.

Pischiutta, M., M. Fondriest, M. Demurtas, F. Magnoni, G. Di Toro, and A. Rovelli, Structural control on the directional amplification of seismic noise (campo imperatore, central italy), *Earth and Planetary Science Letters*, *471*, 10–18, 2017.

Pitilakis, K., Site effects, in *Recent advances in earthquake geotechnical engineering and microzonation*, pp. 139–197, Springer, 2004.

Prudencio, J., E. Del Pezzo, A. García-Yeguas, and J. M. Ibáñez, Spatial distribution of intrinsic and scattering seismic attenuation in active volcanic islands – I: model and the case of Tenerife Island, *Geophysical Journal International*, *195*(3), 1942–1956, doi:10.1093/gji/ggt361, 2013.

Quintal, B., R. Jänicke, J. G. Rubino, H. Steeb, and K. Holliger, Sensitivity of s-wave attenuation to the connectivity of fractures in fluid-saturated rocks, *Geophysics*, *79*(5), WB15–WB24, 2014.

Rigano, R., F. Cara, G. Lombardo, and A. Rovelli, Evidence for ground motion polarization on fault zones of mount etna volcano, *Journal of Geophysical Research: Solid Earth*, *113*(B10), 2008.

Rovida, A., R. Camassi, P. Gasperini, and M. Stucchi, Catalogo parametrico dei terremoti italiani, versione cpti11, 2011.

Rubin, A. M., D. Gillard, and J.-L. Got, Streaks of microearthquakes along creeping faults, *Nature*, *400*(6745), 635, 1999.

Saito, T., H. Sato, and M. Ohtake, Envelope broadening of spherically outgoing waves in three-dimensional random media having power law spectra, *Journal of Geophysical Research: Solid Earth*, *107*(B5), ESE–3, 2002.

Saito, T., H. Sato, M. Ohtake, and K. Obara, Unified explanation of envelope broadening and maximum-amplitude decay of high-frequency seismograms based on the envelope simulation using the markov approximation: Forearc side of the volcanic front in northeastern honshu, japan, *Journal of Geophysical Research: Solid Earth*, *110*(B1), 2005.

Sato, H., M. C. Fehler, and T. Maeda, *Seismic wave propagation and scattering in the heterogeneous earth*, vol. 496, Springer, 2012.

Scarfi, L., H. Langer, and S. Gresta, High-precision relative locations of two microearthquake clusters in southeastern sicily, italy, *Bulletin of the Seismological Society of America*, *93*(4), 1479–1497, 2003.

Schiattarella, M., Quaternary tectonics of the pollino ridge, calabria-lucania boundary, southern italy, *Geological Society, London, Special Publications*, *135*(1), 341–354, 1998.

Scionti, V., P. Galli, and G. Chiodo, The calabrian seismicity during the viceroyalty of naples: Sources silence or silent sources? the case of the strong 1744 earthquake, *Boll. Geof. Teor. Appl.*, *47*(1/2), 53–72, 2006.

Sgarlato, G., G. Lombardo, and R. Rigano, Evaluation of seismic site response nearby underground cavities using earthquake and ambient noise recordings: A case study in catania area, italy, *Engineering Geology*, *122*(3-4), 281–291, 2011.

Singh, S. K., and M. Ordaz, On the origin of long coda observed in the lake-bed strong-motion records of mexico city, *Bulletin of the Seismological Society of America*, *83*(4), 1298–1306, 1993.

Sketsiou, P., F. Napolitano, A. Zenonos, and L. De Siena, New insights into seismic absorption imaging, *Physics of the Earth and Planetary Interiors*, *298*, 106,337, doi: https://doi.org/10.1016/j.pepi.2019.106337, 2020.

Snoke, J., A program for focal mechanism determination by combined use of polarity and sv-p amplitude ratio data, *Earthquake notes*, *55*, 15, 1984.

Snoke, J., Earthquake mechanisms, encyclopedia of geophysics (de james, ed.), 1989.

Souriau, A., et al., Multimethod characterization of the french-pyrenean valley of bagnères-de-bigorre for seismic-hazard evaluation: observations and models, *Bulletin of the Seismological Society of America*, *101*(4), 1912–1937, 2011.

Steidl, J. H., Variation of site response at the ucsb dense array of portable accelerometers, *Earthquake Spectra*, *9*(2), 289–302, 1993.

Strollo, A., S. Richwalski, S. Parolai, M. Gallipoli, M. Mucciarelli, and R. Caputo, Site effects of the 2002 molise earthquake, italy: analysis of strong motion, ambient noise, and synthetic data from 2d modelling in san giuliano di puglia, *Bulletin of Earthquake Engineering*, *5*(3), 347–362, 2007.

Su, F., J. G. Anderson, J. N. Brune, and Y. Zeng, A comparison of direct s-wave and coda-wave site amplification determined from aftershocks of the little skull mountain earthquake, *Bulletin of the Seismological Society of America*, *86*(4), 1006–1018, 1996.

Takahashi, T., H. Sato, T. Nishimura, and K. Obara, Strong inhomogeneity beneath quaternary volcanoes revealed from the peak delay analysis of s-wave seismograms of microearthquakes in northeastern japan, *Geophysical Journal International*, *168*(1), 90–99, 2007.

Takahashi, T., H. Sato, T. Nishimura, and K. Obara, Tomographic inversion of the peak delay times to reveal random velocity fluctuations in the lithosphere: method and application to northeastern japan, *Geophysical Journal International*, *178*(3), 1437–1455, 2009.

Tertulliani, A., and L. Cucci, New insights on the strongest historical earthquake in the pollino region (southern italy), *Seismological Research Letters*, *85*(3), 743–751, 2014.

Totaro, C., D. Presti, A. Billi, A. Gervasi, B. Orecchio, I. Guerra, and G. Neri, The ongoing seismic sequence at the pollino mountains, italy, *Seismological Research Letters*, *84*(6), 955–962, 2013.

Totaro, C., L. Seeber, F. Waldhauser, M. Steckler, A. Gervasi, I. Guerra, B. Orecchio, and D. Presti, An intense earthquake swarm in the southernmost apennines: Fault architecture from high-resolution hypocenters and focal mechanismsan intense earthquake swarm in the southernmost apennines, *Bulletin of the Seismological Society of America*, *105*(6), 3121–3128, 2015.

Tripathi, J. N., P. Singh, and M. L. Sharma, Attenuation of high-frequency p and s waves in garhwal himalaya, india, *Tectonophysics*, *636*, 216–227, 2014.

Vinci, C., J. Renner, and H. Steeb, On attenuation of seismic waves associated with flow in fractures, *Geophysical Research Letters*, *41*(21), 7515–7523, 2014.

Waldhauser, F., and W. L. Ellsworth, A double-difference earthquake location algorithm: Method and application to the northern hayward fault, california, *Bulletin of the Seismological Society of America*, *90*(6), 1353–1368, 2000.

Waldhauser, F., and D. P. Schaff, Large-scale relocation of two decades of northern california seismicity using cross-correlation and double-difference methods, *Journal of Geophysical Research: Solid Earth*, *113*(B8), 2008.

Wathelet, M., D. Jongmans, and M. Ohrnberger, Surface-wave inversion using a direct search algorithm and its application to ambient vibration measurements, *Near surface geophysics*, *2*(4), 211–221, 2004.

Watts, D. G., and G. Jenkins, Spectral analysis and its applications, *San Francisco*, 1968.

Xue, H., K. Ogawa, and T. Shoji, Effect of welded mechanical heterogeneity on local stress and strain ahead of stationary and growing crack tips, *Nuclear Engineering and Design*, *239*(4), 628–640, 2009.

Yang, Z., Y. Chen, Y. Zheng, and X. Yü, Accurate relocation of earthquakes in central-western china using the double-difference earthquake location algorithm, *Science in China Series D: Earth Sciences*, *46*(2), 181–188, 2003.